Graduate Theses and Dissertations

Iowa State University Capstones, Theses and Dissertations

2019

Analysis of guided and leaky modes of circular waveguides and realization of mechanical tunable metamaterial and devices

Siming Yang
Iowa State University

Follow this and additional works at: https://lib.dr.iastate.edu/etd

Part of the Alternative and Complementary Medicine Commons, and the Electromagnetics and Photonics Commons

Analysis of guided and leaky modes of circular waveguides and realization of mechanical tunable metamaterial and devices

by

Siming Yang

A dissertation submitted to the graduate faculty

in partial fulfillment of the requirements for the degree of

DOCTOR OF PHILOSOPHY

Major: Electrical Engineering

Program of Study Committee:
Jiming Song, Co-major Professor
Liang Dong, Co-major Professor
Nathan Neihart
Mani Mina
John R. Bowler

The student author, whose presentation of the scholarship herein was approved by the program of study committee, is solely responsible for the content of this dissertation. The Graduate College will ensure this dissertation is globally accessible and will not permit alterations after a degree is conferred.

Iowa State University

Ames, Iowa

2019

TABLE OF CONTENTS

iv

LIST OF TABLES

LIST OF FIGURES

ACKNOWLEDGEMENTS

ABSTRACT

The guided and leaky mode characteristics for planar dielectric structures are relatively well known, due to its various kind of applications. However, the investigation to the modes characteristics for a circular rod structure is relatively rare, especially for the leaky modes, despite the rod structure is very simple and useful.

Accordingly, in the first part of the thesis, we analyze the guided and leaky modes for a circular dielectric rod in detail. The analysis is carried out in several steps. First, by considering the field distributions outside the rod, the modes are well defined and classified based on their physical meanings. The relations for the mode solutions using different types of special functions and Riemann sheets are figured out. Further, completed forms of characteristic equations used to solve different modes are presented explicitly. Second, in order to solve this nonlinear characteristic equation efficiently and accurately, we employ iterative methods and spent lots of efforts in deriving the initial guess expression in a simply but efficient form. Through using the asymptotic expansion method and employing the Lambert W function, we derive the initial guesses around the cutoff frequency, low frequency limit and high frequency limit for both TM and TE cases. Finally, the numerical results are presented for the complex transverse propagation constants of proper and two types of improper modes for both cases. Some of the improper modes have not been shown in literatures.

Next, we extend the analysis to the circular rod with negative permittivity and permeability (double negative material (DNG)). Following the same analysis procedure for the conventional dielectric circular rod, first, we derive the characteristic equation for the DNG case and define different types of modes. Second, we expand the characteristic equation asymptotically and then find the initial guess expression for different types of modes

around the cutoff, high frequency limit and low frequency limit. Finally, using these initial guesses we solve the characteristic equation with iterative methods and find the dispersion curves.

The electromagnetic (EM) material property of simultaneous negative permittivity and permeability we use for the DNG rod analysis actually can not be found in nature so far. The method in generating material with DNG property is using metamaterials. In the second part of the thesis we introduce metamaterials, and discuss our work of realizing tunable metamaterials in detail. This type of tunable property allows the metamaterial device to overcome the drawback of fixed and limited bandwidth from the conventional metamaterials.

We start it from presenting a novel tunable and flexible SRR-based meta-atom capable of tuning its EM response characteristics over a broad frequency range by simple mechanical stretching. First, we design and simulate a meta-atom with a liquid metal as the resonator material. The liquid metal is patterned to be a SRR structure and embedded inside a highly stretchable silicone elastomer. Due to its liquid nature, the liquid metal-based SRR could flow in response to an applied strain, and compliant to change from the encasing elastomer as the meta-atom being stretched and twisted. Therefore, through simple mechanical stretching, the shape of the SRR is changed. Correspondingly, the equivalent capacitance and inductance of the SRR are adjusted, thus tuning the resonance frequency of the meta-atom. The shifting trend of the resonance frequency with different stretching orientations is predicted by a simple circuit mode, and verified from the experiment.

Next, we extend the idea of meta-atom to the meta-skin, which is composed of an array of meta-atoms. This meta-skin performed as a tunable selective surface with a wide resonance frequency tuning range when being stretched. Further, due to its flexibility, this meta-skin can function as a flexible "cloaking" surface in suppressing the scattering from the dielectric object. As examples, we demonstrate frequency selective responses of multilayer meta-skins with different stretching ratio in the planar direction. Also, we investigate

scattering suppression effect of the meta-skin coated on a finite-length dielectric rod in free space.

Benefit from the liquid metal and highly stretchable elastomer, we design and realize a directivity reconfigurable two-arm spiral antenna. This new device has the ability to reconfigurate the radiation pattern along the main lobe direction by control the shape of the antenna, as the radiation pattern becomes sharper, directivity is optimized. Finally, the directivity, efficiency, and axial ratio with different dome height, operating frequencies are presented.

CHAPTER 1.   INTRODUCTION

1.1   Reveiw on Electromagnetic Propagation in Circular Rod Structure

Geometrical configurations based on a circular rod are very popular, such as coaxial lines and cavities; these cylindrical structures maintain a uniform cross section along their length. However, due to the conductor loss, the metallic based structures are impractical in the high frequency region. A better option is to use the low loss dielectric waveguide [1]-[3]. One of the well known examples is the optical fiber. In 1966, Kao [4] published a paper on the theory and practice of optical fiber for communication applications, which heralded the beginning of a new era in telecommunications. Investigation related to the guide modes has been well established even earlier than 1966 [5, 6], whereas the leaky modes below the cutoff frequency have been scarcely investigated. Yet, the leaky wave is useful in the many antenna applications [7]-[10]. Until 1969, Arnbak [11] found the complex propagation constant below the cutoff frequency by solving the asymptotic forms of the characteristic equation, thus, proving the existence of leaky modes in the circular dielectric waveguide. Later on, Sammut [12] presented the characteristic of the leaky modes graphically for both lossless and lossy cases. However, these results were obtained based on approximation method, which led to the results not accurate enough for further applications.

Several decades later, Kim studied the guided and leaky modes supported by the dielectric circular rod [13, 14], and demonstrated several lower order modes by using the Davidenko's complex root finding algorithm. In addition, Kim also defined and explained the regimes of these modes based on their physical meanings [15]-[18]. To solve the eigenvalue problems more efficiently, the asymptotic formulas have been derived before using the numerical solvers for planar and circular multilayered structures [19]-[23]. The waveguides open to air or closed with perfect matching layer (PML) were considered, and Lambert

W function [24, 25] has been leveraged frequently to simplify the asymptotic expressions. Solutions to dispersion equations with a complex dielectric permittivity are considered [26] for microwave transfer in tubular sliding-mode plasma waveguides.

However, through investigating these articles and relevant textbooks [27, 28], we found that there are still many ambiguous parts left unsolved. First of all, different special functions involved characteristic equations have been employed in different articles [11, 13] or textbooks [27, 28] to solve these modes. A same solution is achieved using different special functions for proper (guided) modes. Nevertheless, due to the multiple value issue in the special functions, confusion and difficulty emerge for improper (leaky) modes. Secondly, it is also found that types of improper modes have not been demonstrated completely for both TM and TE cases in the previous works. The ways of obtaining and indexing these modes are unclear as well [13, 14].

Based on these considerations, in the first part of the thesis we will start the analysis of proper and improper modes from the perspective of special functions to find the solutions supported by the circular dielectric waveguide. Accordingly, three kinds of special functions: Hankel function of the first kind ($H_m^{(1)}(\cdot)$), Hankel function of the second kind ($H_m^{(2)}(\cdot)$), and modified Bessel function ($K_m(\cdot)$) are analyzed in detail to find the relationship of the solutions when a designated special function is involved. Then, a set of completed form of characteristic equations for different cases are explicitly exhibited.

The nonlinear characteristic equation we are interesting with has no closd form solution, thus we will employ Newton-Raphson method to solve it iteratively. As we know the initial guess is important for the iterative method, which affects both efficiency of the solving process and accuracy. In order to derive a simple and accurate initial guess expression, we employed the asymptotic expansion method [29] to find the initial guess expressions for proper and improper modes based on the characteristic equations of TM and TE cases. The initial guess derivation for the hybrid (EH or HE) modes will not be discussed in this thesis. It is believed that the idea of deriving the initial guesses for both TM and TE cases

can be further extended to derive the initial guess for the hybrid modes. In this process, analysis for the modes in dielectric slab [30]-[34] has been referred.

For completeness, initial guess expressions are derived from high and low frequency limits, and around cutoff frequency respectively. In this process, we leveraged Lambert W function in some expressions. These complete initial guess expressions provide simple and efficient way of indexing these modes. Finally, Newton method is employed to determine the complex propagation constant of both proper and improper modes for TM and TE case. The numerical results are verified by comparing with Kim's results [13].

The analysis procedures we mentioned above are not only limited to circular rod made of double positive (DPS) material, which has simultaneous positive permittivity and permeability, but also applicable to double negative (DNG) material, which has simultaneous negative permittivity and permeability. Following the analysis procedures for the conventional rod, we defined different types of modes for the DNG rod. Then we derived the completed initial guess expressions of different type modes for the DNG case. These expressions are not exactly the same as the expression for the DPS case, especially the index for numbering different order of modes in the initial guess expressions. Finally, the dispersion curves for DNG case will be presented, and the difference between DPS and DNG cases will be discussed in detail.

1.2   Review on Tunable Metamaterials

Flexible electronics have gained considerable attentions because of their potential applications in artificial skins, flexible displays, wearable sensors, sustainable energy, etc. Many flexible electronic devices have recently been developed, such as stretchable integrated circuits [35]-[39], microfluidic antennas [40]-[42], three-dimensional energy devices [43], printed thin film transistors [44]-[47], and biometric pressure sensors [48]. On the other hand, EM metamaterials have been intensively studied because they possess intriguing properties unattainable with naturally existing materials, such as negative permittivity

and permeability [49]-[61]. Split ring resonator (SRR) is a popular building block of many metamaterial-based resonant devices in the microwave regime [62]-[65]. But, these resonant devices often have a limited bandwidth. If the metamaterial's response characteristics can be dynamically tuned, then the usefulness of these resonant devices will be significantly extended. To this end, a number of tunable metamaterial technologies have been demonstrated, based on changing unit cell's effective circuit parameters [66]-[70], constituent material properties [71]-[76], or geometries [77]-[82]. Specifically, the circuit tuning method uses variable capacitors and switches to change individual impedances of unit cells [66]-[70]. Tuning of the constituent materials relies on using phase change materials or liquid crystal to change properties of materials that make up unit cells [66]-[70].

The micro-electro-mechanical systems and microfluidics based approaches change structures and locations of unit cells relative to a fixed part of metamaterials [77]-[82]. While the aforementioned tunable metamaterial technologies have led to significant improvement toward broadening dynamic tuning ranges of the EM properties of the microwave metamaterials, there is still much room to improve. One possible direction is to simplify the frequency tuning mechanism, while further extending the frequency tuning range of metamaterials. The other direction is to increase the structural flexibility to make metamaterials not only tunable but also compliant to any arbitrary surface of the interaction object. Recently, a switchable metamaterial has been developed, capable of tuning its resonance frequency by pumping mercury into and out of SRR-shaped microchannels [75]. But, this approach required a relatively complex microfluidic control system to modify the gap capacitance of the SRR. We also noted that a tunable liquid metal-based antenna has been formed, by injecting a liquid metal alloy into a microchannel made of a stretchable elastomer [40]. This device could be stretched to more than double of its original length, thus obtaining a wide frequency tuning range.

In this part of the thesis we presented a novel tunable and flexible SRR-based meta-atom capable of tuning its EM response characteristics over a broad frequency range by simple

mechanical stretching. The presented meta-atom used a liquid metal as the resonator material. The liquid metal was patterned to be a SRR structure and embedded inside a highly stretchable silicone elastomer. Due to its liquid nature, the liquid metal-based SRR could flow in response to an applied strain, and thus, was not prone to fatigue or cracking. When the encasing elastomer was stretched and twisted, the SRR was shown sufficiently compliant to yield the necessary deformation. Therefore, by changing the shape of the SRR via simple mechanical stretching, the gap distance and thus the gap capacitance of the SRR could be adjusted, thus tuning the resonance response of the meta-atom.

Further, we designed and fabricated meta-skin composed of meta-atoms array by using the same fabrication technology. Compared with the single meta-atom, the meta-skin can perform as a tunable selective surface with a wide frequency tuning range when being stretched. Also, the meta-skin can be wrapped around a curved dielectric material, due to its flexibility, and function as "cloaking" surface. The experimental result for frequency selective surface and "cloaking" effect are demonstrated in Chapter 5.

1.3   Review on Directivity Reconfigurable Antennas

Electronics have been extensively studied because they provide a simple mean of integrating electronic devices on curved surfaces for various applications, such as wearable devices, artificial skins, flexible displays, and flexible solar energy harvesters [35, 36, 83, 84, 85, 86].

Among these devices, reconfigurable antennas [87]-[89] have attracted increasing attentions due to the explosive growth of wireless communications, satellite communications, wireless power transfer, radar, etc, where the radiation pattern reconfigurability of antennas is highly demanded. Several liquid metal based tunable antennas have been reported based on different tuning mechanisms and designs, including a stretchable dipole antenna or unbalanced loop antenna [90], an electrically small antenna [91], and an electrochemical controlled capillary actuated monopole antenna [89]. All of these reconfigurable antennas

are mainly focused on frequency tuning and exhibit their radiation patterns with relatively low directivity. It should be noted that directional antennas are challenging to develop and widely demanded for applications such as wireless communication, remote sensing, and targeted power transfer. Therefore, antennas capable of reconfiguring directivity are highly desired to optimize their transmission or receiving power in a specific direction of interest.

Benefit from the fabrication technology, which has been introduced in Chapters 4 and 5, of embedding liquid metal into a flexible elastomer. In Chapter 6, we report the development of a directivity reconfigurable two-arm spiral antenna made of all flexible materials. The original planar antenna can be inflated to form a dome-like shape by blowing high-pressure air into an air cavity below the antenna with the help of commercial micro-electromechanical systems (MEMS) based microblowers. The ability to change the shape of the antenna allows reconfiguring the radiation pattern of the antenna along the main lobe direction or the inflation direction. Due to the formation of the dome-shaped structure, the radiation pattern of the antenna becomes sharper, thus optimizing its directivity, while its passing band still remains in a wide frequency range.

For the metamaterial and devices presented in Chapters 4, 5, and 6, Dr. Peng Liu and I designed the structures, I performed the EM modeling and simulations, Dr. Peng Liu did the mechanical simulations and fabrication work, and we did the measurement together.

CHAPTER 2.   ANALYSIS OF GUIDED AND LEAKY MODES IN CIRCULAR DIELECTRIC WAVEGUIDE

2.1   Formulations

The analysis of the guided and leaky modes in the circular dielectric waveguide is actually to find the propagation constant in the rod structure. In this section we will in detail analyze the steps to set up the characteristic equation and solve the equations in different situations. To begin with, we will first have the the structure setup.

2.1.1   Structure Setup

A uniform circular dielectric waveguide is embedded in an infinite homogeneous medium. This circular waveguide is infinity long in the z direction with radius a. The structure is illustrated in Figure 2.1. ϵ_{ri} and μ_{ri} are the relative permeability and permittivity respectively. The second subscript $i = 1$ represents the region within the rod, and $i = 2$ represents the region outside the rod. The purpose is to find all the possible modes can be supported by this structure. To solve this problem, we can start from expressing the axial field distribution of structure [27].

$$E_{zi} = A_i \mathscr{C}_m(k_{\rho i}\rho) \left\{ \begin{array}{c} \sin(m\varphi) \\ \cos(m\varphi) \end{array} \right\} e^{-jk_z z} \tag{2.1a}$$

$$H_{zi} = B_i \mathscr{C}_m(k_{\rho i}\rho) \left\{ \begin{array}{c} \cos(m\varphi) \\ \sin(m\varphi) \end{array} \right\} e^{-jk_z z} \tag{2.1b}$$

where A_i and B_i are the coefficient to be determined. $\mathscr{C}_m(k_{\rho 1}\rho)$ denotes $J_m(k_{\rho 1}\rho)$ for $i = 1$ and $\mathscr{C}_m(k_{\rho 2}\rho)$ denotes $H_m^{(2)}(k_{\rho 2}\rho)$ for $i = 2$, where $J_m(\cdot)$ is the m-th order Bessel
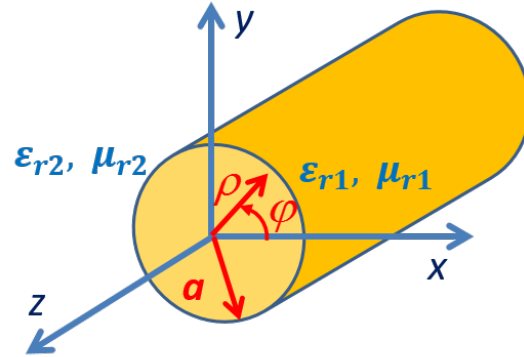
Figure 2.1   Circular dielectric rod with radius a

function of the first kind, $H_m^{(2)}(\cdot)$ is Hankel function of the second kind, m and k_z are the azimuthal wave number and axial propagation constant, $k_{\rho i}$ denotes the transverse complex propagation constant. It is defined as

$$k_{\rho i} = \sqrt{k_0^2 \mu_{ri} \epsilon_{ri} - k_z^2} \tag{2.2}$$

where $i = 1, 2$ and k_0 is the wave number in free space. Other field components related to H_z are expressed as [27]

$$E_\rho = -\frac{j\omega\mu}{k_\rho^2} \frac{1}{\rho} \frac{\partial H_z}{\partial \varphi} \qquad\qquad H_\rho = -\frac{jk_z^2}{k_\rho^2} \frac{\partial H_z}{\partial \rho} \tag{2.3a}$$

$$E_\varphi = \frac{j\omega\mu}{k_\rho^2} \frac{\partial H_z}{\partial \rho} \qquad\qquad H_\varphi = -\frac{jk_z}{k_\rho^2} \frac{1}{\rho} \frac{\partial H_z}{\partial \varphi} \tag{2.3b}$$

Similarly, field components in other directions related to E_z are expressed as:

$$E_\rho = -\frac{jk_z}{k_\rho^2} \frac{\partial E_z}{\partial \rho} \qquad\qquad H_\rho = \frac{j\omega\epsilon}{k_\rho^2} \frac{1}{\rho} \frac{\partial E_z}{\partial \varphi} \tag{2.4a}$$

$$E_\varphi = -\frac{jk_z}{k_\rho^2} \frac{1}{\rho} \frac{\partial E_z}{\partial \varphi} \qquad\qquad H_\varphi = -\frac{j\omega\epsilon}{k_\rho^2} \frac{\partial E_z}{\partial \rho} \tag{2.4b}$$

By substituting Equation (2.1) into Equations (2.3) and (2.4), the field components in ρ and φ directions are expressed as

$$E_{\rho i} = -\frac{j}{k_{\rho i}^2}\left[A_i k_z k_{\rho i}\mathscr{C}'_m(k_{\rho i}\rho) \mp B_i\frac{m\omega\mu_i}{\rho}\mathscr{C}_m(k_{\rho i}\rho)\right]\left\{\begin{array}{c} \sin(m\varphi) \\ \cos(m\varphi) \end{array}\right\}e^{-jk_z z} \qquad (2.5a)$$

$$E_{\varphi i} = -\frac{j}{k_{\rho i}^2}\left[\pm A_i\frac{k_z m}{\rho}\mathscr{C}_m(k_{\rho i}\rho) - B_i\omega\mu_i\mathscr{C}'_m(k_{\rho i}\rho)\right]\left\{\begin{array}{c} \cos(m\varphi) \\ \sin(m\varphi) \end{array}\right\}e^{-jk_z z} \qquad (2.5b)$$

$$H_{\rho i} = -\frac{j}{k_{\rho i}^2}\left[\mp A_i\frac{\omega m\epsilon_i}{\rho}\mathscr{C}_m(k_{\rho i}\rho) + B_i k_z k_{\rho i}\mathscr{C}'_m(k_{\rho i}\rho)\right]\left\{\begin{array}{c} \cos(m\varphi) \\ \sin(m\varphi) \end{array}\right\}e^{-jk_z z} \qquad (2.5c)$$

$$H_{\varphi i} = -\frac{j}{k_{\rho i}^2}\left[A_i\omega\epsilon_i k_{\rho i}\mathscr{C}'_m(k_{\rho i}\rho) \mp B_i\frac{mk_z}{\rho}\mathscr{C}_m(k_{\rho i}\rho)\right]\left\{\begin{array}{c} \sin(m\varphi) \\ \cos(m\varphi) \end{array}\right\}e^{-jk_z z} \qquad (2.5d)$$

In Equation (2.5) $i = 1, 2$. The $\prime$ stands for the derivative to the special function. After getting the expressions for all of the field components, we can apply the following boundary condition for the rod.

$$E_{z1}|_{\rho=a} = E_{z2}|_{\rho=a}, \qquad\qquad H_{z1}|_{\rho=a} = H_{z2}|_{\rho=a} \qquad (2.6a)$$

$$E_{\varphi 1}|_{\rho=a} = E_{\varphi 2}|_{\rho=a}, \qquad\qquad H_{\varphi 1}|_{\rho=a} = H_{\varphi 2}|_{\rho=a} \qquad (2.6b)$$

By substituting the fields expression into Equation (2.6a) and (2.6b), we will have

$$A_1\frac{mk_z}{k_0 a}\left(\frac{1}{k_{\rho 1}^2} - \frac{1}{k_{\rho 2}^2}\right) \mp B_1\left[\frac{\mu_{r1}J'_m(k_{\rho 1}a)}{k_{\rho 1}J_m(k_{\rho 1}a)} - \frac{\mu_{r2}H_m^{(2)\prime}(k_{\rho 2}a)}{k_{\rho 2}H_m^{(2)}(k_{\rho 2}a)}\right] = 0 \qquad (2.7a)$$

$$\mp B_1\frac{mk_z}{k_0 a}\left(\frac{1}{k_{\rho 1}^2} - \frac{1}{k_{\rho 2}^2}\right) + A_1\left[\frac{\epsilon_{r1}J'_m(k_{\rho 1}a)}{k_{\rho 1}J_m(k_{\rho 1}a)} - \frac{\epsilon_{r2}H_m^{(2)\prime}(k_{\rho 2}a)}{k_{\rho 2}H_m^{(2)}(k_{\rho 2}a)}\right] = 0 \qquad (2.7b)$$

To have non-trivial solution for A_1 and B_1, the determinant of the coefficient matrix must vanish. After simplification and arrangement, the characteristic equation is derived as follow

$$\left[\frac{\mu_{r1}J'_m(k_{\rho 1}a)}{k_{\rho 1}J_m(k_{\rho 1}a)} - \frac{\mu_{r2}H_m^{(2)\prime}(k_{\rho 2}a)}{k_{\rho 2}H_m^{(2)}(k_{\rho 2}a)}\right]\left[\frac{\epsilon_{r1}J'_m(k_{\rho 1}a)}{k_{\rho 1}J_m(k_{\rho 1}a)} - \frac{\epsilon_{r2}H_m^{(2)\prime}(k_{\rho 2}a)}{k_{\rho 2}H_m^{(2)}(k_{\rho 2}a)}\right] = \left(\frac{mk_z}{k_0 a}\right)^2\left(\frac{1}{k_{\rho 1}^2} - \frac{1}{k_{\rho 2}^2}\right)^2$$
$$(2.8)$$

By solving Equation (2.8), we can obtain all the modes supported by the rod. However, it is complicated to solve this equation directly. In order to make our discussion more efficiently, we will not discuss the hybrid modes (HE or EH) here, which is $m \neq 0$. In stead, we will focus on TE and TM cases, where $m = 0$ in Equation (2.8).

2.1.2 Characteristic Equation and Modes Definition

A specific case is considered here by imposing $m = 0$, which means modes are without variations along the circular angles. Under this circumstance, Equation (2.8) is split into two characteristic equations. The one without H_z component represents the TM_{0n} modes, and the one without E_z component represents TE_{0n} modes, where the first subscript comes from $m = 0$, and the second subscript denotes the order of the modes. Mathematically, the characteristic equations for TE and TM cases are identical by simply reciprocating material parameters, thus both cases are discussed in this report based on the same form of characteristic equation. Before further discussion, new variables u and v are introduced to simplify notation, which are expressed as

$$u \triangleq k_{\rho 1} a = k_0 a \sqrt{\mu_{r1} \epsilon_{r1} - \delta^2} \tag{2.9a}$$

$$v \triangleq j k_{\rho 2} a = k_0 a \sqrt{\delta^2 - \mu_{r2} \epsilon_{r2}} \tag{2.9b}$$

where $\delta = k_z / k_0$, and r is given by

$$r = \sqrt{u^2 + v^2} = k_0 a \sqrt{\mu_{r1} \epsilon_{r1} - \mu_{r2} \epsilon_{r2}} \tag{2.10}$$

Further, by introducing the relationship of $H_0^{(2)\prime}(z) = -H_1^{(2)}(z)$ and $J_0'(z) = -J_1(z)$, the characteristic equation is rewritten as

$$\frac{\kappa}{u} \frac{J_1(u)}{J_0(u)} + \frac{1}{jv} \frac{H_1^{(2)}(-jv)}{H_0^{(2)}(-jv)} = 0 \tag{2.11}$$

where $\kappa = \epsilon_{r1} / \epsilon_{r2}$ for TM case and $\kappa = \mu_{r1} / \mu_{r2}$ for TE case. For non-magnetic dielectric rod $\mu_{r1} = \mu_{r2} = 1$, thus $\kappa = 1$. For Equation (2.11), either u, v, or δ can be treated as

an unknown. It is well known that Hankel function of the second kind has multiple value property in complex plane, and it is found that Equation (2.11) is an even function of u and δ. These properties of Equation (2.11) make v as a variable directly a better choice. In this situation, the square root issue introduced by solving δ or u is directly avoided. Once v is solved, u and δ are expressed in terms of v explicitly. Equation (2.9b) indicates that v describes the wave behavior along the radial direction outside the circular dielectric rod. By substituting v into the leading transverse wave form of the Hankel function, we have $e^{v\rho/a} = e^{-\mathrm{Re}(v)\rho/a}e^{-j\mathrm{Im}(v)\rho/a}$. It is clear that v is normalized complex transverse attenuation constant with the imaginary part for propagation constant. Accordingly, Table 2.1 presents the classification of different types of modes based on v, and these definitions will be used in the following discussion.

Table 2.1   Classification of different kinds of modes

	Proper Modes	Improper Modes	
		Outging	Incoming
$\mathrm{sign}(\mathrm{Re}(v))$	$(+)$	$(-)$	
$\mathrm{sign}(\mathrm{Im}(v))$	$(+,-)$	$(+)$	$(-)$

2.1.3   Relationship between Special Functions and Propagation Constants

Besides expressing Equation (2.11) in terms of $H_m^{(2)}(\cdot)$, the characteristic equation can be also expressed in terms of $K_m(\cdot)$, and $H_m^{(1)}(\cdot)$ with different arguments

$$\frac{\kappa}{u}\frac{J_1(u)}{J_0(u)} + \frac{1}{v}\frac{K_1(v)}{K_0(v)} = 0 \tag{2.12}$$

$$\frac{\kappa}{u}\frac{J_1(u)}{J_0(u)} - \frac{1}{jv}\frac{H_1^{(1)}(jv)}{H_0^{(1)}(jv)} = 0 \tag{2.13}$$

For the proper modes, solutions corresponding to different special functions involved equations are distributed in the same Riemann sheet. Thus, the characteristic Equations (2.11), (2.12) and (2.13) give same solutions. However, the improper cases are more complicated due to the multiple value issue involved. Starting from the relationship between $K_m(\cdot)$,

$H_m^{(1)}(\cdot)$ and $H_m^{(2)}(\cdot)$, we have the following relationship by considering $K_m(\cdot)$ and $H_m^{(1)}(\cdot)$ in different quadrants.

$$K_m(z) = j(\pi/2)e^{jm\pi/2}H_m^{(1)}(\tilde{z}_1)$$

$$-\pi < \arg(z) \le \pi/2$$

(2.14)

$$K_m(z) = -j(\pi/2)e^{-jm\pi/2}H_m^{(2)}(\tilde{z}_2)$$

$$-\pi/2 < \arg(z) \le \pi$$

(2.15)

(a)   (b)
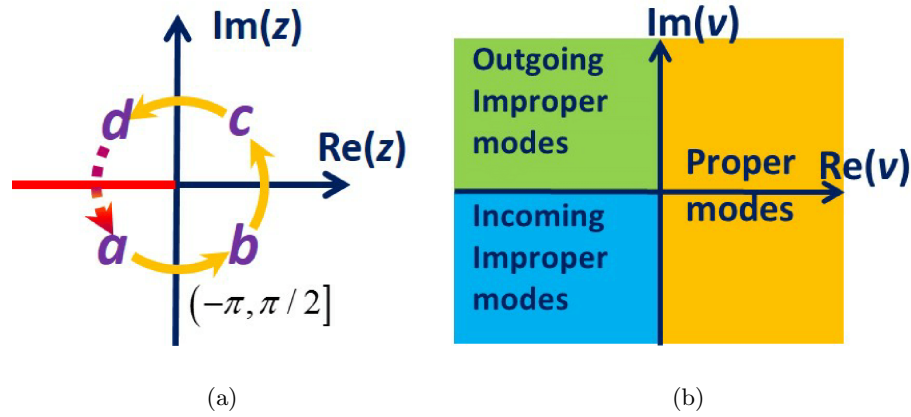
Figure 2.2   (a) Relationship between $K_m(\cdot)$ and $H_m^{(1)}(\cdot)$ in different quadrants. Negative real axis is defined as the branch cut for $\log(z)$, and $\arg(z) : (-\pi, \pi/2]$. (b) Different types of modes.

where $\tilde{z}_1 = ze^{j\pi/2}$, and $\tilde{z}_2 = ze^{-j\pi/2}$. In Figure 2.2(a), a, b, c, and d represent third, fourth, first, and second quadrants respectively. In Figure 2.2(a), when the argument of $K_m(z)$ is defined in location a, b or c, the argument of $H_m^{(1)}(z)$ will move to location b, c and d respectively. When the argument of $K_m(z)$ is in location d, the argument of $H_m^{(1)}(z)$ will across the branch cut and move to the next Riemann sheet. Consequently, $K_m(\cdot)$ and $H_m^{(1)}(\cdot)$ in different Riemann sheets related as

$$K_{m,p-1}(z) = j(\pi/2)e^{jm\pi/2}H_{m,p}^{(1)}(\tilde{z}_1)$$

$$\pi/2 < \arg(z) < \pi$$

(2.16)

where the second subscript p indicates the p-th Riemann sheet. Similarly for Equation (2.15), when z is in the third quadrant, due to the $e^{-j\pi/2}$ factor, the argument of $H_m^{(2)}(\tilde{z}_2)$ rotates clockwise and then crosses the branch cut, finally reaches the other Riemann sheet. Then, we have

$$K_{m,p+1}(z) = -j(\pi/2)e^{-jm\pi/2}H_{m,p}^{(2)}(\tilde{z}_2)$$

$$-\pi < \arg(z) < -\pi/2 \tag{2.17}$$

With these relationships between different special functions, we can qualitatively conclude the relationship between the solutions of Equations (2.12), (2.13), and (2.14): for the proper modes, v is in the first and fourth quadrants. Consequently, all three equations with different special functions give same solutions

$$v_{np}^K = v_{np}^{H_1} = v_{np}^{H_2} \tag{2.18}$$

The superscripts H_2, K, and H_1 mean the solution from Equations (2.11)-(2.13) respectively. The subscript stands for the n-th modes in p-th Riemann sheet. For the outgoing improper mode, as shown in Figure 2.2(b), v is in the second quadrant.

$$v_{np}^K = v_{n(p+1)}^{H_1} = v_{np}^{H_2} \tag{2.19}$$

Similarly, for the incoming improper mode, we have

$$v_{n(p+1)}^K = v_{n(p+1)}^{H_1} = v_{np}^{H_2} \tag{2.20}$$

Equation (2.18) shows that all the proper modes are the same for a given Riemann sheet. Thus, they can be easily solved by using principal form from Equations (2.11), (2.12), and (2.13). However, for the improper mode, when $H_m^{(1)}(\cdot)$ and $K_m(\cdot)$ are selected, corresponding solution distributed in the second or third quadrant will move to the next Riemann sheet. This requires us to convert the formation of the special function according to the different Riemann sheets it finally reaches. For Equation (2.19), the relationship between $H_m^{(1)}(\cdot)$ in its principal value and its p-th Riemann sheet is expressed as [24]:

$$H_{m,p}^{(1)}(z) = (1-2p)H_m^{(1)p.v.}(z) - 2pH_m^{(2)p.v.}(z) \tag{2.21}$$

where the $p.v.$ in the superscript represents the special function is evaluated in the principal value, and in this case $p = 0$. The characteristic equation for improper modes in the second quadrant can be rewritten as

$$\frac{\kappa}{u}\frac{J_1(u)}{J_0(u)} + \frac{1}{jv}\frac{H_1^{(1)}(-jv) + 2H_1^{(2)}(-jv)}{H_0^{(1)}(-jv) + 2H_0^{(2)}(-jv)} = 0 \tag{2.22}$$

Following the same steps, the relationship between $K_m(\cdot)$ in its p-th Riemann sheet and its principal formation is given as [24]:

$$K_{m,p}(z) = K_m^{p.v.}(z) + j2\pi(-1)^{m+1}I_m(z) \tag{2.23}$$

where $I_m(\cdot)$ is m-th order modified Bessel function of the first kind. By employing Equation (2.23), the characteristic equation for the improper modes in the third quadrant with $K_m(\cdot)$ involved is rewritten as

$$\frac{\kappa}{u}\frac{J_1(u)}{J_0(u)} + \frac{1}{v}\frac{K_1(v) + j2\pi I_1(v)}{K_0(v) - j2\pi I_0(v)} = 0 \tag{2.24}$$

Finally, we can conclude that Equations (2.11), (2.12), and (2.22) can be used to solve the improper modes in the second quadrant. Equations (2.11), (2.22), and (2.24) can be used to solve the improper modes in the third quadrant [92].

2.1.4 Complex Conjugate Properties for Lossless Rod

To make this study more complete, the properties related to the relationship of solution and their corresponding complex conjugate are presented. These conclusions, on one hand, give a better understanding of this work; on the other hand, it helps us avoid some unnecessary trouble through the numerical implementation. From the complex conjugate relationship of special functions in their principal values, we have the general complex conjugate relationships for special functions in different Riemann sheets as

$$K_{mp}(z^*) = K_{m(-p)}^*(z) \tag{2.25}$$

$$H_{mp}^{(1)}(z^*) = H_{m(-p)}^{(2)*}(z) \tag{2.26}$$

$$H_{mp}^{(2)}(z^*) = H_{m(-p)}^{(1)*}(z) \tag{2.27}$$

Equations (2.25)-(2.27) indicate that, for the principal value, namely $p = 0$, $[v_n^K]^*$, $[v_n^{H_1}]^*$, and $[v_n^{H_2}]^*$ are the solutions as well for the lossless dielectric rod. For the p-th Riemann sheet, we have $[v_{np}^K]^* = v_{n(-p)}^K$, $[v_{np}^{H_1}]^* = v_{n(-p)}^{H_2}$, and $[v_{np}^{H_2}]^* = v_{n(-p)}^{H_1}$ correspondingly. From the above analysis, the relationship of the complex conjugate solutions corresponding to different types of modes can be concluded as

$$[v_{np}^K]^* = [v_{np}^{H_1}]^* = [v_{np}^{H_2}]^* = v_{n(-p)}^K = v_{n(-p)}^{H_2} = v_{n(-p)}^{H_1} \tag{2.28}$$

for the proper modes in the first and fourth quadrants, and

$$[v_{np}^K]^* = [v_{n(p+1)}^{H_1}]^* = [v_{np}^{H_2}]^* = v_{n(-p)}^K = v_{n(-p-1)}^{H_2} = v_{n(-p)}^{H_1} \tag{2.29}$$

for the improper modes in the second quadrant, and

$$[v_{n(p+1)}^K]^* = [v_{n(p+1)}^{H_1}]^* = [v_{np}^{H_2}]^* = v_{n(-p-1)}^K = v_{n(-p-1)}^{H_2} = v_{n(-p)}^{H_1} \tag{2.30}$$

for the improper modes in the second quadrant. Due to the relationship in the modes solved using different special functions, the following sections will focus on the results solved based on $H_m^{(2)}(\cdot)$ as shown in Equation (2.11).

2.2 Initial Guesses

Among several iterative methods, due to the advantages of easy implementation, converging fast, and requiring only one initial guess, Newton-Raphson method [95] is employed to solve Equation (2.11) numerically. Appropriate initial guess is crucial in finding right solutions with less number of iterations. In this section the initial guesses are derived using the asymptotic form on the $p = 0$ Riemann sheet. By considering the behavior of u and v in different regions, Equation (2.11) is expanded around cutoff frequency, high frequency limit as well as the low frequency limit. From numerical solutions, it is found that from neither of the perspectives mentioned above we can solve three types of modes completely, due to the different types of modes distribute in different regions. Especially for the incoming improper modes, which is further categorized as incoming improper modes stop at cutoff

frequency and the ones stop at DC. In this asymptotic expansion process, we will introduce the Lambert W function [24, 25] with different branches to find accurate and simple forms of initial guesses for both TM and TE cases.

2.2.1 Around the Cutoff Frequency

In the circular dielectric rod, TM_{0n} and TE_{0n} modes share the same cut-off frequency. This can be derived by imposing $v = 0$, which leads to $J_0(u = \chi_{0n}) = 0$, where χ_{0n} denotes the n-th root of zero order Bessel function of the first kind. Consequently, we have $r \approx \chi_{0n}$, $0 \approx v \ll r$, and $u \approx r - v^2/(2r)$ around the cut-off frequency, with small argument expansion, the inverse of the Hankel function term in Equation (2.11) is approximated as

$$- jv \frac{H_0^{(2)}(-jv)}{H_1^{(2)}(-jv)} \approx v^2 \ln(ve^\gamma/2) \tag{2.31}$$

where $\gamma \approx 0.577215664$ is the Euler constant. Similarly, the inverse of Bessel function term in Equation (2.11) is expanded around r as

$$\frac{u}{\kappa} \frac{J_0(u)}{J_1(u)} = c(r) + v^2 b(r)/2 \tag{2.32}$$

where

$$c(r) = \frac{r}{\kappa} \frac{J_0(r)}{J_1(r)} \tag{2.33}$$

$$b(r) = \frac{1}{2\kappa} \left[1 - \frac{J_0(r)}{J_1(r)} \left(\frac{1}{r} - \frac{J_1'(r)}{J_1(r)} \right) \right] \tag{2.34}$$

By combining Equations (2.31)-(2.32) together, and only keeping the leading term of $c(r)$ and $b(r)$, which are defined as

$$b_1 = \frac{1}{2\kappa} \tag{2.35}$$

$$c_1(r) = -\frac{\chi_{0n}(r - \chi_{0n})}{\kappa} \tag{2.36}$$

Equation (2.11) is simplified as

$$v^2 \ln(v^2 a_1^2/4) = 2c_1(r) \tag{2.37}$$

with $a_1 = e^{\gamma - 1/2\kappa}$. The solution corresponding to Equation (2.37) is represented by Lambert W function [24, 25] as

$$v = 2a_1^{-1} e^{\frac{1}{2} W_p(z(r))} \tag{2.38}$$

where the subscript p represents different branches of $W(z)$ and $z(r) = a_1^2 c_1/2$. The principal, -1 and +1 branches of Lambert W function with complex input are demonstrated in Figures 2.3, 2.4 and 2.5 respectively. Sommerfeld derived a form similar to Equation (2.37) for waves over lossy wires [93] (p.183) using asymptotic representation of Bessel functions, but (2.37) keeps more terms as shown in Equation (2.32) by expanding the Bessel functions around the cut-off. Sommefelds solution is in a form corrected step by step in the subsequent approximations [93] (p.183), not the closed form solutions as shown in (2.38) using Lambert W functions. The initial guess expression in Equation (2.38) can predict different type of modes with appropriate branches of Lambert W function, which are summarized as

(a)   (b)
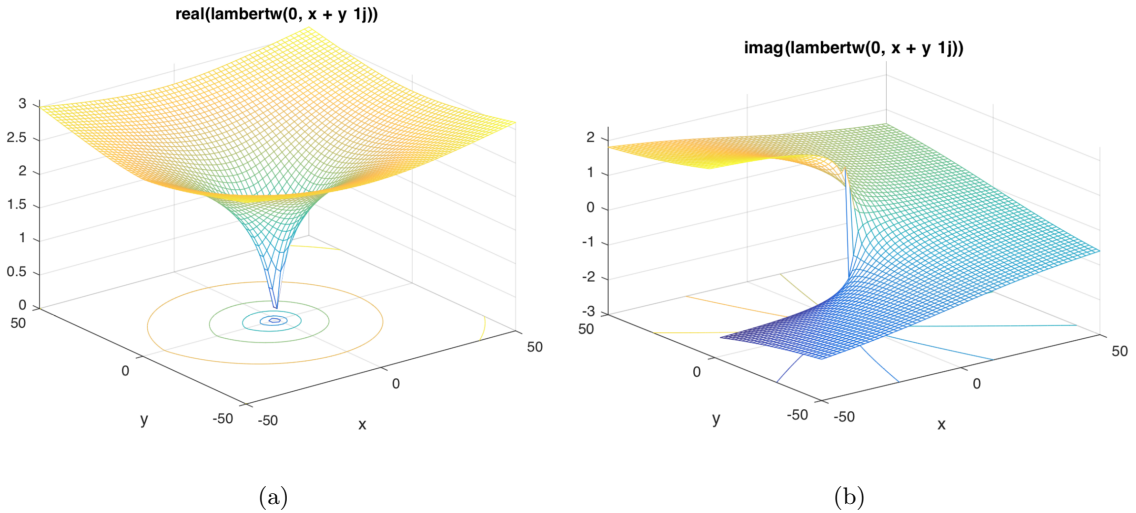
Figure 2.3   Lambert W function for principal branch $p = 0$. (a) Real part. (b) Imaginary part.
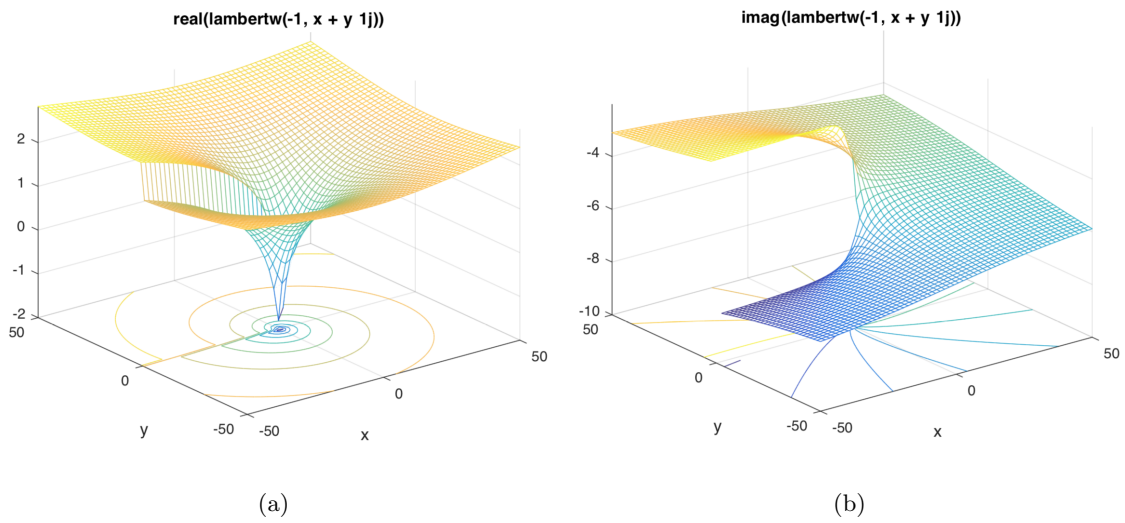
Figure 2.4   Lambert W funciton for branch $p = -1$. (a) Real part. (b) Imaginary part.
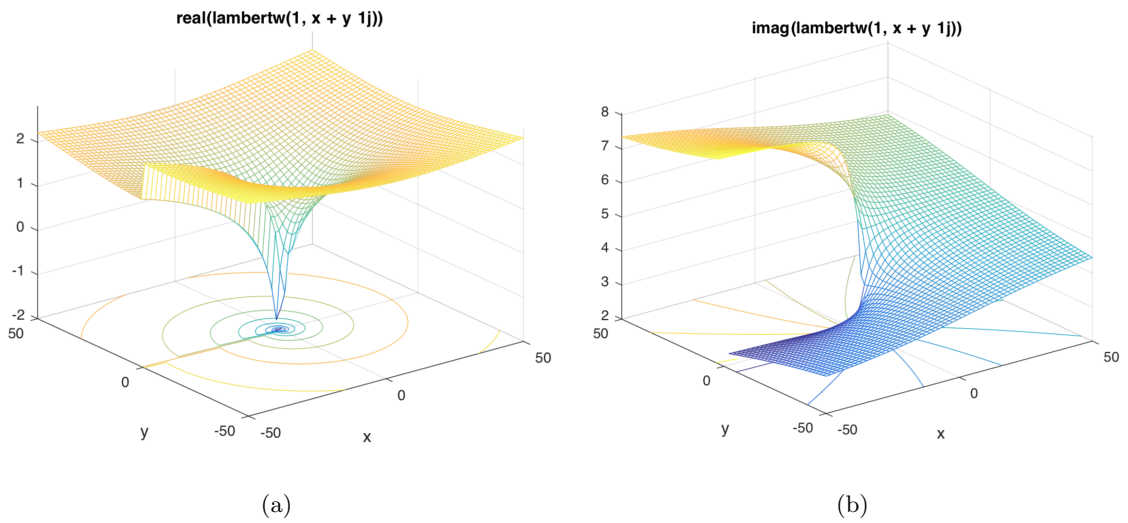
Figure 2.5   Lambert W funciton for branch $p = +1$. (a) Real part. (b) Imaginary part.

The initial guesses in Equation (2.38) are asymptotically expanded in different orders to approximate the true solutions for the proper and improper modes, which are solved numerically using the initial guesses in Equation (2.38). These approximate initial guesses are close to the true solution, as shown in Figure 2.6. However, the difference between initial guesses and true solution is relative large, if all the terms are kept in Equations (2.33) and

Table 2.2   Corresponding branches to derive different types of modes

	Proper Modes	Improper Modes	
		Outgoing	Incoming
p value	-1	1	
$\text{sign}(r - \chi_{0n})$	$(+)$	$(-)$	$(+)$
$\text{sign}(z)$	$(-)$	$(+)$	$(-)$

(2.34), refer to most terms in Figure 2.6. In this situation, Equations (2.31) and (2.32) can be un-symmetric through the expansion. Similarly, if we neglect the v^2 term in Equation (2.32), the initial guesses still have a relative large difference with the true solutions, refer to the least terms in Figure 2.6. From the numerical results, we found that the best way to derive the initial guess around cutoff frequency region is keeping the leading terms in Equation (2.33) and (2.34), referring to the best terms in Figure 2.6. In this manner, the initial guesses are accurate, and the efficiency in deriving these initial guesses is improved [94].

(a)   (b)
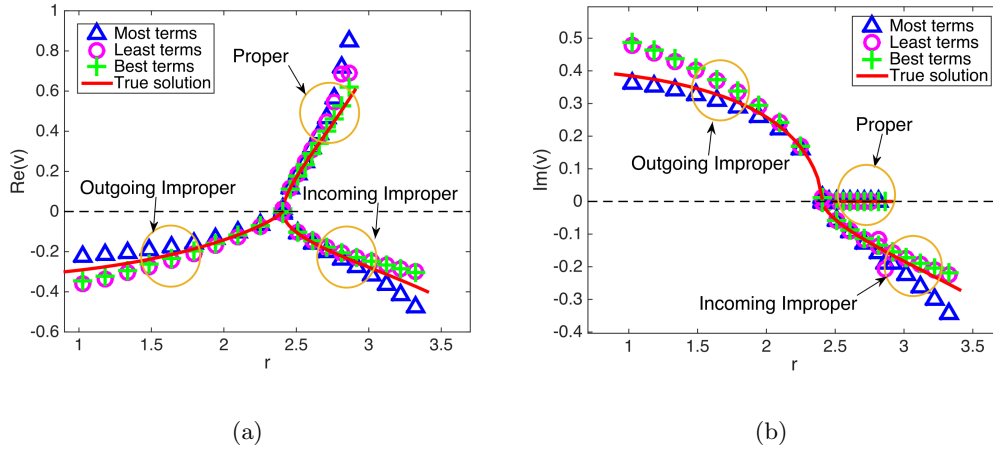
Figure 2.6   With $\kappa = 4$, the initial guess are compared with the numerical solutions around the first cut-off frequency. The most terms, and best terms in the legend refer that $b(r)$, and $c(r)$ are kept with all the terms, and leading terms in Equations (2.33) and (2.34) respectively. The least terms refers that $b(r)$ is with leading term in Equation (2.34), and $c(r) = 0$.

2.2.2 High Frequency Limit

2.2.2.1 Case with $|v| \gg |u| \gg 1$

In the high frequency region ($r \gg 1$), both u, and v are large, namely $v \gg 1$ and $u \gg 1$. Also, in this region $\delta = k_z/k_0$ approaches $\sqrt{\epsilon_{r1}\mu_{r1}}$, which makes $u \gg v$, Under this circumstance $J_m(\cdot)$ and $H_m^{(2)}(\cdot)$ are expanded with large argument [24, 29] by considering the argument in different regions, when $|\arg(z)| < \pi$, Bessel function of the first kind and Hankel function of the second kind are expanded as [24]

$$J_m(z) \sim \sqrt{\frac{2}{\pi z}} \cos(z - \frac{m\pi}{2} - \frac{\pi}{4}) \tag{2.39}$$

and

$$H_m^{(2)}(z) \sim \sqrt{\frac{2}{\pi z}} e^{-j(z - \frac{m\pi}{2} - \frac{\pi}{4})} \tag{2.40}$$

For the case $m = 0$, and $m = 1$, we have $J_1(u)/J_0(u) \approx -u/(v\kappa) \approx 0$ from Equation (2.11), namely $J_1(u) \approx 0$. From the asymptotic form in Equation (2.39) we can further derive $\sin(u - \pi/4) \approx 0$. Consequently, a very simple form in predicting variable u at high frequency range is expressed as $u_0 = \pi/4 + m\pi$, where $m = 1, 2, 3....$ More generally, Equation (2.11) is written as

$$\tan\left(u - \frac{\pi}{4}\right) = -\frac{1}{\kappa}\frac{u}{v} \tag{2.41}$$

For the proper modes, the primary form of v_0 can be derived from Equation (2.9b) as $v_0 = \sqrt{r^2 - u_0^2}$, by substituting this v_0 expression into Equation (2.41), a set of more accurate initial guess expressions for proper modes are obtained as

$$u_1 = \frac{\pi}{4} + m\pi - \tan^{-1}\left(\frac{1}{\kappa}\frac{u_0}{\sqrt{r^2 - u_0^2}}\right) \tag{2.42a}$$

$$v_1 = \sqrt{r^2 - u_1^2}, \quad m = 1, 2, 3... \tag{2.42b}$$

For the improper modes in the third quadrant, the primary form of v_0 is written as $v_0 = -\sqrt{r^2 - u_0^2}$. Following the same steps, more accurate initial guesss expressions for

incoming improper are written as

$$u_1 = \frac{\pi}{4} + m\pi + \tan^{-1}\left(\frac{1}{\kappa}\frac{u_0}{\sqrt{r^2 - u_0^2}}\right) \tag{2.43a}$$

$$v_1 = -\sqrt{r^2 - u_1^2}, \quad m = 1, 2, 3... \tag{2.43b}$$

2.2.2.2   Case with $|u| \gg |v| \gg 1$

Equation (2.43) can be used to predict incoming improper modes for TM and TE cases for the high frequency limit. Another type of solution at the high frequency is $|u| \gg |v| \gg 1$. Through the numerical test, it is found that the value of u and v fluctuate around a constant value from the high frequency region to the low frequency limit for the TE modes. In the other word, Equation (2.43) no longer works for this special case when κ is close to one, and we observed that for these special cases, the argument $z = -jv$ is in the second quadrant and close to the negative real axis with condition of $|u| \gg |v| \gg 1$. Under this circumstance, $H_m^{(2)}(\cdot)$ is re-expanded. This process can be started from expanding $J_m(\cdot)$ with $\arg(z){\approx}\pi$, by using

$$J_m(z) = (-1)^m J_m(-z) \tag{2.44}$$

Accordingly, $J_m(\cdot)$ can be expanded as

$$J_m(z) \sim (-1)^m \sqrt{\frac{-2}{\pi z}}\cos(z + \frac{m\pi}{2} + \frac{\pi}{4}) \tag{2.45}$$

Now, let us derive the asymptotic expression of the Hankel function for the argument z in the second quadrant above the negative real axis and close to π. We know that $H_m^{(2)}(z) = J_m(z) - jY_m(z)$, where $Y_m(z)$ is the Bessel function of the second kind. The phase angle of z is close to π, thus $J_m(-z)$ and $H_m^{(2)}(-z)$ can be well approximated according to Equations (2.39) and (2.40). To express $H_m^{(2)}(z)$ in terms of $J_m(-z)$, and $H_m^{(2)}(-z)$, we can use

$$Y_m(ze^{jm\pi}) = e^{-jnm\pi}Y_m(z) + 2j\sin(nm\pi)\cot(m\pi)J_m(z) \tag{2.46}$$

where m is the order of special function, and n is an integer. For $n = -1$, $ze^{-j\pi} = -z$ is in the fourth quadrant near the positive real axis, the rotation from z to -z does not cross the

branch cut. Equation (2.46) can be further simplified as

$$Y_m(z) = (-1)^m \left[Y_m(-z) + 2jJ_m(-z) \right] \tag{2.47}$$

By substituting $J_m(z) = (-1)^m J_m(-z)$, and having Equation (2.47) into the $H_m^{(2)}(z)$ expression, we have

$$H_m^{(2)}(z) = (-1)^m \left[H_m^{(2)}(-z) + 2J_m(-z) \right] \tag{2.48}$$

Further, substituting Equations (2.40) and (2.45) into Equation (2.48), we finally reach

$$H_0^{(2)}(z) \sim \sqrt{\frac{-2}{\pi z}} \left[e^{j(z+\pi/4)} + 2\cos(z + \pi/4) \right] \tag{2.49a}$$

$$H_1^{(2)}(z) \sim \sqrt{\frac{-2}{\pi z}} \left[-je^{j(z+\pi/4)} + 2\sin(z + \pi/4) \right] \tag{2.49b}$$

Accordingly, the second term of Equation (2.11) is written as

$$\frac{1}{jv} \frac{H_1^{(2)}(-jv)}{H_0^{(2)}(-jv)} = \frac{1}{jv} \frac{3\tan(-jv + \pi/4) - j}{3 + j\tan(-jv + \pi/4)} \tag{2.50}$$

Further, Equation (2.11) is reformed as

$$\frac{v\kappa}{u} \frac{J_1(u)}{J_0(u)} = \frac{3\tanh(v + j\pi/4) + 1}{3 + \tanh(v + j\pi/4)} \tag{2.51}$$

Finally, we have

$$\tanh(v + j\pi/4) = -\frac{1 - 3a(v)}{3 - a(v)} \tag{2.52}$$

where $a(v) = \kappa \dfrac{v}{u} \dfrac{J_1(u)}{J_0(u)}$. Thus, the primary form of initial guess of incoming improper modes is evaluated as

$$v_0 = -\tanh^{-1}(1/3) + j(m - 1/4)\pi, \quad m = -1, -2, -3, ... \tag{2.53}$$

and a more accurate form for v is expressed as

$$v_1 = -\tanh^{-1}\left(\frac{1 - 3a(v_0)}{3 - a(v_0)} \right) + j(m - 1/4)\pi \tag{2.54}$$

2.2.3 Low Frequency Limit

2.2.3.1 TM Case with $\kappa \neq 1$

At low frequency range ($r \ll 1$), due to the solution for two types of improper modes locate in different regions, the corresponding special functions are expanded in different ways. At DC limit, right hand side of Equation (2.10) approaches zero, namely $u^2 + v^2 = 0$, we have $u \approx -jv$, and $v \approx ju$. For the improper modes in the second quadrant, v is in the second quadrant and close to the positive imaginary axis, thus $u \approx -jv$ is in the first quadrant and close to the positive real axis. This indicates that Equation (2.41) still can be employed to derive the initial guesses for the outgoing improper modes. According to the previous discussion, the primary forms of initial guesses for the outgoing improper modes are expressed as

$$u_0 = \pi/4 + m\pi + j \tanh^{-1}(1/\kappa), \quad m = 0, 1, 2, ... \tag{2.55a}$$

$$v_0 = -\sqrt{r^2 - u_0^2} \approx j(\pi/4 + m\pi) - \tanh^{-1}(1/\kappa) \tag{2.55b}$$

However, for the incoming improper modes stop at DC limit, the variable v is around the negative imaginary axis, therefore $u \approx -jv$ is in the second quadrant and close to the negative real axis. In this situation, both $H_m^{(2)}(-jv)$, and $J_m(u)$ have to be expanded around negative real axis, which are shown in Equations (2.45) and (2.48). Correspondingly, we have

$$\frac{J_1(u)}{J_0(u)} \sim \tan(u + \pi/4) \tag{2.56a}$$

$$\frac{H_1^{(2)}(u)}{H_0^{(2)}(u)} \sim \frac{3\tan(u + \pi/4) - j}{3 + j\tan(u + \pi/4)} \tag{2.56b}$$

Equation (2.11) is in a new asymptotic form

$$\tan(u + \pi/4) = \frac{ju}{v} \frac{1}{\kappa} \frac{3\tan(u + \pi/4) - j}{3 + j\tan(u + \pi/4)} \tag{2.57}$$

For $\kappa \neq 1$, it can be further reduced to

$$\tan(u + \pi/4) = \frac{1}{\kappa} \frac{3\tan(u + \pi/4) - j}{3 + j\tan(u + \pi/4)} \tag{2.58}$$

In this quadratic equation $\tan(u + \pi/4)$ is treated as variable. After neglecting one solution which contradicts the assumption, we have

$$\tan(u + \pi/4) = j\tilde{\kappa} \tag{2.59}$$

where

$$\tilde{\kappa} = \frac{3(\kappa - 1) + \sqrt{9(\kappa - 1)^2 + 4\kappa}}{2\kappa}. \tag{2.60}$$

Therefore, the initial guesses for the incoming improper modes stop at DC limit is expressed as

$$u_0 = \pi/4 + m\pi + j\tanh^{-1}(1/\tilde{\kappa}), \quad m = -1, -2, -3, ... \tag{2.61a}$$

$$v_0 = -\sqrt{r^2 - u_0^2} \approx j(\pi/4 + m\pi) - \tanh^{-1}(1/\tilde{\kappa}) \tag{2.61b}$$

2.2.3.2   TE Case with $\kappa = 1$

The Equations (2.55) and (2.61) we have derived are only applicable for $\kappa \neq 1$, like the TM case. To generate the expressions for TE case with $\kappa = 1$, we first exam the value of u at DC limit and find that u has a large value for the imaginary part. As matter of fact, we assume u is in the form of

$$u = \pi/4 + m\pi + ju_I, \quad m = 0, 1, 2, ... \tag{2.62}$$

where the subscript I represents the imaginary part of u. By substituting it into Equation (2.62) into Equation (2.41) with $\kappa = 1$ yields

$$\tanh u_I \approx u_I/\sqrt{r^2 + u_I^2} \tag{2.63}$$

Further Equation (2.63) is written as

$$(r^2 + u_I^2)(1 - e^{-2u_I})^2 = u_I^2(1 + e^{-2u_I})^2 \tag{2.64}$$

After neglecting the higher order terms, we have

$$4u_I^2 e^{-2u_I} \approx r^2 \tag{2.65}$$

The solution to Equation (2.65) is

$$u_I = -W_{-1}(-r/2) \tag{2.66}$$

Similarly, for the incoming improper modes stop at DC limit. We still assume u in Equation (2.57) has the same form of Equation (2.62) but with $m = -1, -2, -3, ...$ Following the same procedure, we have

$$\coth u_I \approx \frac{u_I}{\sqrt{r^2 + u_I^2}} \frac{3 \coth u_I - 1}{3 - \coth u_I} \tag{2.67}$$

u_I is approximated as in Equation (2.66) as well. Consequently, the initial guesses of outgoing improper modes and incoming improper modes stop at DC limit for TE case are expressed as

$$u_0 = \pi/4 + m\pi - jW_{-1}(-r/2) \tag{2.68a}$$

$$v_0 = -\sqrt{r^2 - u_0^2} \approx j(\pi/4 + m\pi) + W_{-1}(-r/2) \tag{2.68b}$$

2.3 Numerical Results and Discussions

The guided and leaky modes of circular waveguide are solved numerically using the initial guesses derived from last section around the cut-off frequency and the high or low frequency limits. The solutions using the second kind of Hankel function on the principal plane are presented in this section. Using the relationship from last section, the solutions using other special functions or in different Riemann sheets can be found. For most examples, normalized complex transverse attenuation constant v is shown because it defines different mode properties as listed in Table 2.1. Several low order proper and outgoing improper modes are shown in Figure 2.7. For the proper modes, there is no propagation in the transverse direction, and it has positive attenuation constant above the cutoff frequency, which is exhibited in Figure 2.7(a). For the convenience of visualization the attenuation constant v for the proper modes are normalized with $k_0 a$. These curves are generated either

from the cutoff frequency using initial guesses according to section 2.2.1, or from the high frequency limit in Equation (2.42). Also from the analysis in the high frequency limit, the asymptotic value for the upper bound is $\sqrt{\mu_{r1}\epsilon_{r1} - \mu_{r2}\epsilon_{r2}}$. As the operating frequency decreases to the cutoff frequency, the proper modes will vanish, and finally convert into the outgoing improper modes. This set of outgoing improper modes can be generated from using the initial guesses derived in section 2.2.1, or using the initial guesses from the low frequency limit with Equation (2.55). Further, they are well indexed from low order to high order according the integer m in Equation (2.55). Some discussions of the physical meaning on the outgoing improper modes have been presented by Kim in [14]. Compared to the outgoing improper modes, the incoming improper modes presented in Figure 2.8 have the opposite sign for the attenuation constants. The magnitude for these two types of improper modes is increasing in the direction away from the waveguide, but propagating in the opposite directions transversely. This set of incoming improper modes which stop at cut off frequency can be predicted by using the initial guesses in Equation (2.38) with $p = 1$ around the each cutoff frequency, or by using the initial guesses in Equation (2.43) at high frequency limit. From the high frequency limit, the asymptotic lower bound is $-\sqrt{\mu_{r1}\epsilon_{r1} - \mu_{r2}\epsilon_{r2}}$.

However, for $\kappa = 4$, except the first three low order modes, the index in Equation (2.55) is not in a one-to-one relationship with the order of modes stop at the cutoff frequency. For instance, the incoming improper modes stop at the fourth cutoff frequency is indexed with $m = 7$ from Equation (2.43). The reason is that Equation (2.43) not only generates the set of incoming improper modes end up at the cutoff frequency but also another type of incoming modes stopping at DC, which have not been presented before. For this type of incoming improper modes stop at DC, they can be predicted from the DC limit by using Equation (2.61), or by using Equation (2.43) as we mentioned before.
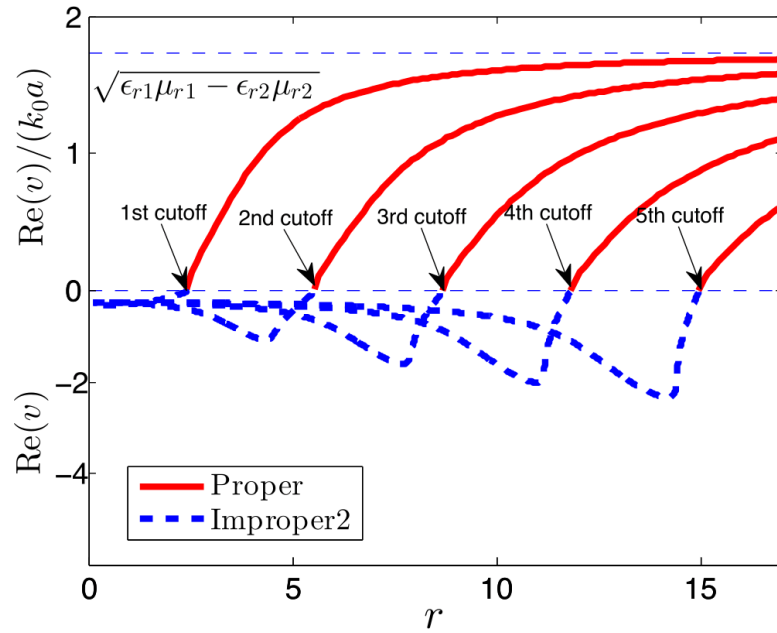
(a)
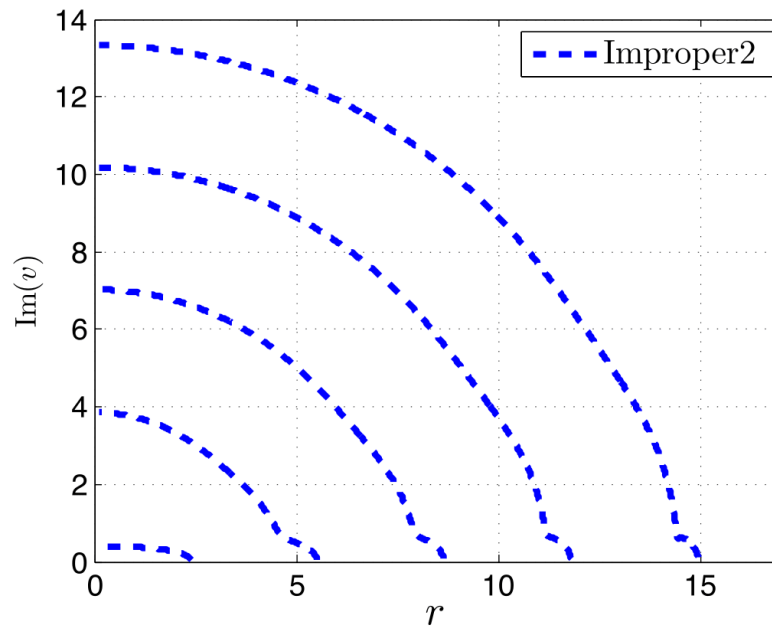
(b)

Figure 2.7   Complex transverse attenuation constants for several low orders proper and outgoing improper modes with $\kappa = 4$. (a) Real parts. (b) Imaginary parts. The Improper2 in the legend represents the outgoing improper modes in the second quadrant.

(a)

(b)

Figure 2.8   Complex transverse attenuation constants for the low order incoming improper mode stop at cutoff frequency with $\kappa = 4$. (a) Real parts. (b) Imaginary parts. The Improper3c in the legend represents the incoming improper in the third quadrant stops at the cutoff frequency.

It is observed from Figure 2.9 that the imaginary part of v is much larger than the real part for the incoming improper modes at DC. This is similar for the outgoing improper modes shown in Figure 2.7, which implies that the imaginary part is dominant in deriving the initial guesses at DC limit for both the incoming improper modes as well as the outgoing improper modes. The corresponding values are $\text{Im}(v) = \pi/4 + m\pi$ for the outgoing case with $m = 0, 1, 2 \ldots$ and $m = -1, -2, -3 \ldots$ for the incoming case. As the absolute value of the index m increases, the initial guess will be more accurate compared to the true value. In contrast, the real part of v is close to a relative small constant at DC limit for both the outgoing and incoming cases. According to Equations (2.55b) and (2.61b), with $\kappa = 4$, the real parts are very close to $-\tan^{-1}(1/\kappa) \approx -0.2554$, and $-\tanh^{-1}(1/\tilde{\kappa}) \approx -0.4531$ respectively. These values are well matched with the numerical results shown in Figure 2.7(a) and Figure 2.9(a) at DC limit. The proper modes exhibited here are the physical modes, which form a complete set and can generally describe an arbitrary field [96]. Correspondingly, the incoming improper modes are nonphysical modes [96], the wave propagates and decays in region 1, and has an exponential growth in the transverse direction in region 2 [97].

The way of deriving the complex transverse propagation constants for TE case is very similar to TM case by using the initial guesses derived in section 2.2, except for the set of initial guess expressions at DC limit for two types of improper modes and the initial guesses at high frequency limit for the incoming improper modes. The transverse attenuation constants of several low orders proper modes and outgoing improper modes for $\kappa = 1$ are shown in Figure 2.10. By comparing with Figure 2.7(a), it is found that the proper modes are always well behaved from cutoff frequency to the high frequency limit. However, for the outgoing improper modes, the real part of v will stop at DC limit with different values. Due to the different values of κ, at DC limit the real parts of v are close to $W_{-1}(-r/2)$ for $\kappa = 1$, and $-\tanh^{-1}(1/\kappa)$ for $\kappa \neq 1$.

(a)
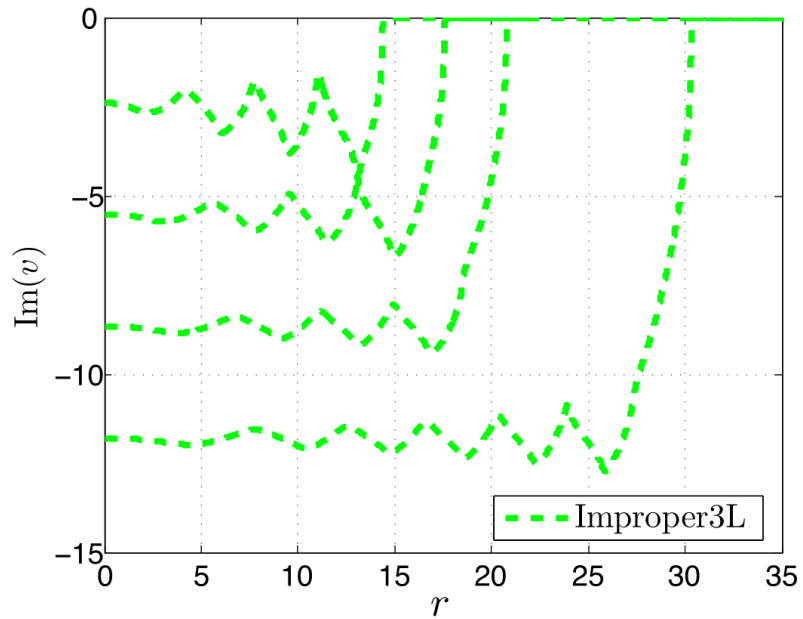
(b)

Figure 2.9   Complex transverse attenuation constants for the low order incoming improper mode stop at DC with $\kappa = 4$. (a) Real parts. (b) Imaginary parts. The Improper3L in the legend represents the incoming improper in the third quadrant stops at the low frequency limit.
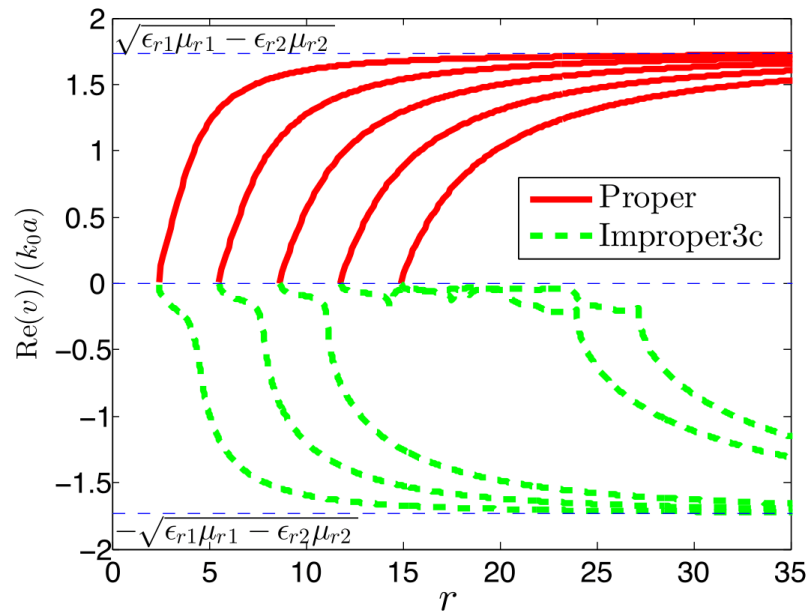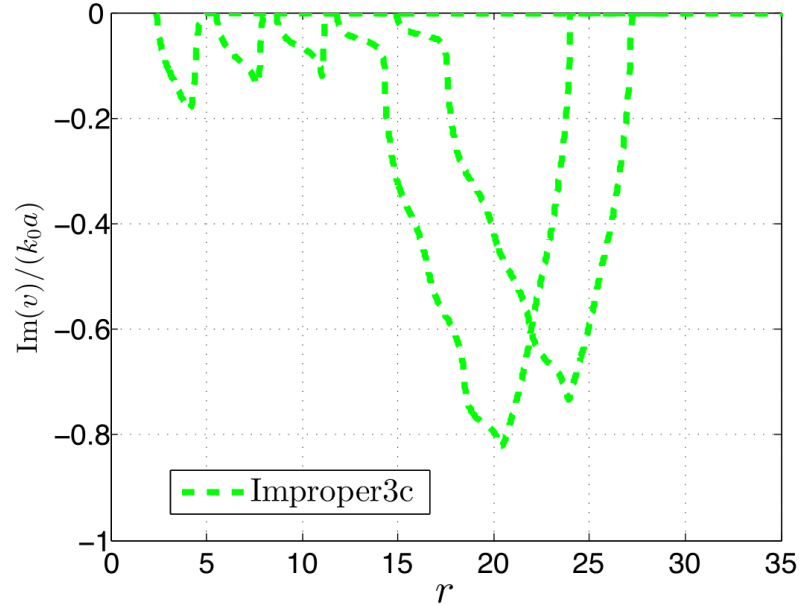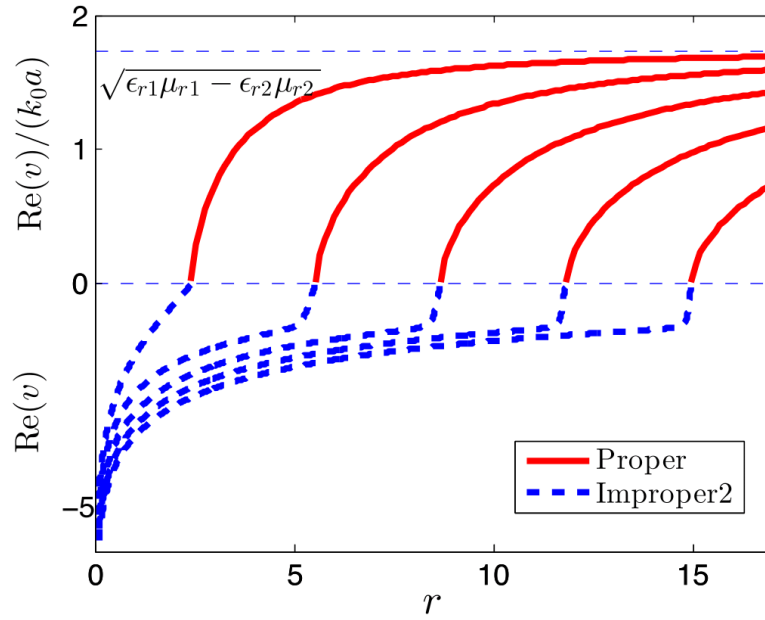
(a)
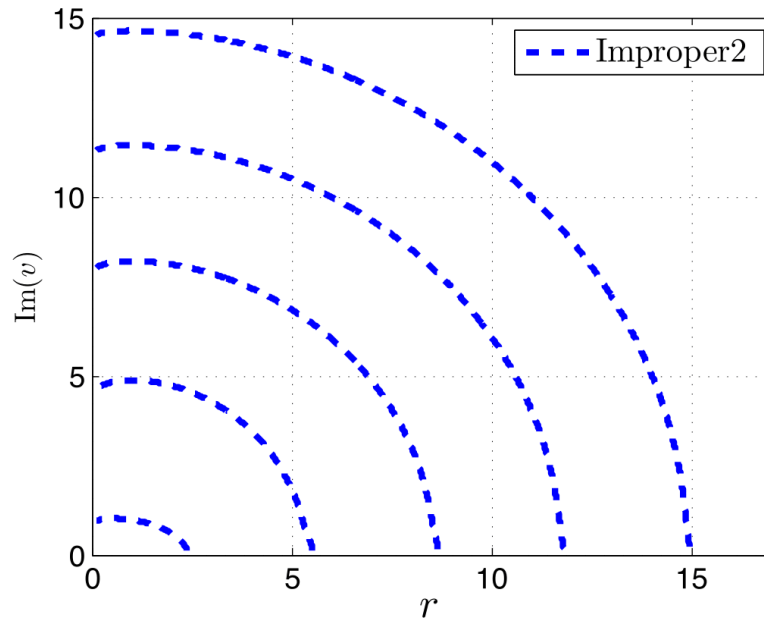
(b)

Figure 2.10   Transverse attenuation constants for several low orders proper modes and outgoing improper modes with $\kappa = 1$. (a) Real parts. (b) Imaginary parts.
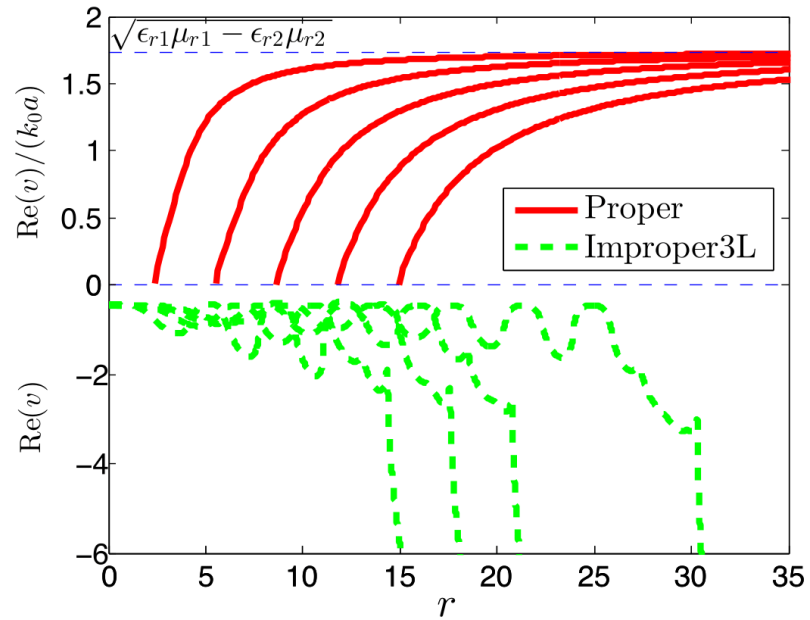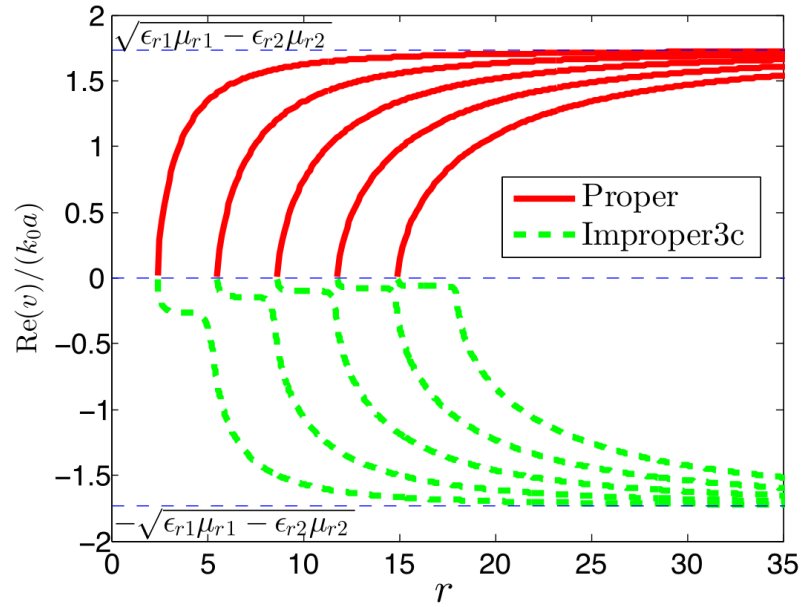
(a)
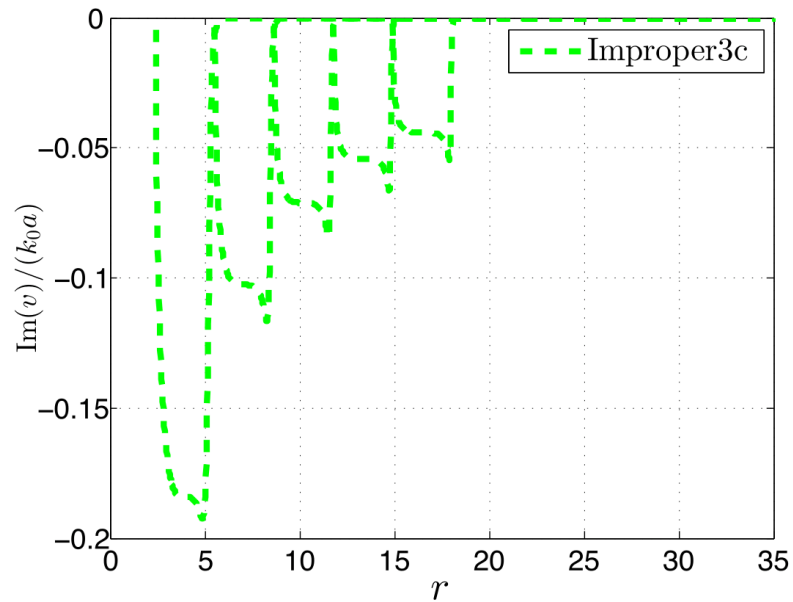
(b)

Figure 2.11   Complex transverse attenuation constants for the low order incoming improper

mode stop at cutoff frequency with $\kappa = 1$. (a) Real part. (b) Imaginary part.
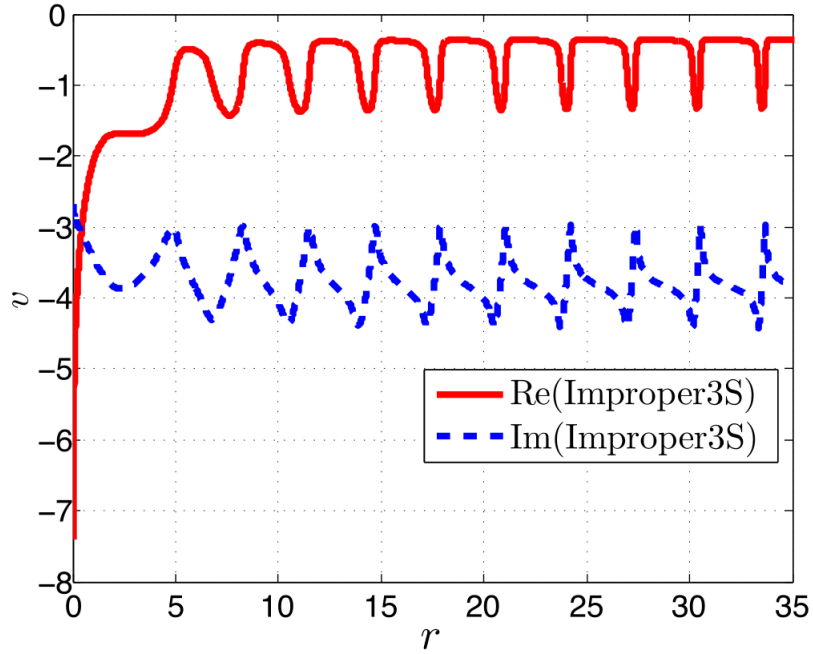
Figure 2.12   Both the real and imaginary parts of the complex transverse attenuation constant for the first TE incoming improper mode ($m = 1$) with $\kappa = 1$. The Improper3S in the legend represents the special case of incoming improper modes in the third quadrant.

Figure 2.11(a) plots the transverse attenuation constant for the low order incoming improper mode stopping at the cutoff frequency. Similarly, by comparing with Figure 2.8, it is found that the dispersion curves are smoother for the higher modes with $\kappa = 1$. However for the incoming improper modes ending up at the DC, the behavior for the TE case shown in Figure 2.12 is different from the TM case. Besides the different value at DC limit, v will approach a constant value through the whole range for both the real and imaginary parts.
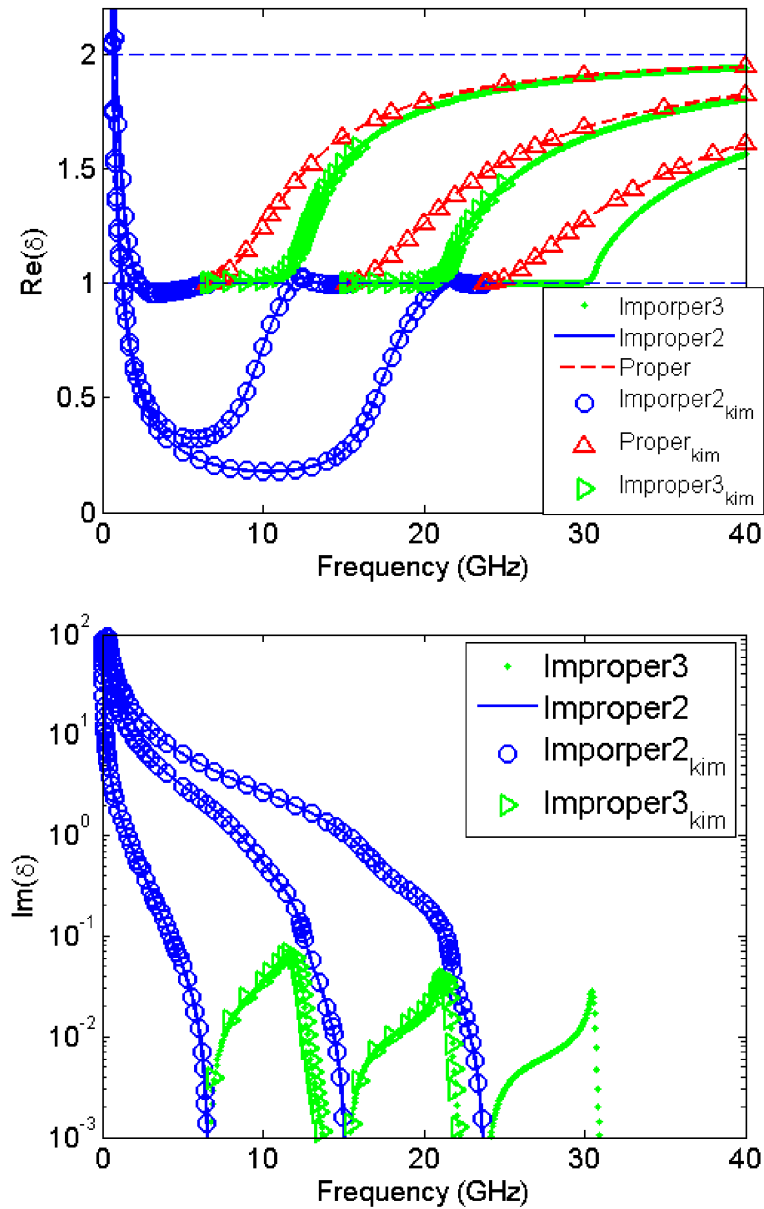
Figure 2.13 The complex longitudinal propagation constants for low order proper, and two types of improper modes. (a) Real part. (b) Imaginary part. The radius for the rod is $a = 0.01$ m, and the dielectric constants inside and outside the rod are $\epsilon_{r1} = 4$ and $\epsilon_{r2} = 1$ respectively.

Our verifications are made by comparing our results with Kim's results [13]. Through the expression of the normalized longitudinal propagation constant $\delta = k_z/k_0$, which can be derived from Equation (2.9b) with given v. Both the real and imaginary parts for several low order modes are illustrated in Figure 2.13. An agreement has been reached between our results and Kim's results. For the other high order incoming improper modes, they are examined by substituting the numerical results into Equation (2.11), and the relative error is down to 10^{-10}.

CHAPTER 3.   ANALYSIS OF GUIDED AND LEAKY MODES IN DOUBLE NEGATIVE CIRCULAR WAVEGUIDE

The analysis of guided and leaky modes for the DPS circular waveguide can be extended to the DNG case. In this chapter, we follow the same procedure as we analyze the conventional circular rod. First, express the characteristic equation for the DNG case, and define different type of modes based on their propagation property. Second, expand the characteristic equation asymptotically and then find the initial guess expressions for different type of modes from different regions. Finally, use these initial guesses solve the characteristic equation with iterative method and plot the dispersion curves.

3.1   Structure and Characteristic Equations

Compared with the structure for the DPS rod, the structure for the uniform DNG rod is the same. This DNG rod is embedded in an infinite homogeneous medium, with radius of a, and it is infinite along the z direction. The structure for the DNG rod is shown in Figure 3.1. Both the permeability and permittivity for the rod are negative.
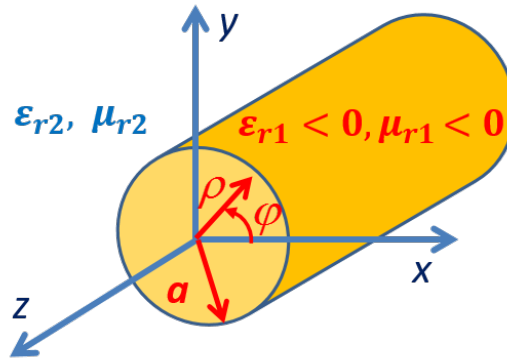
Figure 3.1   Circular rod with negative permittivity and permeability.

By applying the continuity conditions of tangential fields to this DNG rod, the characteristic equation for TM and TE cases can be derived by imposing $m = 0$ [27, 28], which means the modes are without variations along the circular angle. Under this circumstance, the characteristic equation for the DNG rod can be expressed as

$$\frac{\kappa}{u}\frac{J_1(u)}{J_0(u)} + \frac{1}{jv}\frac{H_1^{(2)}(-jv)}{H_0^{(2)}(-jv)} = 0 \tag{3.1}$$

Again, we assign $\kappa = \epsilon_{r1}/\epsilon_{r2}$ or $\kappa = \mu_{r1}/\mu_{r2}$ and $\kappa < 0$, Equation (3.1) represents TM or TE case, where ϵ_{ri} and μ_{ri} are the relative permittivity and permeability respectively. The second subscript $i = 1$ represents the region within the rod, where ϵ_{r1} and μ_{r1} are negative, and $i = 2$ represents the region outside the rod. $J_m(\cdot)$ and $H_m^{(2)}(\cdot)$ are the m-th order Bessel function of the first kind and Hankel function of the second kind. For the DNG case, the value for κ can be various. We will focus on the case where $|\kappa| \geq 1$ in this chapter. In Equation (3.1), u and v are expressed as

$$u \triangleq k_0 a\sqrt{\mu_{r1}\epsilon_{r1} - \delta^2} \tag{3.2a}$$

$$v \triangleq k_0 a\sqrt{\delta^2 - \mu_{r2}\epsilon_{r2}} \tag{3.2b}$$

where k_0 is the wave number in free space. $\delta = k_z/k_0$, and k_z is the axial complex propagation constant. Therefore, r is given by

$$r = \sqrt{u^2 + v^2} = k_0 a\sqrt{\mu_{r1}\epsilon_{r1} - \mu_{r2}\epsilon_{r2}} \tag{3.3}$$

The format of Equation (3.1) is exactly same as Equation (2.11) in Chapter 2, thus the details for the derivation will not be repeated here. Although the format of two equations are the same, due to the negative permeability and permittivity property, which leads the rod to have negative refraction index, the wave propagation property will be different physically. For example, the DNG rod will potentially support the Poynting vector of the wave anti-parallel to the direction the phase flow of it. From the equation perspective, this kind of difference is reflected from the negative value of κ in Equation (3.1). The dispersion

curves for the DNG case can be further different from those in the DPS case, which will be presented in the later part of this chapter. For Equation (3.1) we will still treat the transverse complex propagation constant v as unknown, and define different type of modes based on their wave behavior outside the rod along the radial direction as we did in 2.1.2. The classification of the modes is the same as the one shown in Table 2.1, and the mode definitions will be used in the later discussion.

The analysis for the relationship between special functions and corresponding propagation constants in 2.1.3, and the complex conjugate properties for the lossless rod in 2.1.4 still hold for the DNG rod case. We can directly use these conclusions without deriving them repeatedly.

3.2   Initial Guesses for DNG Rod

3.2.1   Around the Cutoff Frequency

For the DNG circular rod, all the analysis procedures and conclusions are the same as 2.2.1 in Chapter 2. Thus the detail procedures in expanding Hankel function and Bessel functions efficiently in finding the accurate initial guess will be skipped here. Only the general form of the initial guess expression and the table for its corresponding relationship with different type of modes will be presented here.

$$v = 2a_1^{-1} e^{\frac{1}{2}W_p(z(r))} \tag{3.4}$$

where $W_p(z)$ represents the Lambert W function [24, 25], subscript p denotes the p-th branch, $z(r) = a_1^2 c_1/2$, $a_1 = e^{\gamma - 1/2\kappa}$, $c_1(r) = -\chi_{0n}(r - \chi_{0n})/\kappa$, χ_{0n} denotes the n-th root of zero order Bessel function of the first kind, and $\gamma \approx 0.577215664$ is the Euler constant. Equation (3.4) can predict different types of modes for the DNG rod with appropriate branches of Lambert W function. The corresponding branch and sign choices are summarized as

Table 3.1   Corresponding branches to derive different types of modes for DNG rod

| | Proper Modes | Improper Modes | |
		Outging	Incoming
p value	-1	1	
$\text{sign}(r - \chi_{0n})$	$(-)$	$(+)$	$(-)$
$\text{sign}(z)$	$(-)$	$(+)$	$(-)$

3.2.2   High Frequency Limit ($|v| \gg |u| \gg 1$)

After examining the values of u and v in the high frequency region ($r \gg 1$), it is found $|v| \gg |u| \gg 1$. Under this circumstance $J_m(\cdot)$ and $H_m^{(2)}(\cdot)$ are still expanded with large argument as Equation (2.39) and (2.40) in 2.2.2. The simplest form in predicting variable u at high frequency range is expressed as $u_0 = \pi/4 + m\pi$, where $m = 1, 2, 3....$. The more accurate initial expression can be derived by first rewritten Equation (3.1) as

$$\tan\left(u - \frac{\pi}{4}\right) = -\frac{1}{\kappa}\frac{u}{v} \tag{3.5}$$

For the proper modes, the primary form of v_0 can be derived from Equation (3.2b) as $v_0 = \sqrt{r^2 - u_0^2}$, by substituting this v_0 expression into Equation (3.5), a set of more accurate initial guess expressions for real proper modes are obtained as

$$u_1 = \frac{\pi}{4} + m\pi - \tan^{-1}\left(\frac{1}{\kappa}\frac{u_0}{\sqrt{r^2 - u_0^2}}\right) \tag{3.6a}$$

$$v_1 = \sqrt{r^2 - u_1^2}, \quad m = 1, 2, 3... \tag{3.6b}$$

The initial expression in Equation (3.6) is the same as Equation (2.42) we derived for the DPS case. However, the corresponding relationship between the modes and the index m is different from DPS case. Here, $m = 1$ corresponds to the real proper mode stop at the second cutoff frequency, and $m = 2, 3, 4...$ corresponds to the higher order modes with ascending order of cutoff frequencies. For the improper modes in the second quadrant, the primary form is $v_0 = -\sqrt{r^2 - u_0^2}$. Following the same steps, a more accurate initial guess

expression for outgoing improper modes are written as

$$u_1 = \frac{\pi}{4} + m\pi + \tan^{-1}\left(\frac{1}{\kappa}\frac{u_0}{\sqrt{r^2 - u_0^2}}\right) \tag{3.7a}$$

$$v_1 = -\sqrt{r^2 - u_1^2}, \quad m = 1, 2, 3... \tag{3.7b}$$

3.2.3   Low Frequency Limit

At low frequency range ($r \ll 1$), we expand special functions in different ways, due to the solutions for the complex proper mode and the incoming improper mode locate in different regions. At DC limit, the right hand side of Equation (3.3) approaches zero, namely $u^2 + v^2 = 0$, we have $u \approx -jv$, and $v \approx ju$. For the complex proper modes in the first or fourth quadrants, v is found to be in the first quadrant and close to the positive imaginary axis, thus $u \approx -jv$ is in the fourth quadrant and close to the positive real axis.

This indicates we could still expand $J_m(u)$ and $H_m^{(2)}(-jv)$ off the negative real axis ($|\arg(z)| < \pi$). However, the situation for the DNG case is more complicated compared with the DPS case. To derive the accurate initial guess expressions for the complex proper modes with different values κ, we need to keep more terms in the first order expansion of $J_m(z)$ and $H_m^{(2)}(z)$

$$J_m(z) \sim \sqrt{\frac{2}{\pi z}}\left[\cos(z - \frac{m\pi}{2} - \frac{\pi}{4}) - \sin(z - \frac{m\pi}{2} - \frac{\pi}{4})\frac{(4m^2 - 1)}{8z}\right] \tag{3.8}$$

and

$$H_m^{(2)}(z) \sim \sqrt{\frac{2}{\pi z}}e^{-j(z - \frac{m\pi}{2} - \frac{\pi}{4})}\left[1 - j\frac{(4m^2 - 1)}{8z}\right] \tag{3.9}$$

By plugging in the asymptotic expressions from Equations (3.8) and (3.9) into Equation (3.1), we have

$$\kappa\frac{\tan(u - \pi/4) + \dfrac{3}{8u}}{1 + \dfrac{1}{8u}\tan(u - \pi/4)} = -\frac{u}{v}\frac{1 + \dfrac{3}{8v}}{1 - \dfrac{1}{8v}} \tag{3.10}$$

we can further assume $u = \pi/4 + ju_I$, where u_I is the imaginary part of u. For low frequency limit $|u| \gg r$, and $v = ju\sqrt{1 - r^2/u^2} \approx ju(1 - r^2/(2u^2))$. Thus, Equation (3.10) can be further written as

$$\kappa \frac{\tanh u_I - \dfrac{3j}{8u}}{1 + \dfrac{j}{8u} \tanh u_I} = \left(1 + \frac{r^2}{2u^2}\right) \frac{1 - \dfrac{3j}{8u}}{1 + \dfrac{j}{8u}} \tag{3.11}$$

For Equation (3.11), we can further simplify it by neglecting the high order terms as

$$\left[\kappa + \frac{j(\kappa - 1)}{8u}\right] \tanh u_I \approx 1 + \frac{r^2}{2u^2} + (\kappa - 1)\frac{3j}{8u} \tag{3.12}$$

For $\kappa < -1$, with large value of u, $\tanh u_I \approx 1/\kappa$ can be derived from Equation (3.12). Correspondingly, we have $u_I \approx \tanh^{-1}(1/\kappa)$.

This indicates Equation (3.5) can still be employed to derive the initial guesses for the complex proper modes. This procedure is very similar to the derivation of the outgoing improper modes for the DPS case at the low frequency limit in 2.2.3. The initial guesses for the complex proper modes are expressed as

$$u_0 = \pi/4 + m\pi + j\tanh^{-1}(1/\kappa), \quad m = 1, 2, 3... \tag{3.13a}$$

$$v_0 = \sqrt{r^2 - u_0^2} \approx j(\pi/4 + m\pi) - \tanh^{-1}(1/\kappa) \tag{3.13b}$$

In Equation (3.13), the lowest index $m = 1$ corresponds to the mode related to the second order real proper modes, and $m = 2, 3, 4...$ corresponds to the higher order complex proper modes related to 3rd, 4th, 5th ... order of real proper modes.

For $\kappa = -1$, $u_I < 0$, both u and u_I are of large values, $\tanh u_I = (e^{2u_I} - 1)/(e^{2u_I} + 1)$ can be approximated as

$$\tanh u_I = -1 + 2e^{2u_I} \tag{3.14}$$

To further derive the equations, we can neglect $r^2/(2u^2)$ in Equation (3.12) first and simplify it as

$$\tanh u_I \approx -1 + \frac{j}{u} \tag{3.15}$$

By combining Equation (3.15) and Equation (3.14) together we have

$$2ue^{2u_I} = j \tag{3.16}$$

With $u_I = -j(u - \pi/4)$, Equation (3.16) can be further simplified, and the initial guess expression of v is written as

$$v = -\frac{1}{2}W_{-m}(-j) \quad m = 1, 2, 3... \tag{3.17}$$

For the incoming improper modes of the DNG case, its property is very similar to the incoming improper modes for the DPS case. At DC limit, the variable v is around the negative imaginary axis, correspondingly $u \approx -jv$ is in the second quadrant and close to the negative real axis. Therefore we need to expand both $H_m^{(2)}(-jv)$ and $J_m(u)$ around the negative axis according to Equation (2.45) and (2.48) respectively, and rewrite Equation (3.1) as

$$\tan(u + \pi/4) = \frac{ju}{v}\frac{1}{\kappa}\frac{3\tan(u + \pi/4) - j}{3 + j\tan(u + \pi/4)} \tag{3.18}$$

The derivation of Equation (3.18) can refer to 2.2.2.2 in Chapter 2. For $\kappa \neq 1$, Equation (3.18) can be further reduced to

$$\tan(u + \pi/4) = \frac{1}{\kappa}\frac{3\tan(u + \pi/4) - j}{3 + j\tan(u + \pi/4)} \tag{3.19}$$

In Equation (3.19) $\tan(u + \pi/4)$ is treated as variable. In stead of neglecting one of the two solutions in the DPS case, here we need to keep both of the solutions to catch all the incoming improper modes at low frequency limit. Consequently, we will have

$$\tan(u + \pi/4) = j\tilde{\kappa}^{\pm} \tag{3.20}$$

where

$$\tilde{\kappa}^{\pm} = \frac{3(\kappa - 1) \pm \sqrt{9(\kappa - 1)^2 + 4\kappa}}{2\kappa} \tag{3.21}$$

Therefore, the initial guesses for the incoming improper modes stop at DC limit are expressed as

$$u_0^{\pm} = \pi/4 + m\pi + j\tanh^{-1}(1/\tilde{\kappa}^{\pm}), \quad m = -1, -2, -3, ... \tag{3.22a}$$

$$v_0^{\pm} = -\sqrt{r^2 - (u_0^{\pm})^2} \approx j(\pi/4 + m\pi) - \tanh^{-1}(1/\tilde{\kappa}^{\pm}) \tag{3.22b}$$

3.2.4 Special Treatment for Evanescent Mode

Unlike the first order real proper in the DPS case, whose initial guess can be predicted easily from the high frequency limit or around the cutoff. For the DNG case, with different values of κ, the first order real proper mode shows the low frequency limit behavior or high frequency limit behavior different from other higher order real proper modes.

In order to derive the first order real proper mode completely, different values of κ from low frequency limit or high frequency limit. We first employ the characteristic Equation (2.12). For real proper modes, In v is real, $u = j\sqrt{v^2 - r^2}$ is pure imaginary. Thus, Equation (2.12) can be rewritten as

$$\frac{\kappa}{\sqrt{v^2 - r^2}}\frac{I_1(\sqrt{v^2 - r^2})}{I_0(\sqrt{v^2 - r^2})} + \frac{1}{v}\frac{K_1(v)}{K_0(v)} = 0 \tag{3.23}$$

where $I_n(v)$ is the modified Bessel functions of the first kind. When $|\arg(v)| < \pi$, modified Bessel function of the first kind and second kind are expanded as [24]

$$I_m(v) \sim \frac{e^v}{\sqrt{2\pi v}}\sum_{k=0}^{\infty}(-1)^k\frac{a_k(m)}{v^k} \tag{3.24}$$

$$K_m(v) \sim e^{-v}\sqrt{\frac{\pi}{2v}}\sum_{k=0}^{\infty}\frac{a_k(m)}{v^k} \tag{3.25}$$

where $a_0(m) = 1$, and $a_k(m) = (4m^2 - 1)(4m^2 - 3^2)\cdots(4m^2 - (2k-1)^2)/(k!8^k)$, with $k \geq 1$. For the case when $m = 0$, and $m = 1$, $I_1(v)/I_0(v) = (8v - 3)/(8v + 1)$, and $K_1(v)/K_0(v) = (8v + 3)/(8v - 1)$. When $\kappa = -1$, the first order real proper mode has a high frequency limit. Under this circumstance $v \gg r \gg 1$, we can plug the expansion

expressions of $I_1(\sqrt{v^2 - r^2})/I_0(\sqrt{v^2 - r^2})$ and $K_1(v)/K_0(v)$ into Equation (3.23), and keep the first two terms

$$v - \sqrt{v^2 - r^2} = \frac{1}{8}\left[2 + 3\left(\frac{v}{\sqrt{v^2 - r^2}} + \frac{\sqrt{v^2 - r^2}}{v}\right)\right] \tag{3.26}$$

For the high frequency limit, as $v \gg r$, the right hand side of Equation (3.26) approach one. After further simplification of Equation (3.26), we have

$$v \approx r^2/2 \tag{3.27}$$

For the low frequency limit $r \ll 1$, when $\kappa < -1$, Equation (3.23) can be simplified as

$$\frac{\kappa}{v}\frac{I_1(v)}{I_0(v)} + \frac{1}{v}\frac{K_1(v)}{K_0(v)} = 0 \tag{3.28}$$

For large value of positive $\mathrm{Re}(v)$, we can still plug in the asymptotic expansion expressions of $I_1(v)/I_0(v)$ and $K_1(v)/K_0(v)$, then we will have

$$v = \frac{\kappa - 1}{2(\kappa + 1)} \tag{3.29}$$

3.3 Numerical Results and Discussions

The guided and leaky modes for the DNG circular waveguide are solved with Newton-Raphson method [95] using the initial guesses derived from the previous section around the cut-off frequency and the high or low frequency limits. To maintain unity, the solutions presented in this section are still solved by using characteristic equation with the second kind of Hankel function on the principal plane. For the numerical examples, normalized or unnormalized complex transverse attenuation constant v will be shown according to the modes defined in Table 2.1.

Several low order proper and complex proper modes are shown in Figure 3.2. Compared with the real modes for the DPS circular rod, the real proper modes for the DNG own the same feature of not propagating in the transverse direction, and meanwhile have positive attenuation constants above the cutoff frequency. This property is illustrated in Figure 3.2.

45

However, the real proper modes for the DNG case are not exactly same as the DPS case. The difference mainly comes from two aspects. First, from the dispersion curve shown in Figure 3.2 we found that the normalized propagation constant does not monotonically increase as r increases, for the small region below the cutoff frequency, the normalized propagation constant increases as r decreases. This indicating a backward wave propagation [13], which is evidence from the negative slope in part of the dispersion curve for the real proper mode. For this backward wave region, the Poynting vector is anti-parallel to the direction of the phase flow. Second, compared with the real proper modes in the DPS case, instead of directly converting into the improper modes below the cutoff, the real proper modes for the DNG case can also convert into complex proper modes at point A shown in Figure 3.2, which is treated as a critical point [13]. These real proper modes are generated either from the cutoff frequency using initial guess expression in Section 3.2.1, or from the high frequency limit in Equation (3.6). What should be emphasized here again is that the first order real proper mode ($m = 0$) is different from other higher order modes, this first order real mode stops at DC, which is shown clearly in Figure 3.3. For this special mode, besides deriving it around cutoff frequency, we can derive it from low frequency limit as well. For this case, $v \approx 0.8186$ as shown in Figure 3.3 is very close to 5/6 calculated from Equation (3.29). From the analysis in the high frequency limit, the asymptotic value for the upper bound is still $\sqrt{\mu_{r1}\epsilon_{r1} - \mu_{r2}\epsilon_{r2}}$ for DNG case.
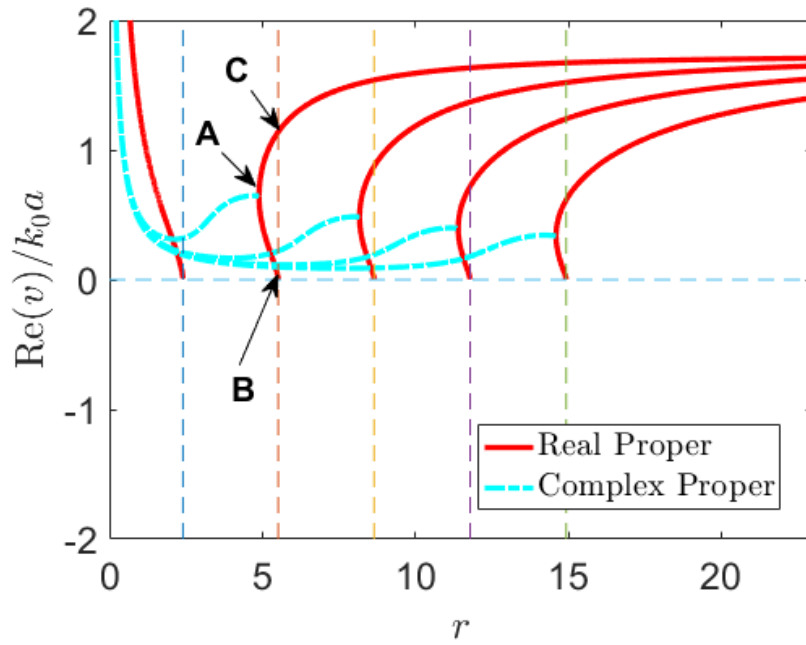
(a)
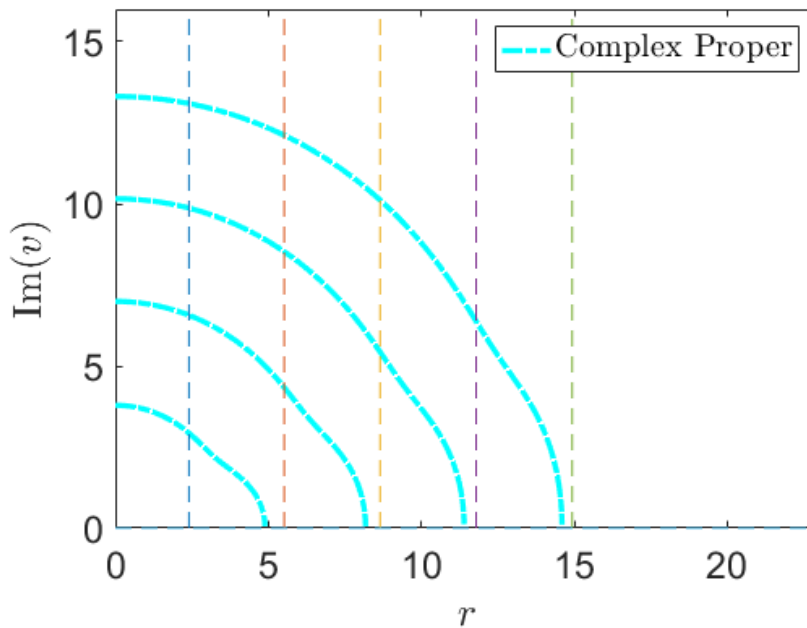
(b)

Figure 3.2   Complex transverse attenuation constants for several low orders real proper and complex proper modes of DNG rod with $\kappa = -4$. (a) Real parts. (b) Imaginary parts.

For a better visualization, the real part of the unnormalized complex proper modes in shown in Figure 3.3. This complex proper modes only exist in the DNG case, it starts from the low frequency limit, and extends to the critical point, and then bifurcates into two branches of real proper modes AB and AC. This complex proper modes can be only predicted from the low frequency limit by using Equation (3.13). For the case of $\kappa = -4$, the real part for the low frequency limit for the complex proper modes can be evaluated from $-\tanh^{-1}(1/\kappa) \approx 0.2554$, which is consistent with numerical results shown in Figure 3.3.

As the operating frequency decreases to the cutoff frequency as shown as Point B on Figure 3.2 and Figure 3.3 , the real proper modes will vanish, and the improper modes appear. Very similar to the DPS case, there are two types of improper modes related to the DNG case. For the outgoing improper modes, which is above the cutoff frequency. The dispersion curve for this type of improper modes is demonstrated in Figure 3.4. There are two ways to derive this outgoing improper modes as we mentioned in the previous sections, one is around the cutoff frequency using Equation (3.4) with $p = -1$ shown in Table 3.1, the other one is from the high frequency limit according to Equation (3.7)

This set of outgoing improper modes can be generated from using the initial guesses derived in Section 2.2.1, or using the initial guesses from the high frequency limit with Equation (3.7). Further, they are well indexed from low order to high order according the integer m in Equation (3.7). Similar to the real proper modes, the outgoing improper mode has a low bound asymptotic value of $-\sqrt{\mu_{r1}\epsilon_{r1} - \mu_{r2}\epsilon_{r2}}$ at high frequency limit.

Besides the outgoing improper modes, there is another type of improper modes, which is operating under the cutoff frequency. This type of incoming improper mode has not been demonstrated in Kim's work [13]. For the convenience of visualization, the unnormalized incoming improper modes are demonstrated in Figure 3.5. There are two possible ways to derive this type of improper modes as well. The first method is starting from the cutoff region, by using Equation (3.4) with $p = 1$. The numerical results are presented in Figure

3.5. Although deriving different types of modes near the cutoff region is convenient, it provides relative less information to connect the initial guess expression with the order of modes. Based on this consideration, we are always trying to access the same type of modes in different ways to build more connections between the initial guess expressions and the numerical results. The second way to derive this incoming improper modes is from the low frequency limit by using Equation (3.22). From v_0^+ we can access the incoming improper modes related to the odd order cutoff except the first order, and from v_0^- we can access the incoming improper modes related to the rest of the cutoff.

A more intuitive plot is shown in Figure 3.6. The dash pink lines represent the set of modes from v_0^+, and the solid green lines represent the rest of modes from v_0^-. For the set of pink curves, their real parts will focus to a constant value at the low frequency limit. This constant value can be derived as $\mathrm{Re}(v_0^+) \approx \mathrm{Re}(-\tanh^{-1}(1/\tilde{\kappa}^+)) \approx -0.0680$ using Equation (3.22) . Correspondingly, for the set of green curves, the real parts will merge to another constant value at low frequency limit. This constant value is derived from $\mathrm{Re}(v_0^-) \approx \mathrm{Re}(-\tanh^{-1}(1/\tilde{\kappa}^-)) \approx -0.2786$. The low frequency limit for the imaginary part of the incoming improper modes are from $\mathrm{Im}(v_0^\pm)$, where $\mathrm{Im}(v_0^-) \approx \pi/4 + m\pi + \mathrm{Im}(-\tanh^{-1}(1/\tilde{\kappa}^-)) \approx \pi/4 + m\pi$ for the group of green lines, and $\mathrm{Im}(v_0^+) \approx \pi/4 + m\pi + \mathrm{Im}(-\tanh^{-1}(1/\tilde{\kappa}^+)) \approx \pi/4 + m\pi + \pi/2$ for the group of pink lines.
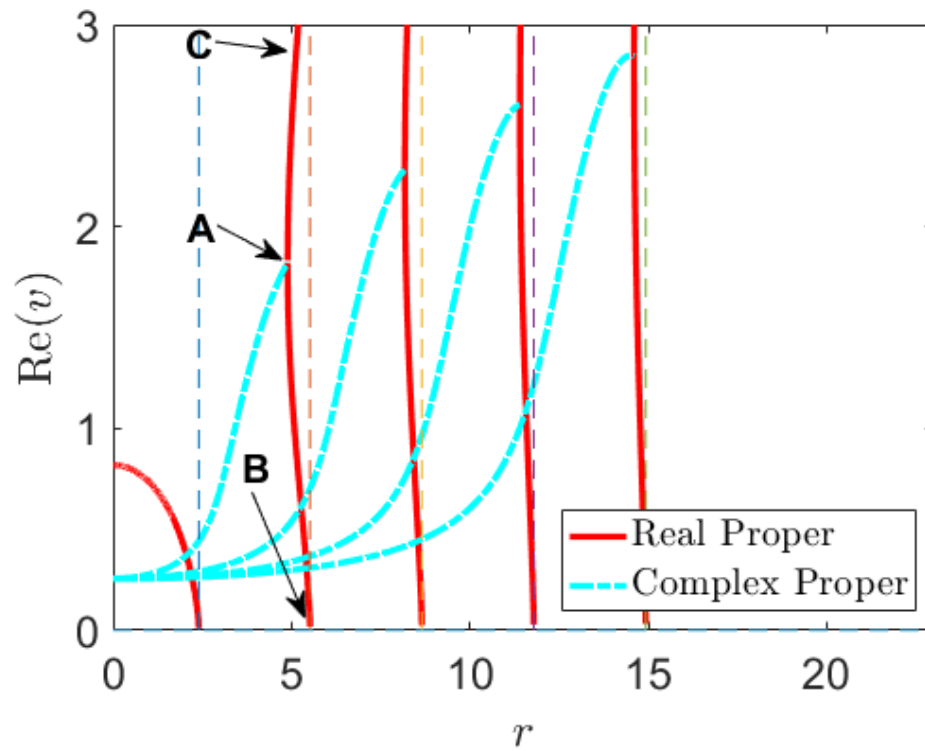
Figure 3.3   Real part of the transverse attenuation constants for several low order real proper and complex proper modes increases with $\kappa = -4$.
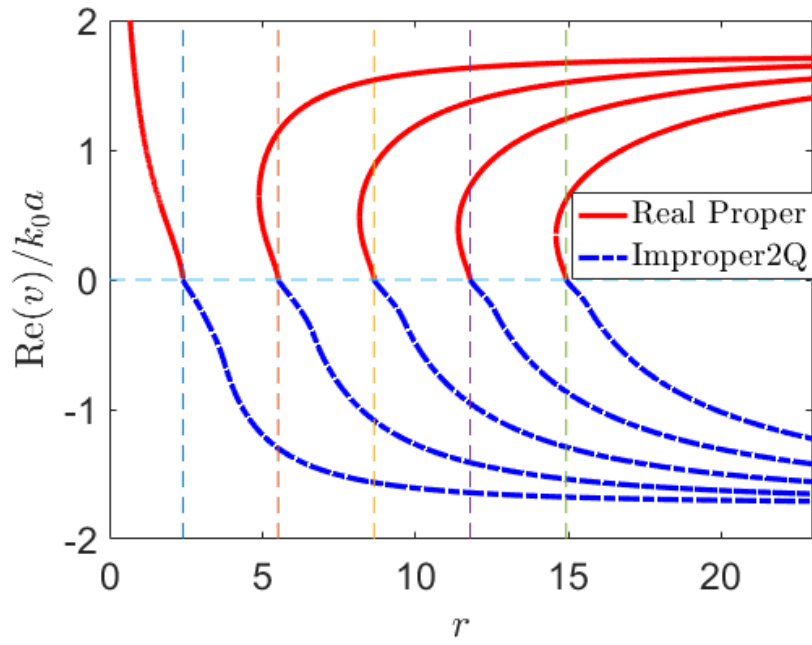
(a)
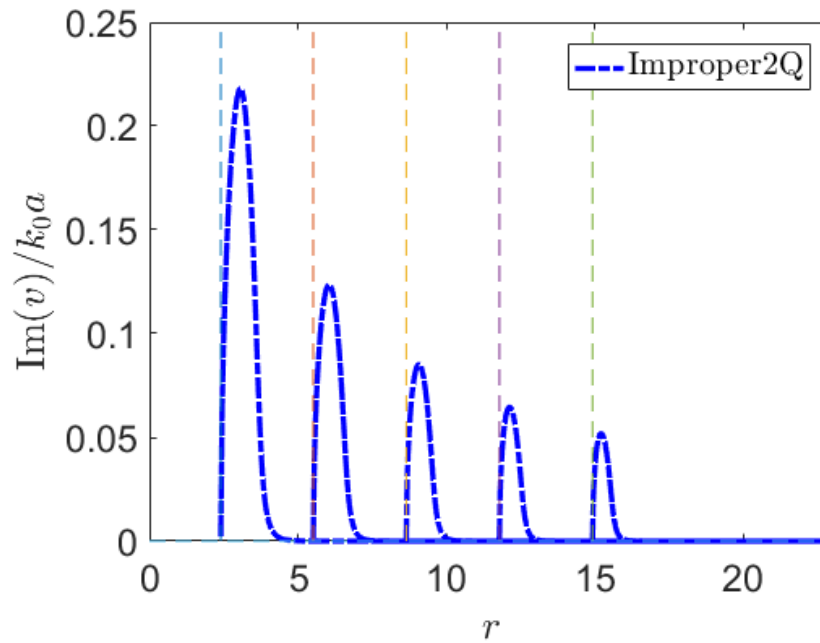
(b)

Figure 3.4   Complex transverse attenuation constants for several low order real proper and

outgoing improper modes with $\kappa = -4$. (a) Real parts. (b) Imaginary parts.

(a)

(b)

Figure 3.5   Complex transverse attenuation constants for several low order real proper and

incoming improper modes with $\kappa = -4$. (a) Real parts. (b) Imaginary parts.
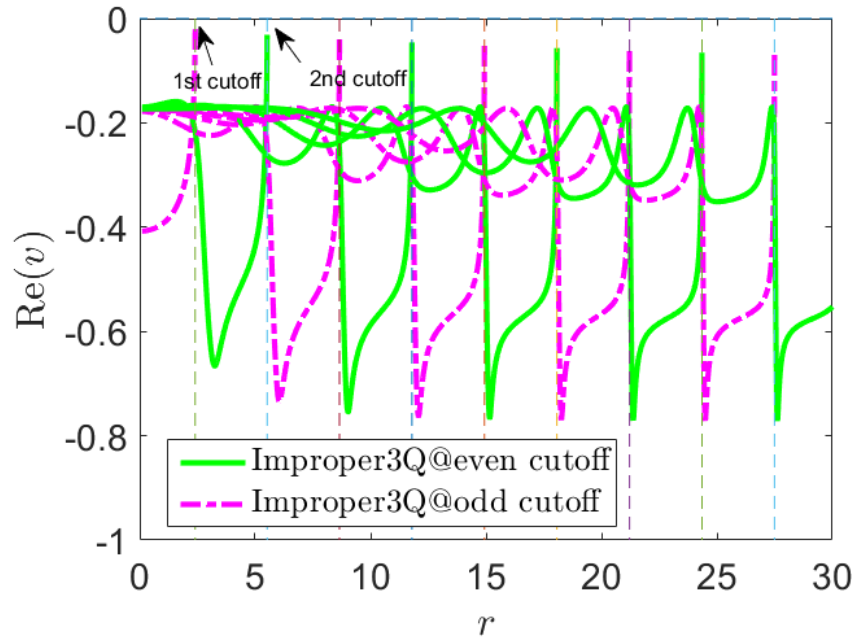
(a)
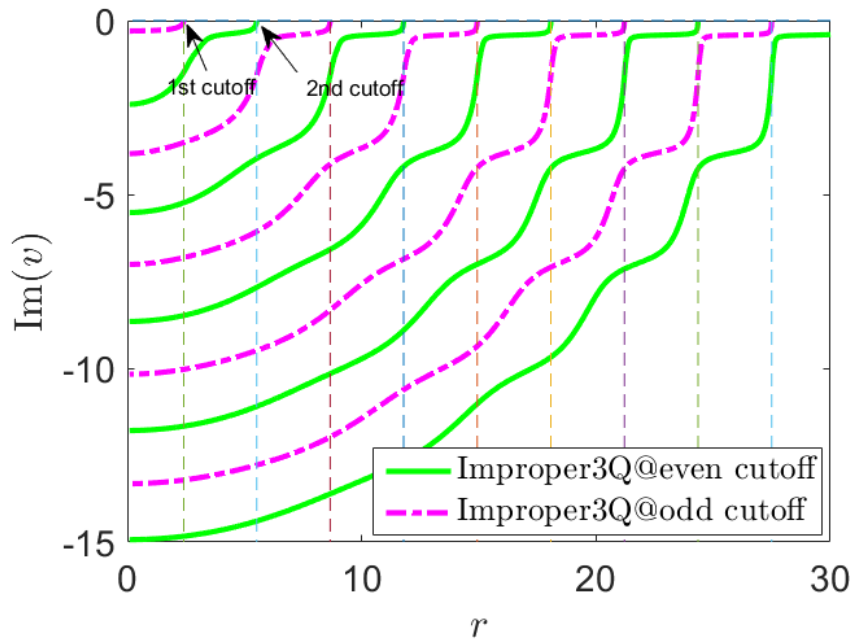
(b)

Figure 3.6   Complex transverse attenuation constants for several incoming improper modes

with $\kappa = -4$. (a) Real parts. (b) Imaginary parts.

53

Compared to the case $\kappa = -4$, the way to derive numerical results for case $\kappa = -1$ is very similar, except some difference at high and low frequency limit behaviors, which are consequence from different value of κ through the initial guess derivations.

Several low order proper and complex proper modes are shown in Figure 3.7. Comparing with the unnormalized real parts of complex proper modes shown in Figure 3.3 and the unnormalized imaginary parts in Figure 3.2 (b), it can be observed that the behavior for the imaginary parts are very similar from cutoff to the low frequency limit. However, the low frequency limit behaviors for the real parts are different. Unlike the case for $\kappa = -4$, where the real parts can be evaluated from $-\tanh^{-1}(1/\kappa)$, for $\kappa = -1$ the real parts for complex proper modes are evaluated from Equation (3.17) and correspondingly the real parts can be calculated from $\text{Re}[(-1/2)W_{-m}(-j)]$, where $m = 1, 2, 3...$ is the mode order.

The normalized real proper modes and outgoing improper modes for case $\kappa = -1$ are demonstrated in Figure 3.8. The numerical results for outgoing improper modes are almost the same for cases $\kappa = -1$ and $\kappa = -4$. All the outgoing improper modes can be derived from high frequency limit with Equation 3.7 or from cutoff frequencies as shown in Section 2.2.1. The behaviors of the real proper modes demonstrated in Figure 3.8 is very similar to the real proper modes shown in Figure 3.4 except the first order real proper modes. For case $\kappa = -1$, instead of stop at the low frequency limit, it will go and rise to the high frequency limit. This special behavior for the first order real proper mode can be either derived from the cutoff or from the high frequency limit by using Equation 3.27. In this case, with $\kappa = -1$, $r = \sqrt{3}k_0a$ and $v/(k_0a) = \sqrt{3}r/2 \approx 0.866r$. Correspondingly, in Figure 3.8 when $r = 25$, $v/k_0a \approx 21.65$.

The behavior of the incoming improper modes for $\kappa = -1$ are demonstrated in Figure 3.9.
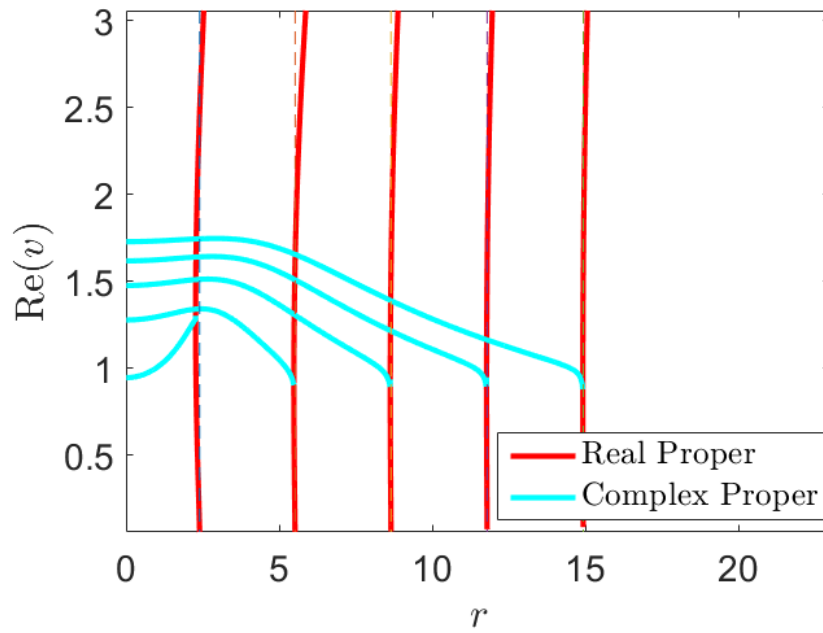
(a)
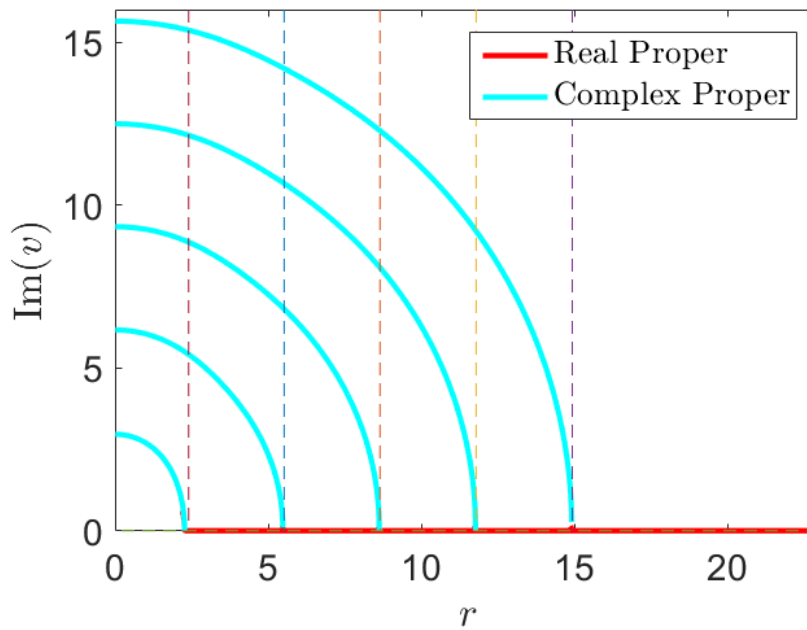
(b)

Figure 3.7   Complex transverse attenuation constants for several low order real proper and

outgoing improper modes with $\kappa = -1$. (a) Real parts. (b) Imaginary parts.
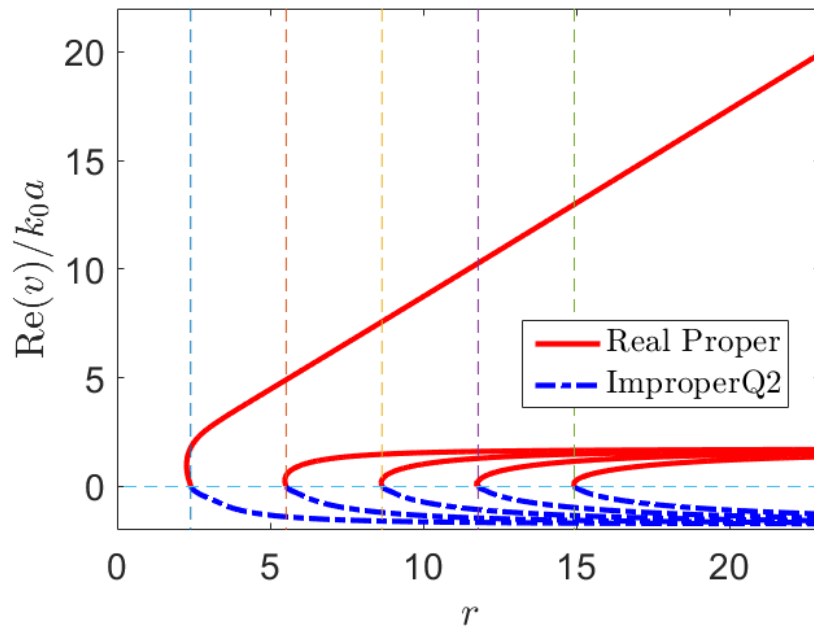
(a)
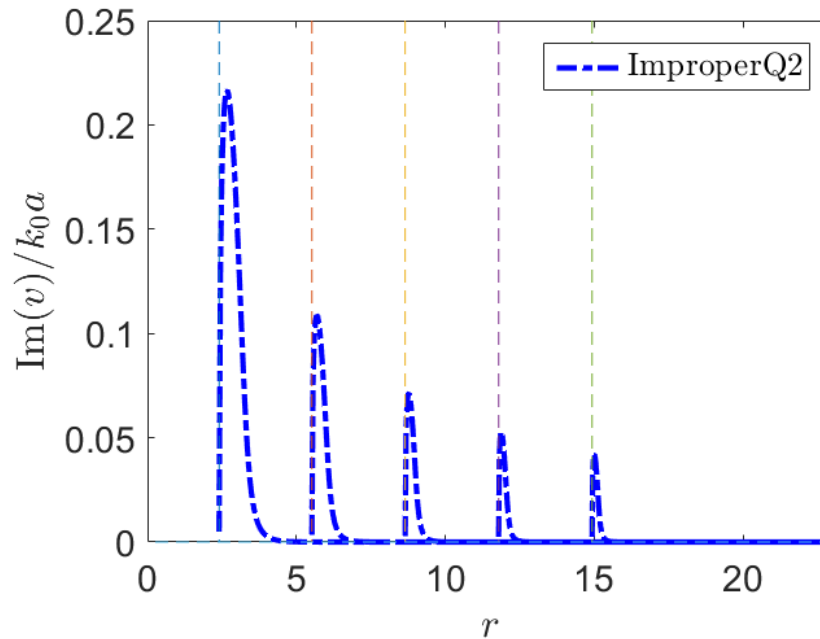
(b)

Figure 3.8   Complex transverse attenuation constants for several low order real proper and

outgoing improper modes with $\kappa = -1$. (a) Real parts. (b) Imaginary parts.
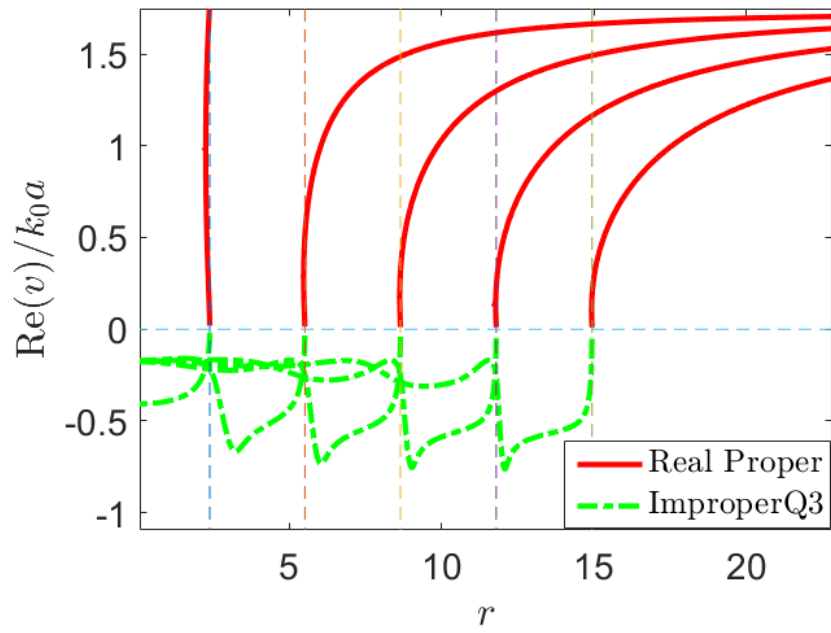
(a)
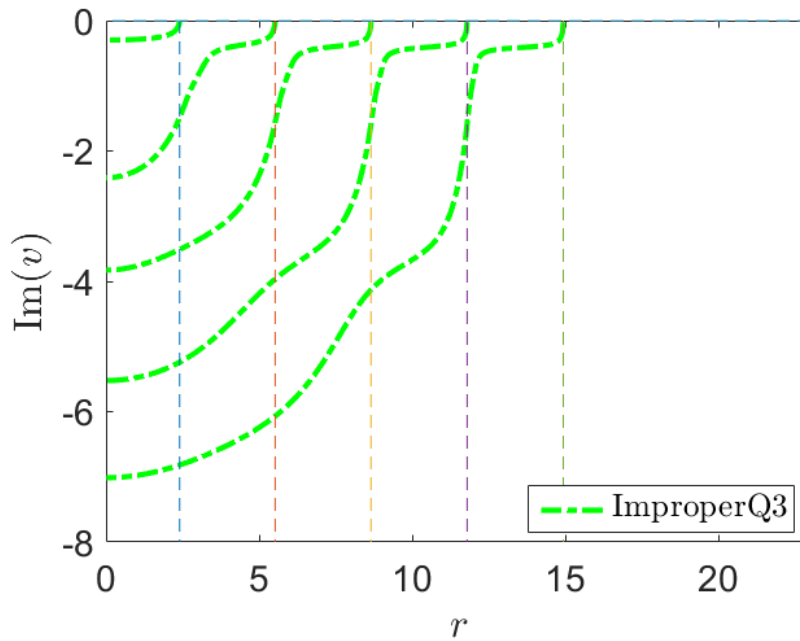
(b)
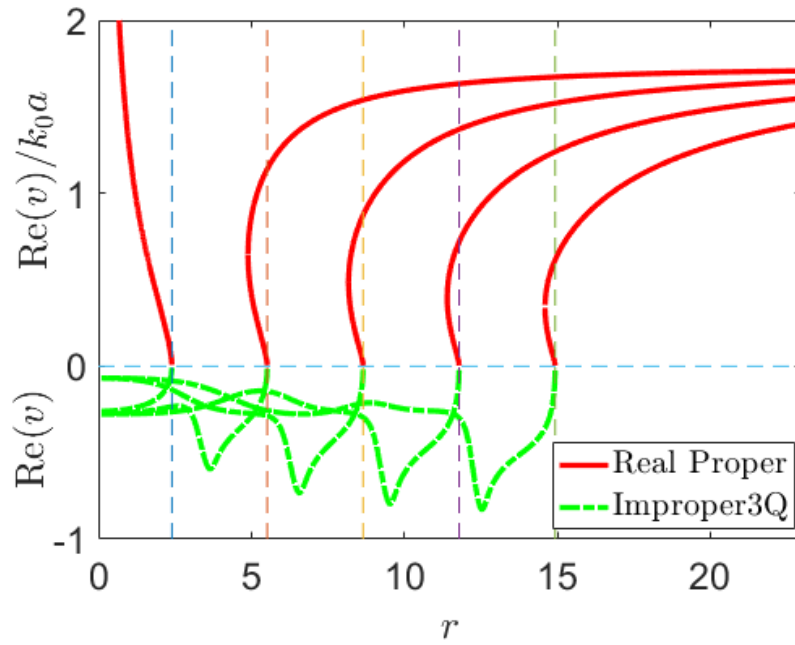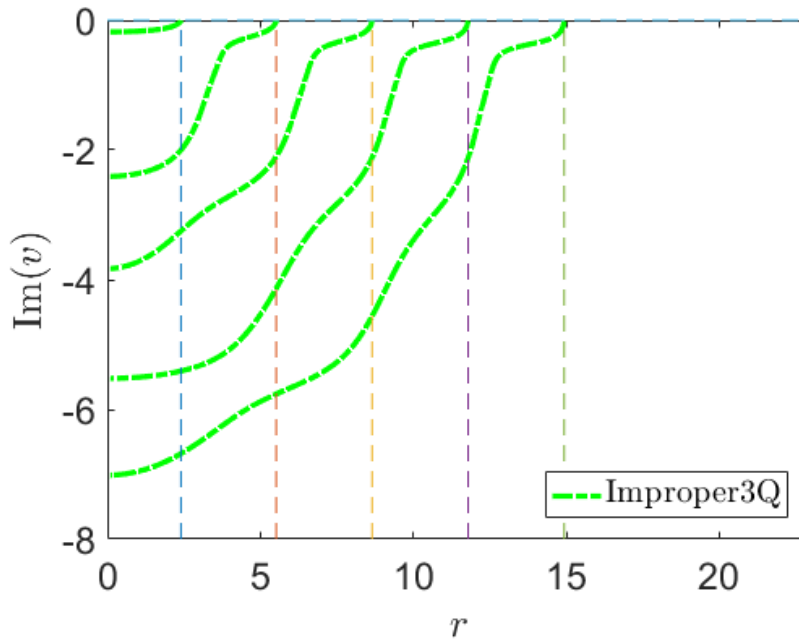
Figure 3.9   Complex transverse attenuation constants for several low order real proper and

outgoing improper modes with $\kappa = -1$. (a) Real parts. (b) Imaginary parts.

# CHAPTER 4. MECHANICALLY TUNABLE COMPLIANT META-ATOMS

4.1 Metamaterial-Overview

Matematerials are fascinating artificial materials that can manipulate electromagnetic wave in surprising ways. Their structure is usually composed of subwavelength metallic resonators hold by dielectric. As the 'unit' element of metamaterial, these periodical metallic resonators could change the electromagnetic properties of the metamaterial through interacting with incidence wave.

Seminal explorations of artificial materials in manipulating electromagnetic waves can be dated back to the end of the 19th century. The earliest structures that may be considered as metamaterials are substances with chiral properties. The term "metamaterial" is initially specifically referring to those artificially designed electromagnetic structure with unusual electromagnetic properties that are rarely found in nature, later the meaning of so-called "metametarial" is extended to other types, such as elastic and acoustic [98, 99].

In the process of studying metamaterial, Russian physicist Veselago first theoretically predicted extraordinary electromagnetic property of metamaterial with a simultaneously negative permittivity and permeability, such as the reversal of Snell's law, a reversed Doppler effect [100]. Through his analysis, this type of material is treated as left-handed material, since electric field, magnetic field, and propagation vector obey the left-handed rule. However, his prediction was not widely accepted until Smith's *et al* [63] experimental materialization in 2000 by using split-ring resonators (SRRs) [101] and continuous wires [102]. These were first introduced by Pendry [101]-[103], who suggested that they can also act as perfect lenses [104]. Later, various kinds of new structures have been proposed and realized [105, 106] based SRRs and thin wires.

Although there is no consensus on the definition of metametarial currently, the common attributes of metametarial can be concluded as [107]: (1) The structures are described with homogenized electromagnetic parameters; (2) they are usually based on conducting, resonant inclusions, which will finally determine the electromagnetic parameters; (3) the resonator inclusions are positioned periodically; (4) the scale of periodicity is smaller—usually by a factor of 5 to 10 times—than that of the free-space wavelength of excitation. Structure with these feature made it distinguished from the existing artificial material categories.

In terms of the real permittivity and permeability, normal dielectrics typically occupy the domain where both quantities are positive. Negative values of the permittivity can be obtained in nature through the radiation-plasma interaction, but this interaction is typically the occurred well beyond the infrared for those solid-state plasmas. To realize the negative permittivity at lower frequency, thin-wire lattices [102] are adopted to dilute the plasma cloud and shift the plasma frequency to a lower part of the spectrum. The negative permeability is rare in nature, it can be obtained from magnetic resonances in ferromagnets at submicrowave frequencies, such as split-ring resonators (SRRs) [101]. This structure can exhibit magnetic dipole and negative permeability in response to magnetic waves. Free tuning the electric and magnetic responses of metamaterials brings about the possibility to realize double-negative materials or negative-index materials (NIMs), in which both the permittivity and permeability are less than zero at the same frequency. Such materials have not yet been found in nature, and the first realization of NIMs exploits the combined operations of wires and SRRs at the same microwave frequency to generate overlapping negative permittivity and permeability [63]. Due to this unusual behavior, NIMs have raised a wide interest in metamaterials and become the center of metamaterial research aimed at operation in the visible frequency range [108]-[110] for different kinds of applications.

4.2   Desgin and Electromagnetic Simulation

In this part of the thesis we present a novel tunable and flexible SRR-based meta-atom capable of tuning its EM response characteristics over a broad frequency range by simple mechanical stretching. The present meta-atom used a liquid metal as the resonator material. The liquid metal was patterned to be a SRR structure and embedded inside a highly stretchable silicone elastomer. Due to its liquid nature, the liquid metal-based SRR could flow in response to an applied strain, and thus, was not prone to fatigue or cracking. When the encasing elastomer was stretched and twisted, the SRR was shown sufficiently compliant to yield the necessary deformation. Therefore, by changing the shape of the SRR via simple mechanical stretching, the gap distance and thus the gap capacitance of the SRR could be adjusted, thus tuning the resonance response of the meta-atom. Material of this chapter is based on co-paper published in JAP [111] with Co-author Peng Liu [112]
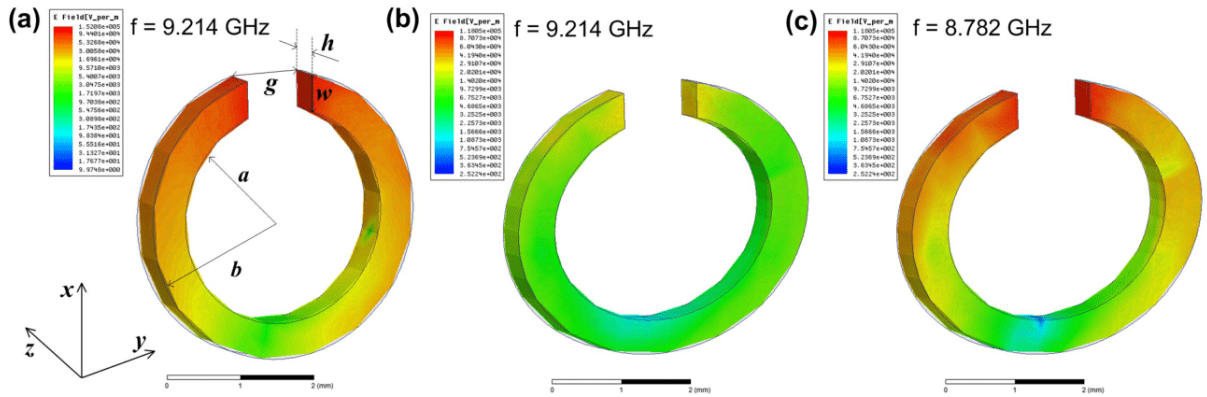
Figure 4.1   The simulated magnitude of the electric field ($\boldsymbol{E}$) distributions in the tunable liquid metal SRR at the resonance frequency of 9.214 GHz when not stretched (a), at 9.214 GHz when stretched by 30% along the y direction (b), and at the new resonance frequency of 8.782 GHz when stretched (c) .

To test the concept of the mechanical tuning, the liquid metal SRR was designed to operate in the X-band frequency range. While many other types of liquid metal could be used, the present SRR used eutectic gallium-indium or EGaIn (75.5% gallium and 24.5% indium),

a liquid at room temperature and a solid at 14°C, because of its favorable attributes, such as high electrical conductivity, low toxicity, and light weight. Structurally, the liquid metal SRR had the inner radius of $a = 1.5$ mm, the outer radius of $b = 2.0$ mm, the thickness of $h = 0.5$ mm, and the gap of $g = 1.0$ mm. The SRR was encased by Ecoflex, a highly stretchable silicone elastomer with the maximal elongation at break of 900%. It's noteworthy that Ecoflex is thermally curable and suitable for replica molding from a master mold, just like polydimethylsiloxane, a commonly used elastomer used in soft lithography. The length, width, and thickness of the Ecoflex encasing membrane were $l = 11.0$ mm, $w = 7.5$ mm, and $t = 1.45$ mm, respectively. To illustrate the influence of the mechanical stretching on the resonance of the SRR, the Ansys high frequency structure simulator (HFSS) software was employed to conduct the EM simulations. As shown in Figure 4.1, the SRR was fixed in the $x - y$ plane inside a waveguide and the magnetic field (**H**) was parallel to the z direction and penetrated through the SRR, thus exciting the magnetic resonance. The simulation result shows that when the gap of the SRR was aligned along the y direction, the resonance frequency of the SRR before stretch was at 9.214 GHz (Figure 4.1(a)). Applying the stretch of 30% along the y direction led to an increase in the gap of the SRR along the same direction (Figure 4.1(b)). Consequently, the SRR was brought out of resonance at the 9.214 GHz and resonated at the new frequency of 8.782 GHz (Figure 4.1(c)). We note that the simulation here only conceptually illustrated the proposed tuning concept. The more quantitative simulation results are presented later, together with the experimental results.

Figure 4.2 shows the fabrication process flow for the proposed tunable meta-atom. First, to form the SRR-shaped microchannels, an 800-μm-thick Ecoflex layer L1 was cast upon a master mold made of SU-8 photoresist on a silicon (Si) wafer W1, and then, was fully cured at 60°C on a hotplate for 30 mins (Figures 4.2(a)-(b)). In a parallel process, a 100-μm-thick Ecoflex thin layer L2 was spin-coated on another Si wafer W2, followed by partial curing at 50°C on a hotplate for 40s (Figure 4.2(c)). Subsequently, the layer L1 was peeled off from the master mold and adhered to the partially cured layer L2. The two layers

L1 and L2 were then permanently and thermally bonded together on a hotplate at 90°C for 30 mins (Figure 4.2(d)). After the two bonded layers were peeled off from the wafer W2, the liquid metal EGaIn was injected into the embedded microchannels through two 100-μm-diameter holes mechanically punched at the two ends of each microchannel. There were some residues of the eutectic alloy remaining around the holes on the top surface of the Ecoflex structure. To clean the top surface, a cotton swab was dipped in a solution of hydrochloric acid (50%, v/v) and then carefully wiped off any residues from the top surface (Figure 4.2e). To encapsulate the liquid metal inside the Ecoflex elastomer, a new Ecoflex prepolymer solution was poured onto the cleaned top surface, followed by a full curing process performed at 80°C on a hotplate for 30 mins (Figures 4.2(f)-(g)). Therefore, the liquid metal SRRs were formed inside the elastomer. The total thickness of the elastomer was 1.45 mm as mentioned. The SRRs were located nearly at half the thickness of the elastomer. Lastly, individual SRRs were diced out of the whole elastomer for testing [112].
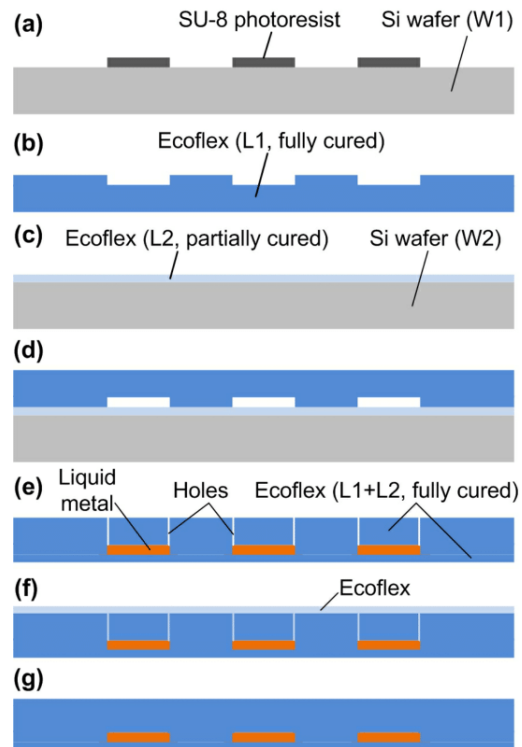
Figure 4.2   The fabrication process for the tunable liquid metal SRR.

4.3   Device Measurement

EM measurements were carried out over the X-band using a WR90 rectangular waveguide (22.86 × 10.16 mm) terminated by a UG39/U cover flange. When the waves propagate in the waveguide, the directions of **E** and **H** are along the short edge and the long edge of the waveguide, respectively. The walls of the waveguide act as reflective mirrors and make the SRR cell behave as an element in a 2D quasi-periodic structure with normal incidence wave. The SRR sample was attached onto a wood slab (low-loss microwave substrate material) and centered in the middle of the waveguide. The spectra were measured using a programmable vector network analyzer (Agilent E8364) [112].
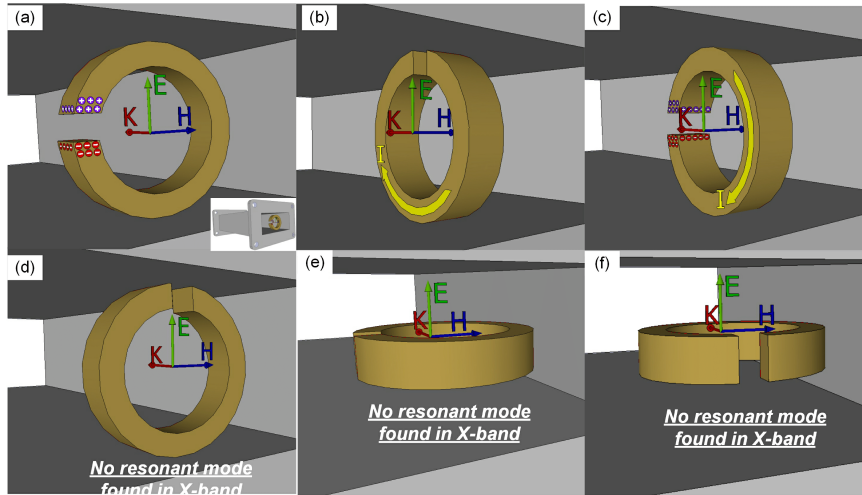
Figure 4.3   The six possible arrangements of the SRR inside a testing waveguide. The inset in (a) shows the relative location of the ring to the waveguide. The electric dipole formed by opposite electric charges accumulating across the gap of the ring couples the SRR resonance to the electric field of the incident waveguide mode in (a) and (c). The magnetic moment due to the loop current couples to the incident magnetic field normal to the ring plane in (b) and (c). No coupling to the resonance was found in (d), (e), and (f) in X-band

There were six possible placements of the SRR inside the waveguide, as illustrated in Figure 4.3, among which three (Figures 4.3(a), 4.3(c), and 4.3(d)) could excite the resonance of the circular ring current in the SRR structure (magnetic dipole resonance). The SRR dimensions were chosen such that this resonance would occur within the X-band for the stretched and unstretched samples. Figure 4.3(a) displays that the incident wave was normal to the plane of the ring and the electric field was parallel to the gap direction. In this configuration the electric dipole formed across the gap allows coupling of the electric field of the waveguide mode to the magnetic dipole resonance of the SRR because of the broken symmetry of the ring with respect to the direction of **E**. In the case shown in Figure 4.3(c), both, the electric moment across the gap driven by the incident **E** field and the magnetic moment of the circular ring induced by the incident **B** field current jointly excite the resonance of the ring. Figure 4.3d shows that the magnetic field was normal to the plane of the ring, thus exciting a circulating current in the ring the induced magnetic moment. Neither electric dipole nor magnetic moment could couple to the incident waveguide mode in the other three configurations shown in Figures 4.3(b), 4.3(e), and 4.3(f).

Theoretically, the unit SRR can be treated as a LC loop, where L is the equivalent net inductor from the SRR loop and C is the equivalent net capacitor from the charge accumulation in the gap region, and hence the resonance frequency of a SRR unit is estimated as:

$$f = \frac{1}{2\pi\sqrt{CL}} \tag{4.1}$$

Both the inductance and capacitance of the SRR unit will change as unit cell being stretched in different directions, which finally shift the resonance frequency according to Equation 4.1.

In this set of experiments, there are two possible stretching manners. One is stretching the unit cell along the gap direction; the other is stretching the unit cell perpendicular to the gap direction. These two types of stretching lead different deformations to the unit cell, which will finally present different electromagnetic responses.

64

(a)   (b)
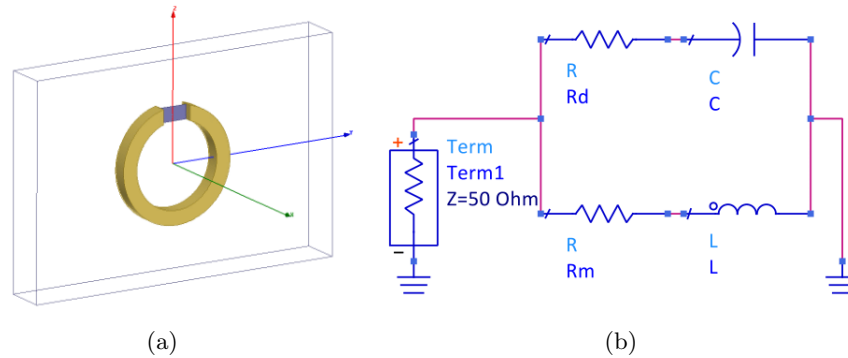
Figure 4.4   (a)Schematic of SRR unit in the free space, a delta source is set along the gap.
(b) The equivalent circuit for the SRR as shown in (a)

In order to have a better understanding of the trend of shifting resonance frequency shown in the experiment, simulations are carried out in HFSS based on single unit cell in the free space. In this simulation, a delta-gap source is set along the gap direction to excite the unit cell, which is shown in Figure 4.4(a), and the impedances are measured by sweeping the frequencies we are interested with. A one port equivalent circuit is designed to describe the resonance behavior of the stretching SRR unit, which is shown in Figure 4.4(b). The equivalent circuit takes consideration of the equivalent inductor (L), and the equivalent capacitor (C), as well as the dielectric loss (R_d) from the substrate, metallic loss (R_m) from the liquid metal. The lumped L and C are obtained by optimizing the impedance of equivalent circuit according to the simulated impedances around resonant frequency with less than 3% of relative error for each stretching case.

The setup in this simulation is not exactly same as the set up in the experiment, which is excited within a waveguide where interaction with the metal wall may exist. However, compared with the effect from the mutual interaction with metal walls, the deformation of the unit cell is considered to contribute most to the changes of resonant frequencies. As matter of fact, we expect the simulation of stretching SRR in the free space to reveal the resonance shifting trend.
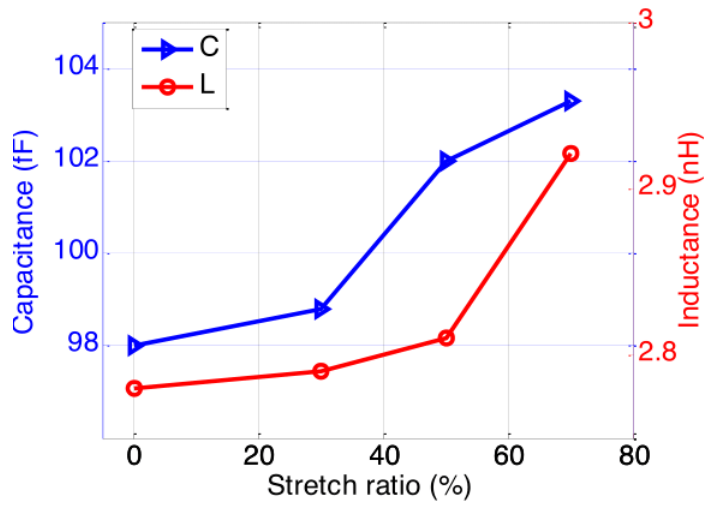
(a)
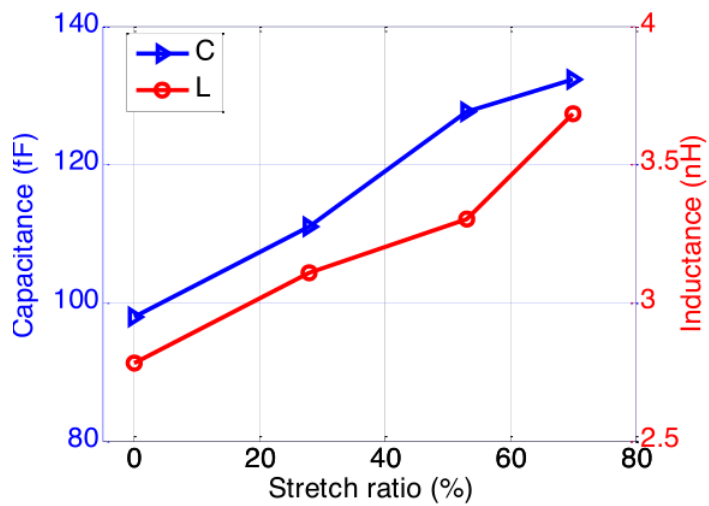
(b)

Figure 4.5   The capacitance and inductance with different stretch ratios. (a) Stretching
along the perpendicular gap direction. (b) Stretching along the gap direction.

From Figure 4.5, it is observed that as the unit cell being stretched in two perpendicular
directions, the equivalent capacitance and inductance will increase as the stretch percent-
age increases. The increment of two components will lead to the decrement of resonant
frequency, and the incremental trend of the perpendicular stretching case is more obvious

than the case stretching along the gap. This difference can be caused by the smaller gap when stretching in the perpendicular direction, which makes the delta-gap source more effective.

Experiment-wise, the major contributor of net capacitance for a SRR is the gap capacitance C_{gap} which depends on the gap geometry . On the other hand the net inductance consists with self-inductance of the conducting loop and the mutual inductance induced by the boundary conditions of waveguide that imposed on the SRR for certain orientations (quasi-periodic structure). The self-inductance of an un-stretched circular loop and a stretched elliptical loop are both geometrically dependent. The mutual inductance not only depends on the self-inductance but also relies on the SRR orientations with different mirror effect imposed by the waveguide. Undoubtedly, the geometry change by simply stretching will have great impact on both net capacitance and inductance, thus shift the resonance frequency.

In the first measurement arrangement (Figure 4.3(a)), the SRR was stretched along the H-field direction with different stretch ratios. The external electric field was formed across the gap to excite the electric resonance that corresponded to a transmission dip at the resonance frequency in the transmittance spectrum.

Figure 4.6 shows that by stretching the SRR, the resonance was progressively tuned to the lower frequencies. Specifically, for the stretch ratio of 17%, 28%, 53%, and 72%, the resonance frequency red shifted from 10.54 GHz to 9.78 GHz, 9.05 GHz, 8.52 GHz, and 7.67 GHz, respectively. This configuration is corresponding to the stretching case shown in Figure 4.5, both L and C are increased caused by the stretching, which resulted in a red shift in resonance frequency.

We conducted the finite element method analysis (FEA) with the COMSOL Multiphysics simulator, where different strains were applied to the two sides of the sample (Figure 4.6). The simulated structural deformation of the ring agrees well with the experimental result, and shows that as the ring was stretched, the geometry of the SRR was changed

dramatically and the liquid metal inside the SRR was compressed with the elastomer and remained connected. The deformation profiles under different stretches were modeled in finite integration solver based electromagnetic simulation tool CST Studio. The SRR was made of liquid metal with conductivity of 3.46×10^7 and was encapsulated in ecoflex cell. The dielectric constant and loss tangent of ecoflex silicone rubber we used in this study were 2.5, and 0.01 respectively. The cell was placed on a wood substrate with dielectric constant of 1.22 and loss tangent of 0.1. The simulation was conducted in a waveguide with four aluminum walls. All the simulation conditions exactly mimic the real measurement setup in order to get a better consistence. The simulated transmittance profiles were presented with dot line along with the experimental results in Figure 4.6.

In the second measurement arrangement (Figures 4.3(c) and 4.7), the resonance was excited by both the electric and magnetic field. Experimentally, at different stretch levels of 17%, 28%, 53%, and 72%, the resonance frequency was observed to red shift from 10.21 GHz to 9.58 GHz, 9.37 GHz, 8.58 GHz, and 7.37 GHz, respectively. The CST simulated result is presented with dot line in Figure 4.7 as well. For this case, the stretching direction is the same as the previous case, and the trend of shifting resonance frequency agrees with simulated L and C shifting trend shown in Figure 4.5(a) according to Equation 4.1.

In the third measurement configuration (Figures 4.3(d) and 4.8), the resonance was induced by the circulating current in the ring caused by the magnetic field. The testing results show that at the stretch of 17%, 28%, 53%, and 72%, the resonance frequency shifted from 9.58 GHz to 9.24 GHz, 8.79 GHz, 8.32 GHz, and 7.32 GHz, respectively and the decrement of resonance frequency was observed as expected according to our simulation shown in Figure 4.5(b). When the device is stretched in this direction, both L and C components will increase as the stretch ratio increase which will result in a decrease of resonance frequency
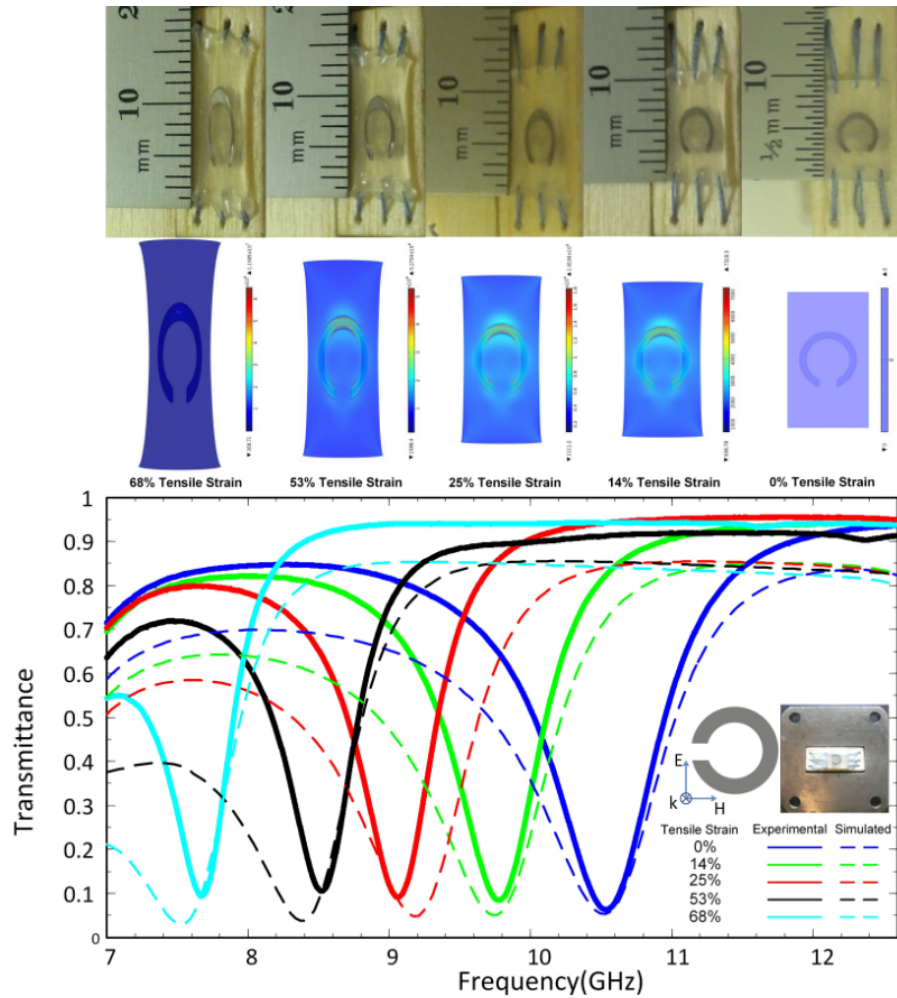
Figure 4.6   The measured and simulated transmittance spectra of the tunable liquid metal
SRR meta-atom at different stretching ratios of 0, 17%, 28%, 53%, and 72%,
when the meta-atom was placed inside the waveguide as shown in the inset.
Also, refer to Figure 4.3(a) for the measurement arrangement. The correspond-
ing experimental (upper) and simulated (down) results for the stretch-induced
deformations of the tunable meta-atom are also included.
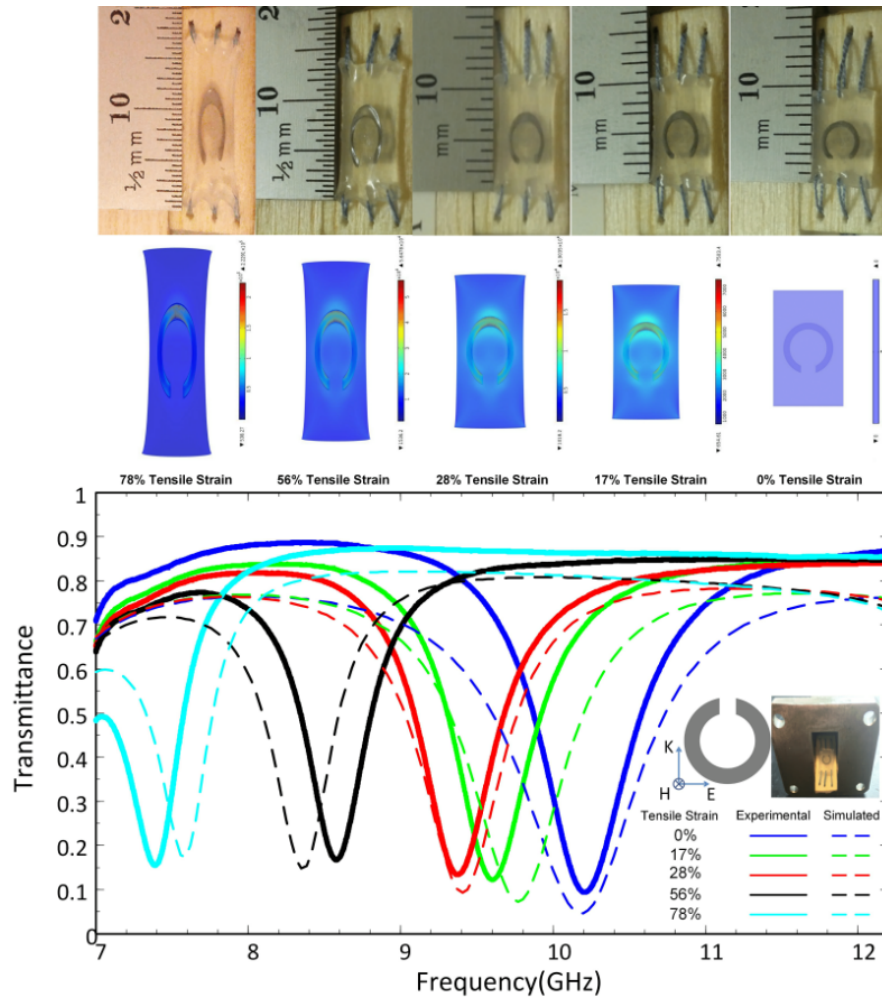
Figure 4.7   The measured and simulated transmittance spectra of the tunable liquid metal SRR meta-atom at the different stretch levels or stretching ratios of 0, 17%, 28%, 53%, and 72%, when the meta-atom was placed inside the waveguide as shown in the inset. Also, refer to Figure 4.3(c) for the measurement arrangement. The corresponding experimental (upper) and simulated (lower panel) results for the stretch-induced deformations of the tunable meta-atom are also included.
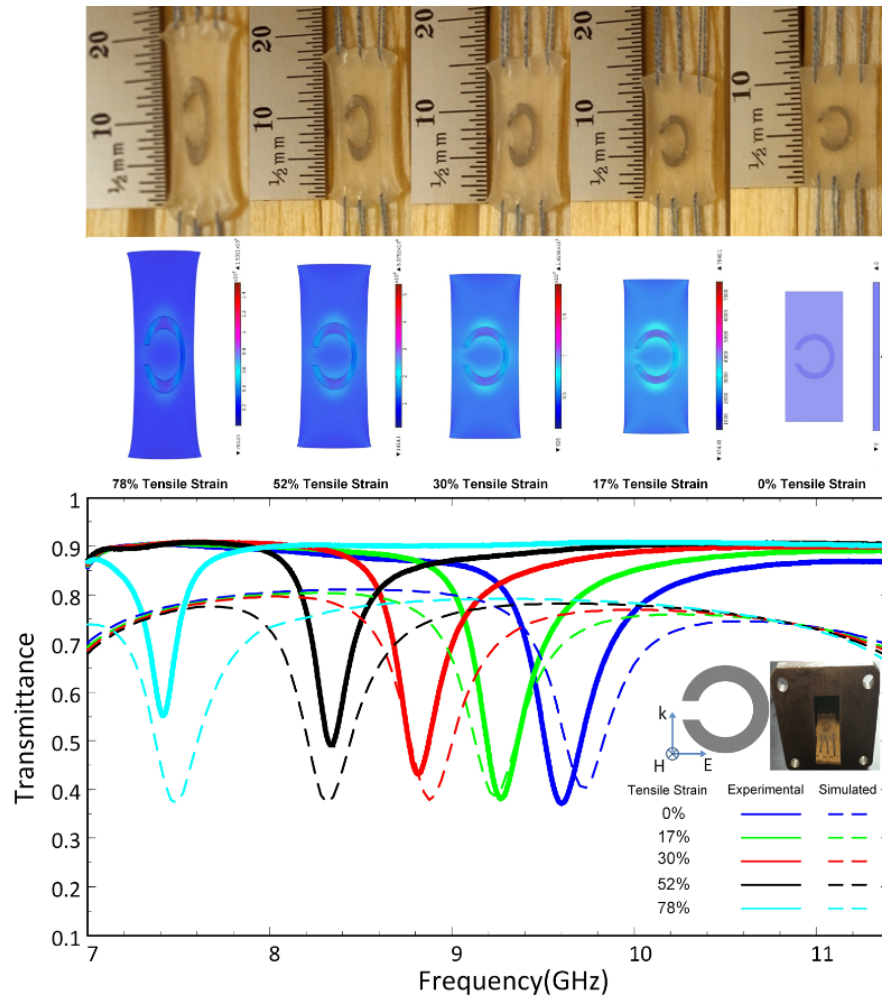
Figure 4.8   The measured and simulated transmittance spectra of the tunable liquid metal SRR meta-atom at the different stretching ratios of 0, 17%, 28%, 53%, and 72%, when the meta-atom was placed inside the waveguide as shown in the inset. Also, refer to Figure 4.3(b) for the measurement arrangement. The corresponding experimental (upper) and simulated (lower panel) results for the stretch-induced deformations of the tunable meta-atom are also included.

For all of these three cases, stretching increased the length edge in the gap region and the fringing effect as well. In addition, more charge will be distributed near the gap region. So the stretching directly increased the facing area of liquid metal by decreasing the front

arm distance near the gap, which enhances the SRR's ability in storing charge in the near gap region, namely this stretching increased the equivalent capacitor.

For all three of the aforementioned measurement configurations, the testing results showed fairly good agreement with the HFSS LC extraction result and CST Studio simulation results. The slight discrepancy between the simulated and testing results may be attributed to the inaccurate geometrical parameters of the SRR extracted from the images of the deformed SRR (Figures 4.6, 4.7, and 4.8) and then applied to the CST Studio simulations. Nevertheless, as demonstrated, when the same stretch of 72% was applied to the SRR in all the three measurement configurations, the resonance frequency of the SRR could be tuned by an absolute shift of 2.87 GHz (Figure 4.6), 2.83 GHz (Figure 4.7), and 2.26 GHz (Figure 4.8), or a relative shift of 27.2%, 27.8%, and 23.5%, with respect to the original resonance frequency of 10.54 GHz, 10.20 GHz, and 9.58 GHz, respectively. Figure 4.9 summarizes the relationships between the stretch ratio and the resulting resonance frequency shift.

The present meta-atom exhibited good repeatability in the resonance modulation, responding to multiple (> 500) cyclic tests. We note that further elongation of the SRR beyond 72% would move the resonance frequency to below the lower cutoff frequency of the waveguide used in this study. Even with the applied moderate stretch amplitude, this tunable meta-atom method could provide a considerable frequency tuning range covering 71.75% (2.87 GHz divided by 4.0 GHz) of the whole X-band frequency range (8.0-12.0 GHz). Furthermore, by changing its overall size and geometrical parameters of the SRR, the original resonance frequency of the SRR can be set to be at the upper limit of the X-band frequency range. By doing that, tuning in the whole X-band frequency range may be achieved with sufficient stretching. Our experiments showed that the present SRR could be stretched by more than twice ($> 200\%$) the original size in any directions, while keeping the embedded liquid metal structure continuous, flexible, and recoverable, without breaking of the encasing polymer layer or occurring of structural hysteresis.
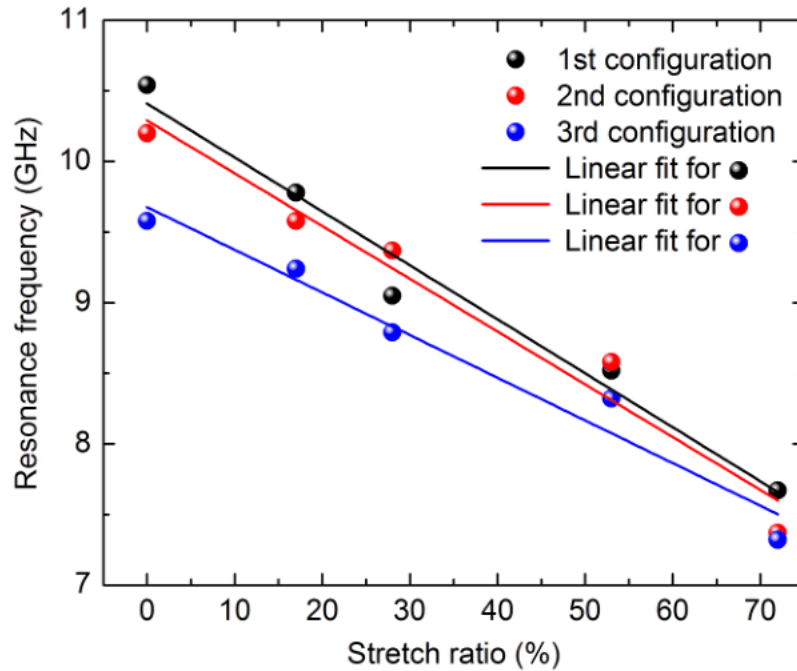
Figure 4.9   The resonance frequency as a function of the stretch ratio for the tunable meta-atom in the three measurement configurations shown in Figures 4.6-4.8

4.4   Conclusions

A liquid metal SRR-based tunable meta-atom was demonstrated in the X-band frequency range. The meta-atom consisted of a liquid metal resonator encased by a flexible elastomer skin. By stretching the meta-atom, the resonance frequency of the meta-atom was tuned continuously over more than 70% of the whole X-band frequency range. The meta-atom in this study presents a simple but effective building block for realizing mechanically tunable metamaterials. Also, since the constituent materials of the present meta-atom are relatively ecofriendly, reusable and durable, the metamaterials made of such meta-atoms potential will find many applications in wearable EM coatings and devices.

CHAPTER 5. FROM META-ATOM TO META-SKIN: A WEARABLE MICROWAVE DEVICE WITH CLOAKING EFFECTS AND TUNABLE FREQUENCY SELECTIVE PROPERTY

In this chapter we extend the previous work of single meta-atom to meta-skin. This meta-skin is composed of an array of liquid metallic split ring resonators (SRRs) that embedded in a stretchable elastomer. By arranging the meta-atoms into a 2-Dimensional (2D), the difficulties of single meta-atom to demonstrate its application in practice is improved. Based on its feature of flexible and stretchable, we demonstrated two potential applications. One is tunable frequency selective surface, and the other is "cloaking" effect in suppressing the scattering field from an object.

The material for this chapter is based on co-paper published in Scientific Report [113] with Co-author Peng Liu [112].

5.1 Meta-skin Desgin and Electromagnetic Simulation

Figure 5.1(a) shows the schematic of the meta-skin, which is composed of 225 identical SRR meta-atoms. These meta-atoms are arranged in a 15×15 2-dimensional (2D) with the lattice constant of $p = 7.5$ mm. For the dimensions of the the SRR in the meta-atom are illustrated in Figure 5.1(a), where the inner radius $a = 2.0$ mm, the outer radius $b = 2.5$ mm, the thickness $h = 0.5$ mm, and the gap $g = 1.0$ mm. Based on the dimension of single SRR, this meta-skin is designed to work in X-Band regime. The SRRs in the 2D array are made of liquid metal (EGaIn) and encased by a silicone elastomer (Ecoflex). The thickness of the Ecoflex is $d = 1.45$ mm. EM simulations were conducted to estimate the resonance frequency of the array by using ANSYS High Frequency Structure Simulator (HFSS). As shown in Figure 5.1(a), the SRR array is placed in the $x - y$ plane, and the magnetic

field ($\mathbf{H}$) is parallel to the z direction and penetrates the SRRs, thus induced the magnetic resonance. With the aforementioned geometrical parameters for the SRR, the resonance frequency for the meta-skin device is around 9.84GHz. The surface current distribution at the resonance frequency is demonstrated in Figure 5.1(a). By stretching the meta-skin (As shown in Figure 5.1(b)), the lattice constant, the shape of the SRRs, and the mutual interaction between the SRRs will be modulated. Accordingly, the resonance frequency of the meta-skins will be shifted [111].

The fabrication process for the meta-skin is exactly same as the one for the single meta-atom, which has been presented in detail in 4.2 from Chapter 4. Thus, it will not be repeated here.
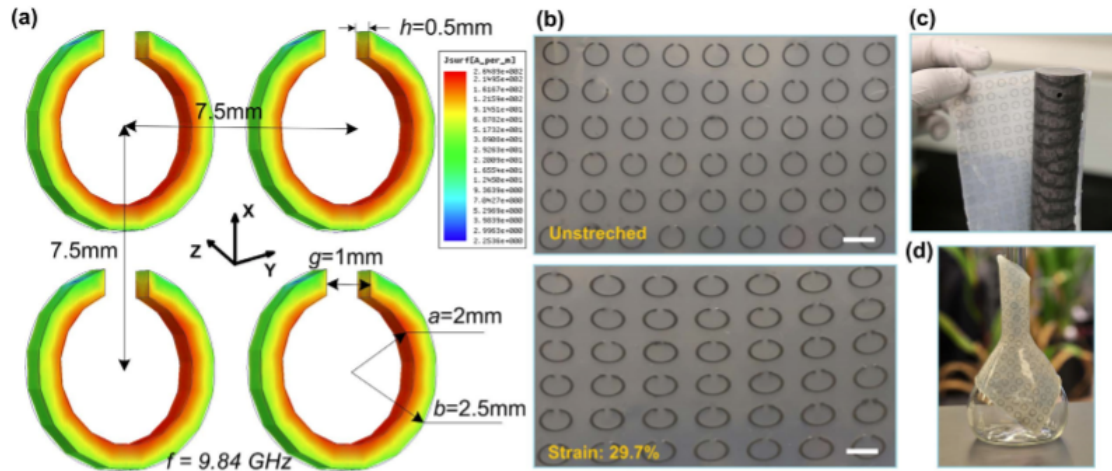
Figure 5.1   (a) Geometry and simulated surface current distribution of the meta-skin. (b) Photos of the unstretched and stretched meta-skin. Scale bars represent 5 mm. (c) A photo of a 30.48 cm long, 3.175 cm diameter dielectric nylon rod wrapped by the meta-skin. (d) Flexibility demonstration with a glass flask wearing the meta-skin.

5.2   Tunable Frequency Selective Characteristic

EM measurements were conducted in free space. A programmable vector network analyzer (VNA, Agilent E8364) was used to measure the spectral responses from sample. To generate a quasi-plane wave illumination, the meta-skins were placed between two horn antennas (one as a transmitter and the other as a receiver) within the far field regions.

5.2.1   Measurement and Results

Due to the highly stretchable feature of the meta-skin, the dimensions of the SRRs can be altered through stretching along different directions. Our previous research showed that the stretch-induced dimensional changes of the SRR can influence the equivalent inductance and capacitance of the SRR, thus shifting its resonance frequency [111].

To exam the true performance of the multi-layer meta-skin, 6 pieces of meta-skin were fabricated to construct a testing device. The schematic for the device is shown in Figure 5.2(a), and the real device is shown in Figure 5.3(a). These 6 pieces of meta-skin were aligned in the direction perpendicular to the surface of meta-skin, with initial space of $d = 3$ mm between two neighboring pieces. The whole multi-layer meta-skin device are placed between two horn antennas (one antenna as receiver and the other as transmitter) in their far-field regions to achieve a quasi-plane wave interaction. In order to excite the magnetic resonance, the meta-skin are placed in the **E**-plane of the antenna, so that the **H** can be coupled to magnetic resonance from the current loop in SRR. This experimental setups are illustrated in Figure 5.2(a).

In this experiment, as the multilayers of the meta-skins were stretched along the wave propagation (k) direction with the stretch ratio of 0%, 15.9%, 29.7%, 36.4%, and 50%. Accordingly, the strong resonances of the meta-skins were observed at 9.84 GHz, 9.76 GHz, 9.47 GHz, 9.27 GHz, and 9.15 GHz, respectively. The measurement results are shown in Figure 5.2(b) with dashed lines.

Since the vertical space d between two neighboring layers also affect the resonance distribution in the spectra, two more supplementary experiments are carried out. The space between two neighboring layers were defined by inserting fixed size foam, which has relative permittivity close to one. Figures 5.2(c), (d) show the spectral responses of the meta-skins to different stretching levels for the spacing of $d1 = 13$ mm and $d2 = 17$ mm, respectively.

As the meta-skins moved farther away from each other, the mutual inductance between the resonators in the neighboring layers is reduced. Consequently, an increase in resonance frequency of the meta-skins is expected. Indeed, for the unstretched sample, the resonance frequency was shifted from 9.84 GHz to 11.9 GHz as the vertical spacing increased from 3 mm to 13 mm. As we further increased d to 17 mm, the resonance frequency was shifted to 12.4 GHz. Similarly, by stretching the multilayer metal-skins along their surfaces in the horizontal direction, the resonance frequency was also observed to move towards lower frequencies. Therefore, by varying the spacing between the meta-skins in the vertical direction and stretching the metal-skins in a planar direction, the resonance frequency tuning range of the meta-skins can be largely broadened.

To verify the reliability of experimental results, an HFSS-based full wave EM simulation was carried out. In order to obtain the authentic deformation of SRR with different stretch ratios, COMSOL Multiphysics was employed to simulate the deformation, and then the structural information was imported into HFSS for the EM simulation, by applying the periodical boundary condition for the SRR unit cell. The simulation results with different stretch ratios are illustrated in Figure. 5.2(b) with solid lines. The simulated results and the experimental results achieved a good agreement in the trend of shifting resonance frequency with different stretch ratios. The minor differences of the dip positions and the bandwidth can be attributed to some possible aspects, such as the real loss from the meta-skin device, accuracy of the real deformation mode, human operation, and temperature change from the laboratory environment.
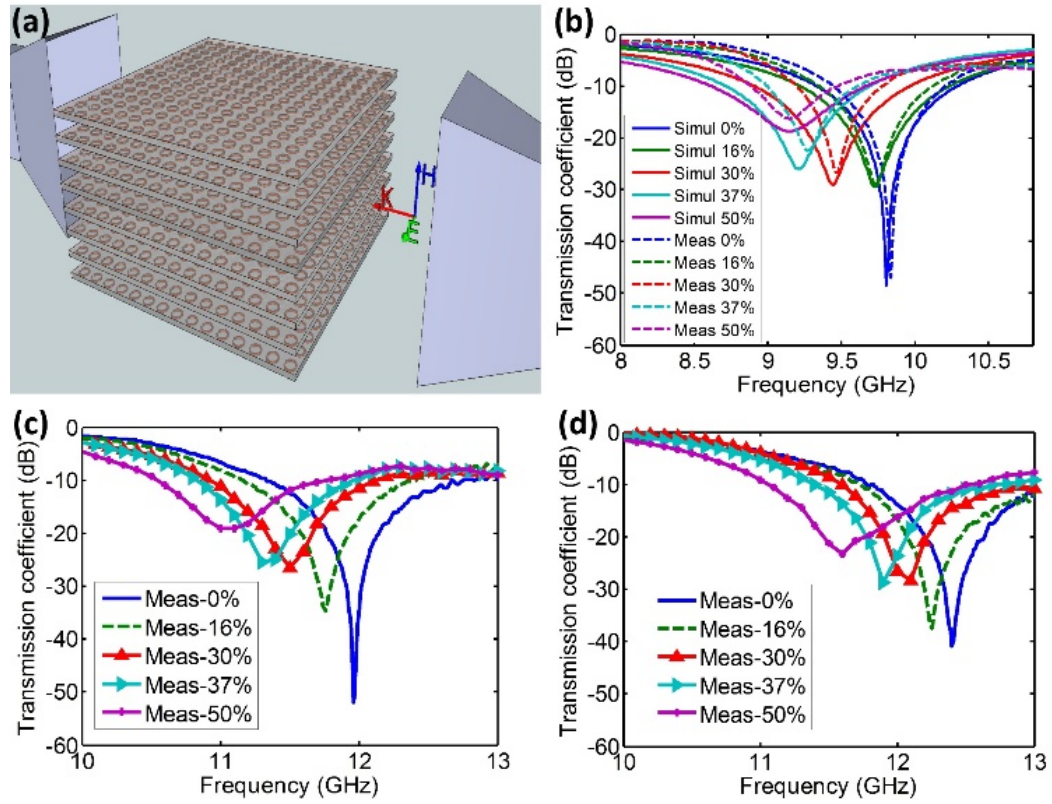
Figure 5.2   (a) Schematic of the multilayer meta-skins and measurement setup.   (b) Simulated and experimental transmittance spectra of the tunable multilayer meta-skins (vertical spacing between neighboring layers: $d = 3$ mm) at different stretching ratios. (c,d) Experimental transmittance spectra for $d = 13$ mm (c) and $d = 17$ mm (d). The conductivity for the liquid metal is 3.47×10^6 S/m. The dielectric constant and loss tangent of Ecoflex are 2.5 and 0.01, respectively.
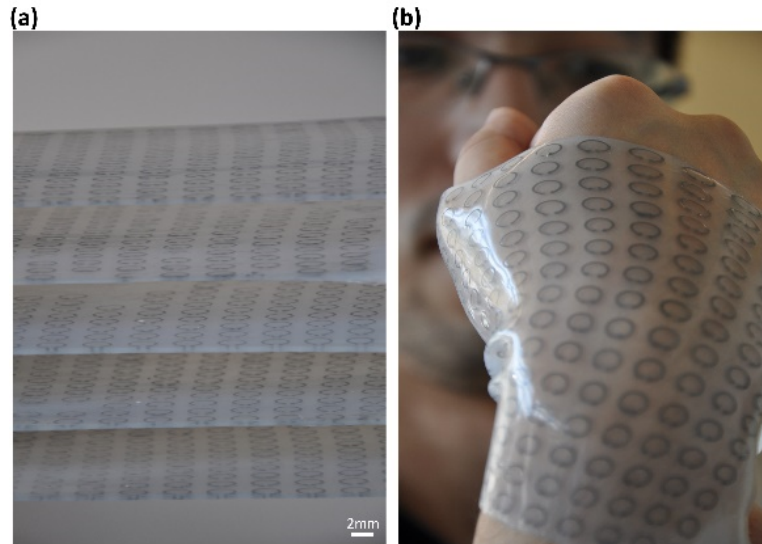
Figure 5.3   (a) Photo of multilayer meta-skins. Each layer consists of an array of liquid metal based SRRs embedded in a highly stretchable elastomer. (b) Flexibility demonstration by wrapping a wrist with a single layer meta-skin.

5.3   Cloaking Effects

The fully flexible nature of the meta-skin makes it possible to wrap on an object with arbitrary shapes (Figure 5.3(b)). To investigate the EM property of the meta-skin coated on the arbitrary shape object, we used a single layer of meta-skin to wrap on a 30 cm long, 3 cm diameter dielectric nylon rod with dielectric constant of 3.8, which is shown in Figure 5.4(b)). We investigated how this wrapping material could influence the scattered field from the rod. The far-field measurement was thus conducted to measure scattering strength from a bare nylon rod, a nylon rod wrapped by a pure Ecoflex sheet, and a nylon rod wrapped by the meta-skin.

In the measurement setup (Figure 5.4(a)), the sample hangs from a cotton thread at to minimize unwanted scattering signals from the support constructs. The two horn antennas are placed at an equal distance of $L = 80$cm from the sample. This ensures that the object

is in the far-field region (according to the far-field condition $2D^2/\lambda$, where $D = 9.8$ cm is the diagonal of the horn antenna and $\lambda = 3$ cm is estimated from the center operating frequency). The transmitter antenna is fixed at $\theta = 0$ during the measurement, while the receiver antenna is moved around the sample with a fixed distance to receive scattering signals from different angles θ. The two horn antennas are inserted into the absorbing material to minimize the scattering from the background. The aforementioned VNA is used to measure scattering parameters from the object. The objective azimuthal bi-static measurements were conducted to obtain the s-parameter for further data analysis.

5.3.1 Device Setup and Measurement
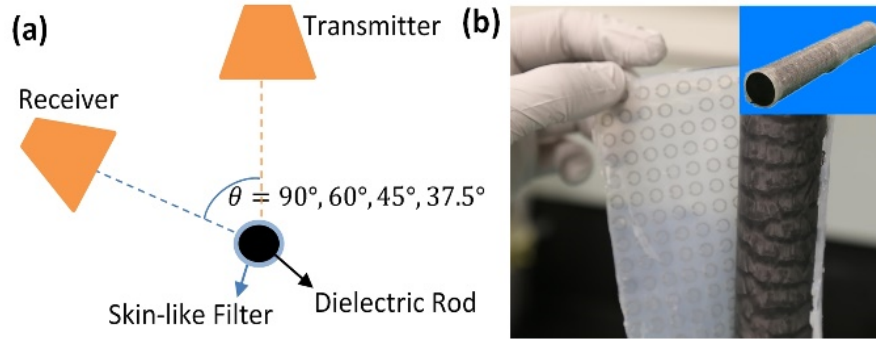
Figure 5.4   (a) Schematic for measurement of cloaking profile. (b) A photo of a dielectric nylon rod wrapped by the meta-skin. The dielectric constant of the rod is 3.8. The diameter and the length of the rod are 3 cm and 25 cm respectively.

5.3.2 Data Processing and Analysis

The way to obtain the scattered field was by subtracting the incidence field (S_{21i}) from the total field (S_{21t}). In this manner, not only the scattering field from the sample can be derived theoretically, but also clutters from background can be minimized in some extend. To realize this, two consecutive measurements were conducted. First, the sample was placed at the designated position and S_{21t} was measured. Then, the sample was removed and S_{21i}

was recorded. Correspondingly, the raw s-parameter of the scattered field can be expressed as

$$S_{21o} = S_{21t} - S_{21i} \tag{5.1a}$$

$$S_{21}(\omega_k) \triangleq S_{21o} \tag{5.1b}$$

where ω_k represents the sampling frequency. This method can be applied to obtain the scattering field from the uncoated rod, poly-coated rod, and SRR-coated rod. Limited by the laboratory environment, this set of measurements were not operated in the anechoic chamber. The non-anechoic environment made the objective signal mixed with background clutter. Although scattering field derived from subtraction can avoid some clutter scattering from the background, it is still hard to entirely remove the clutters due to the complicated environment, and time variant human operations.

The spectra responses of $S_{21}(\omega_k)$ are shown through Figure 5.5(a) with blue solid line. Obviously, the raw data contain many complex stray signal. In order to obtain the target signal without these clutters efficiently and accurately, discrete Fourier transform (DFT) is employed for the post processing.
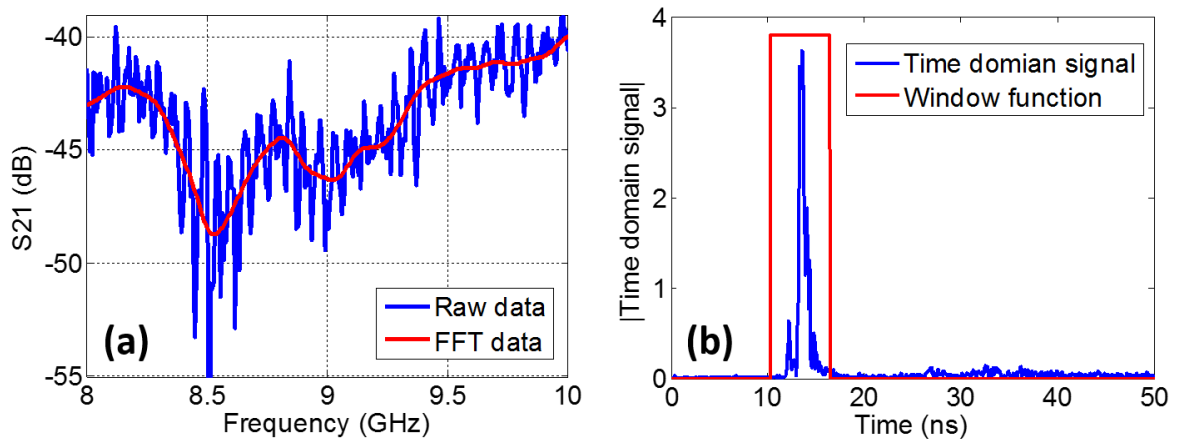
Figure 5.5   (a) Raw data and processed data. (b) The gate function in time domain.

Instead of directly implementing the DFT on $S_{21}(\omega_k)$, a Gaussian window function ($G(\omega_k)$) is multiplied with $S_{21}(\omega_k)$ to select the target signal, due to its better resolution in the time domain. A new signal in frequency domain was generated, denoted as $H(\omega_k)$. To clearly reveal the signal responses in the time domain, an inverse DFT (IDFT) is implemented over $H(\omega_k)$ and generates $h(t_n)$, where t_n represents discrete sampling point in time domain. This IDFT can reveal the signal response in the time domain. As shown in Figure 5.5(b) with solid blue line, the signals from clutters were late arrived compared with signal from the sample object. To remove the interaction with background from $h(t_n)$, a designated rectangular window function ($w(t_n)$) is employed to remove those early or late arrived signals as shown in Figure 5.6(b) with red solid line. Finally, the DFT was implemented over this processed time domain signal ($w(t_n)h(t_n)$), and yielding $S'(\omega_k)G(\omega_k)$, where $S'(\omega_k)$ solely represents the interaction with the sample in the frequency domain. This entire process can be expressed as

$$H(\omega_k) = G(\omega_k) \cdot S(\omega_k) \tag{5.2}$$

$$h(t_n) = \frac{1}{N} \sum_{k=0}^{N-1} H(\omega_k)e^{-j\omega_k t_n} \tag{5.3}$$

$$S'(\omega_k) = \frac{\sum_{k=0}^{N-1} w(t_n)h(t_n)e^{j\omega_k t_n}}{G(\omega_k)} \tag{5.4}$$

where N is number of sampling points. By using Equations 5.2, 5.3, and 5.4, we obtained the scattering field for the aforementioned three different samples. An example with the observation angle of $105°$ is shown in Figure 5.6, where the red solid lines, as shown in Figure 5.6(a)-(c), represent the processed scattering field for different samples. Compared to $S(\omega_k)$, $S'(\omega_k)$ becomes smooth after the removal of the clutters from $S(\omega_k)$.

The post-processed scattering gains for the meta-skin covered, the polymer covered, and the uncovered rods are presented in Figure 5.7(a)-(e). The results show that the scattering gain from the meta-skin covered rod is significantly reduced in the frequency band from 8-10 GHz at five different measurement angles $\theta = 37.5°, 45°, 60°, 90°$, and $105°$. Specifically, compared with the uncovered case, at $\theta = 37.5°$ the meta-skin was able to

suppress the scattering gain in over 33% of frequency band between 8-10 GHz. At other angles the suppression effect of the meta-skin is more significant and the scattering grain was suppressed in over 70% of the same frequency range. The largest suppression of 20 dB was found at around 9 GHz at $\theta = 37.5°$. The overall scattering suppression effect of the meta-skin is illustrated by averaging the scattering gain with different angles (Figure 5.7(f)). It is observed that the meta-skin was able to suppress the scattering gain by about 75% in the band of 8-10 GHz. The scattering suppression is mainly attributed to the cloaking effect of the embedded SRRs around the designed frequency, where the destructive interference between the resonance of the SRRs and the scattering from the dielectric rod occurred. We also noted that the scattering gain spectra of the meta-skin wrap in Figure 5.7 do not have the exactly same resonance frequency as the transmittance spectra of the multilayer meta-skins under the unstretched state in Figure 5.2(b). The factors below may be attributed to this observation: first, the scattering suppression gain was measured at different angles, which actually is angle-dependent due to different phases of multiple reflections and interactions over the interfaces; second, only one layer of the meta-skin was coated on the surface of the nylon rod with the dielectric constant of 3.8, while multiple layers of the meta-skins were used in the frequency selective surface application and spaced by foam with the dielectric constant of close to one.

The whole meta-skin remained fully functional without fatigue or cracking after repeated measurements. This is because the liquid metal SRRs can flow and reshape responding to applied strains. Besides the single circular SRR, many other magnetic resonance structures may be used in the meta-skin setting to realize frequency selection and scattering suppression. Furthermore, in addition to the magnetic resonators, liquid metal-based electric resonant structures, such as wires, can be integrated into the same elastomer. This will make it possible to achieve negative index for cloaking applications. Moreover, other different stretchable and flexible dielectric host media could be used to embed these liquid metal-based resonant structures. This will provide us with more flexibility to control

loss tangent of the meta-skin. In the microwave frequency regime the dielectric losses are dominant and different substrate dielectric materials can affect the loss tangent. For higher frequencies, such as terahertz, as the ohmic losses become significant, other types of liquid metal or conducting materials are required to form the resonating units.
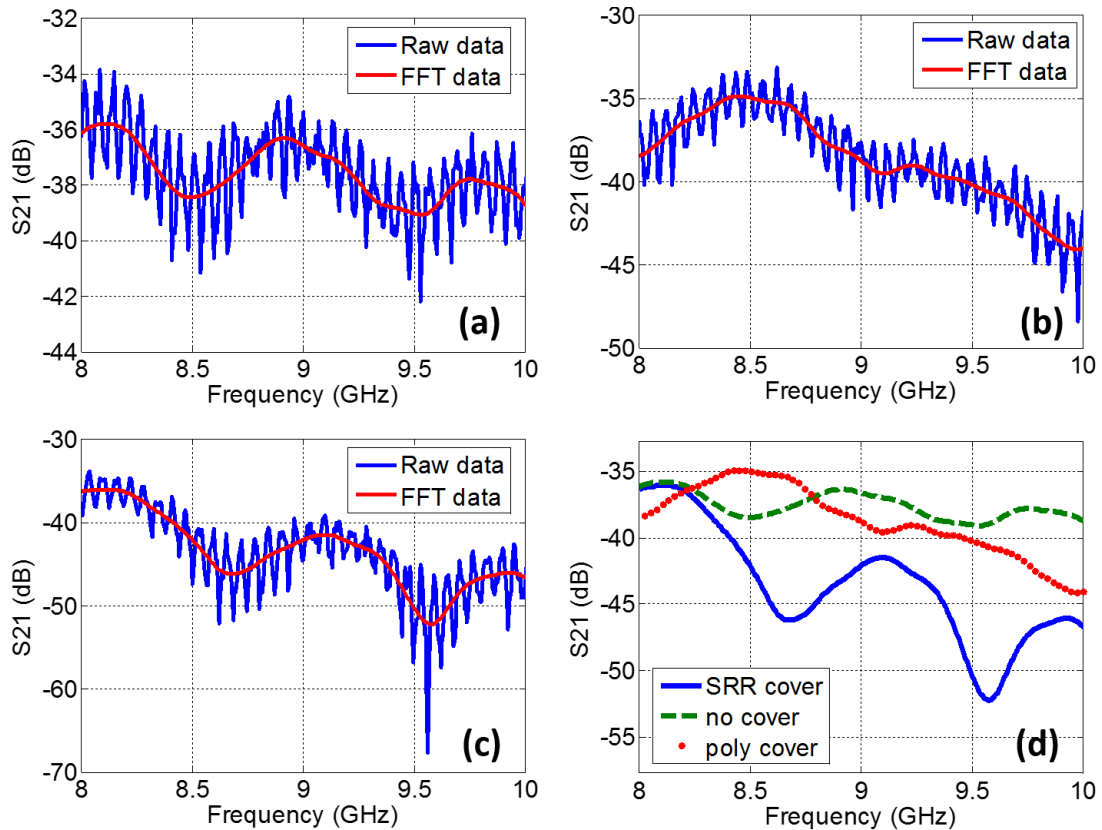
Figure 5.6 (a)-(c) raw data and processed data for uncoated, poly-coated, and SRR-coated cases respectively. The observation angle is $\theta = 105°$. (d) Processed data for three different cases.
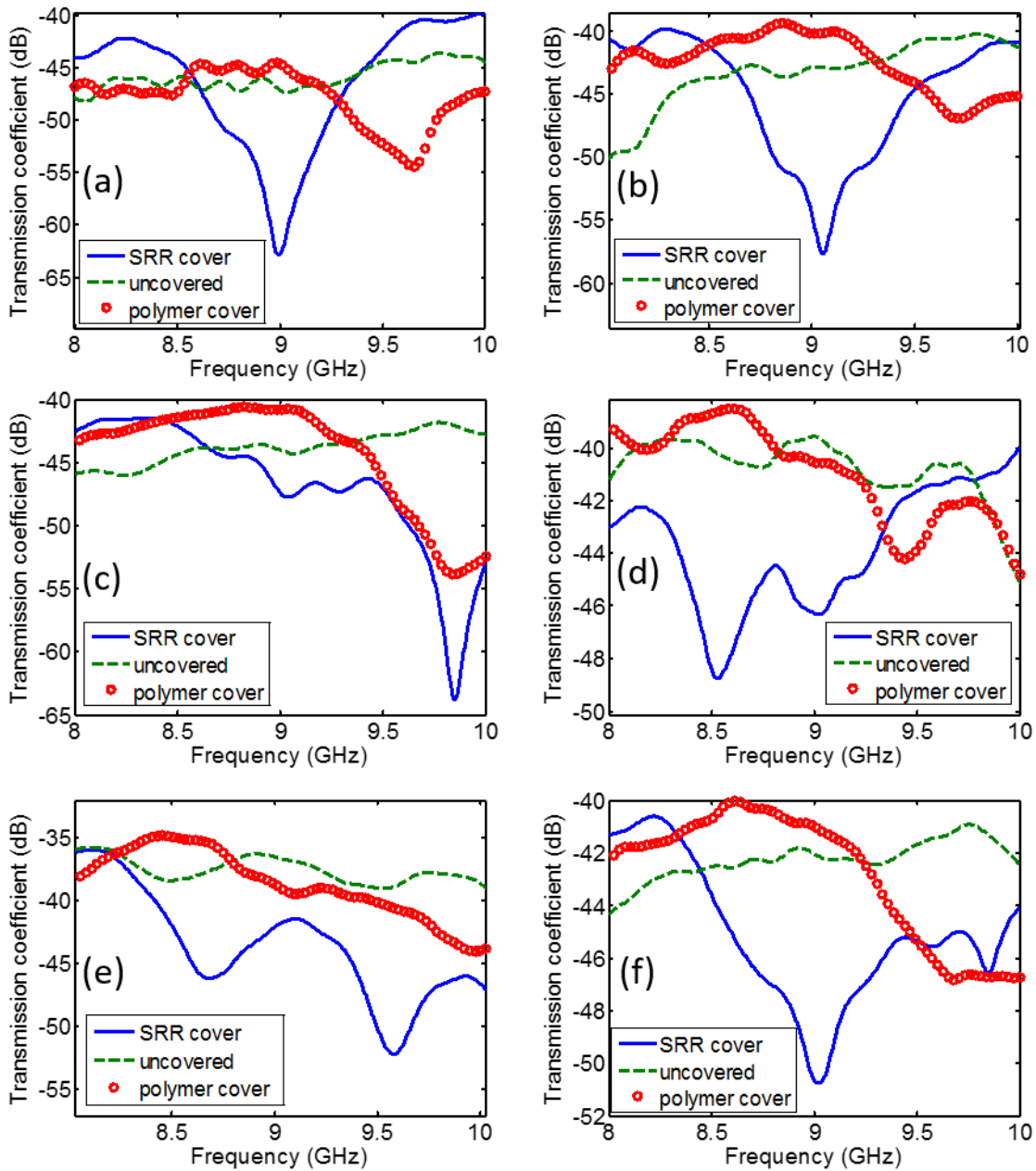
Figure 5.7 Measured scattering gain for the bare dielectric rod (green dash), the rod wrapped with the pure Ecoflex polymer (red circle), and the rod wrapped with the single layer metal-skin (blue solid) at different angles. (a) $\theta = 37.5°$, (b) $\theta = 45°$, (c) $\theta = 60°$, (d) $\theta = 90°$, and (e) $\theta = 105°$. (f) The average scattering gain over different angles.

5.4   Conclusions

A stretchable and wearable microwave meta-skin was developed by embedding an array of liquid metal SRRs into a highly stretchable elastomer. We demonstrated the strong ability of the meta-skin to tune the resonance of the frequency selective surface and to suppress the scattering from the curved surface of a dielectric material along different directions. By combining the planar stretching and the vertical spacing, the resonance frequency of the multilayer meta-skins was tuned from 9.15-12.38 GHz. By wrapping a finite-length dielectric rod with the meta-skin, the scattering from the surface of the rod was suppressed by about 75% in 8-10 GHz. It is believed that the present meta-skin technology will find many applications in EM frequency tuning, shielding, and scattering suppression.

CHAPTER 6.   DIRECTIVITY-RECONFIGURABLE WIDEBAND TWO-ARM SPIRAL ANTENNA

In this chapter, we present a novel directivity-reconfigurable wideband antenna in microwave regime. The directivity-reconfigurable feature is realized, again, by virtue of the special property from the liquid metal alloy and highly stretchable elastomer. A two-arm Archimedean spiral antenna is adopted to implement the concept of optimizing directivity by inflating the elastomer to form a dome-shaped antenna. Micro-electro-mechanical systems based microblowers are employed to pneumatically control the shape of the antenna. Due to the wide frequency band property of the spiral antenna, it can be operated from 6.9 GHz to 13.8 GHz. The ability to change the shape of the antenna allows optimizing its radiation pattern by making it become more directive along the main lobe direction or in the inflation direction. Due to the formation of the dome-shaped structure, the radiation pattern of the antenna becomes shaper, thus optimizing its directivity, while its passing band remains wide.

6.1   Design and Fabrication

Figure 6.1(a) shows schematic for a planar self-complementary, two-arm Archimedean spiral antenna made of liquid metal encased by a stretchable silicone elastomer. The operating frequency range of the antenna can be determined by the innermost radius a and the outermost radius b. In order to operate in X-band regime, the antenna is designed to have $a = 3.5$ mm and $b = 18.5$ mm. Each spiral arm has 2.5 turns. The width of the liquid metal is $w = 1.5$ mm and the gap between two arms is $g = 1.5$ mm. The fabricated device before equipped for testing is shown in Figure 6.1(b).

The fabrication process for the antenna is demonstrated in Figure 6.1(c) and was contributed by the collaborator Dr. Peng Liu. For the completeness of the work, the fabrication process will be briefly introduced here, but not in detail. First, a SU-8 photoresist (Microchem, Westborough, MA) is patterned with the designed spirals on a silicon wafer W1. Subsequently, a 700 μm thick silicone layer L1 is formed by casting a prepolymer solution of silicone Ecoflex (Smooth-On, Macungie, PA) on the SU-8 mold, followed by a thermal curing process at 60°C on a hotplate for 30 min. The fully cured L1 layer is then peeled from the SU-8 mold with the spiral channels inside it. To inject the liquid metal alloy EGaIn into the channels, an inlet and an outlet are mechanically punched at the two ends of each channel. Due to the natural poor adhesion between fully cured Ecoflex, a 100 μm thick Ecoflex layer L2 is partially cured on a silanized bare Si wafer W2 at 45°C for 40 sec. After that, the fully cured L1 and the partially cured L2 are immediately transferred to a hotplate at 90°C for 20 min. This allows permanently bonding the two layers. Thus, the spiral channels are formed inside the elastomer. After EGaIn is manually injected into the channels with a metal needle (#20 Gauge) amounted on a syringe (10 mL; Becton-Dickinson, Franklin Lakes, NJ), the residues of liquid metal left around the inlets and outlets are cleaned by a cotton swab dipped with a hydrochloric acid solution (50%, v/v). Lastly, the device is immersed into a thin prepolymer solution of Ecoflex and then is fully cured at 80°C for 30 min to seal the inlets and outlets. The total thickness of the elastomer is approximately 1 mm. The liquid metal is located in nearly half the thickness of the elastomer Figure 6.1(b), (c).
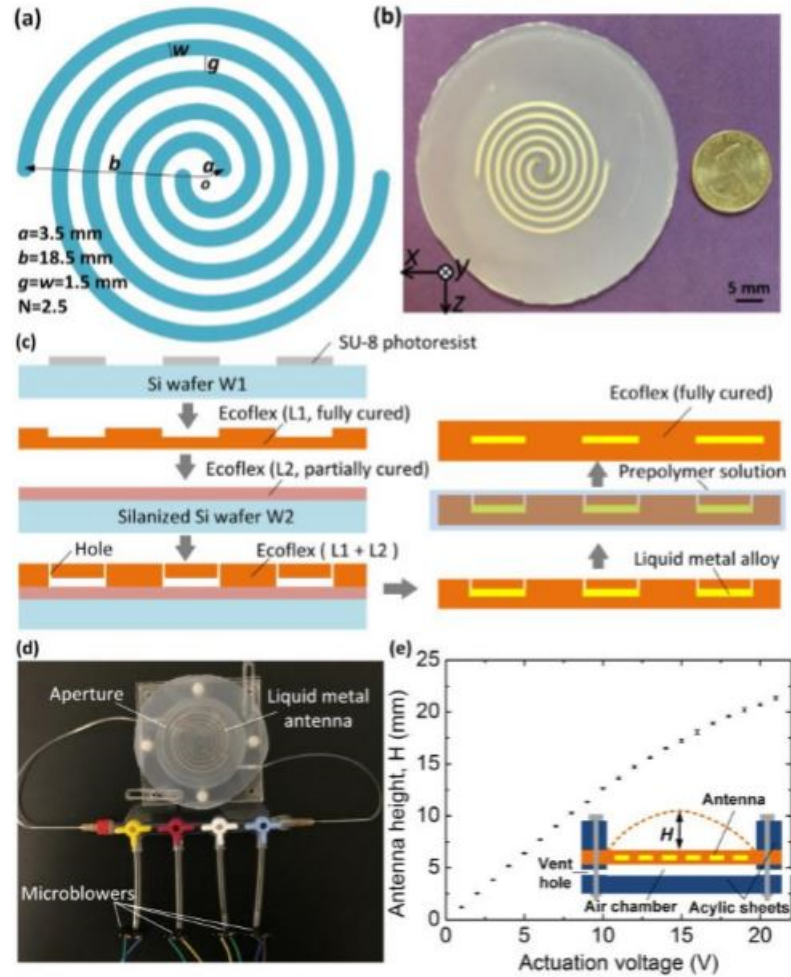
Figure 6.1 (a) Design parameters of the proposed two-arm spiral antenna. (b) Photo of the fabricated planar antenna before assembled to a pneumatic control unit. (c) Schematic of the fabrication process for the planar antenna. (d) Photo of the assembled directivity reconfigurable antenna with a pneumatic air control unit or four voltage-controlled MEMS microblowers. (e) Measured relationship between the inflation height H and the actuation D.C. voltage applied to the microblowers. The error bars represent standard deviations obtained via 100 times repeatability measurements.

In order to deform the liquid metal antenna and control its deformation, an inexpensive and accurate control unit is built with MEMS microblowers (MZB1001E00; Murata, Kyoto, Japan). Briefly, the microblower utilizes a piezoelectric based drive method that features small dimensions and is suitable as a source for high-pressure air generation with compact and low profile. To provide a high pressure to deform the antenna, four microblowers are connected in parallel with tubing and three way hose fittings (Figure 6.1(d)). Subsequently, the planar antenna is sandwiched between two 3 mm thick acrylic boards (Total Plastic, Baltimore, MD) and fixed by four nylon mechanical cap screws. The lower acrylic board is pre-machined to form a 1 mm deep cavity and two lateral air vents. A circular through hole with the diameter of 50 mm is created in the upper cladding board. When a D.C. voltage is applied to the microblowers, the microblowers generate high-speed airflow to pneumatically push the elastomer into a dome-like cap.

6.2   Measurement with Different Configurations

First, the relationship between the applied actuation D.C. voltage to the microblowers and the resulting height H is investigated. As shown in Figure 6.1(e), H increases almost linearly with an applied voltage at low voltage regions (0-10 V) and then increases slightly slowly at high voltage regions (11-21 V). At the maximum allowed voltage of 21 V for the microblowers, the obtained dome height is 21.8 mm. The shape change repeatability of the antenna is investigated by inflating and deflating the antenna for 100 times. The obtained standard deviation of inflation height is less than 1.5%, indicating a good repeatability and reliability of this actuation method. During the repeatability test, the liquid metal inside the spiral channels dynamically responds to the applied pressures by changing its shape and dimensions. No fatigue or cracking is found with the liquid metal or Ecoflex after the repeatability measurements. It takes about 6.5 seconds for the microblowers to inflate the planar antenna from flat to the maximum dome height of 21.8 mm at 21 V. By increasing

the number of the microblowers or exploring other actuation mechanisms, the actuation time of the device can be reduced.
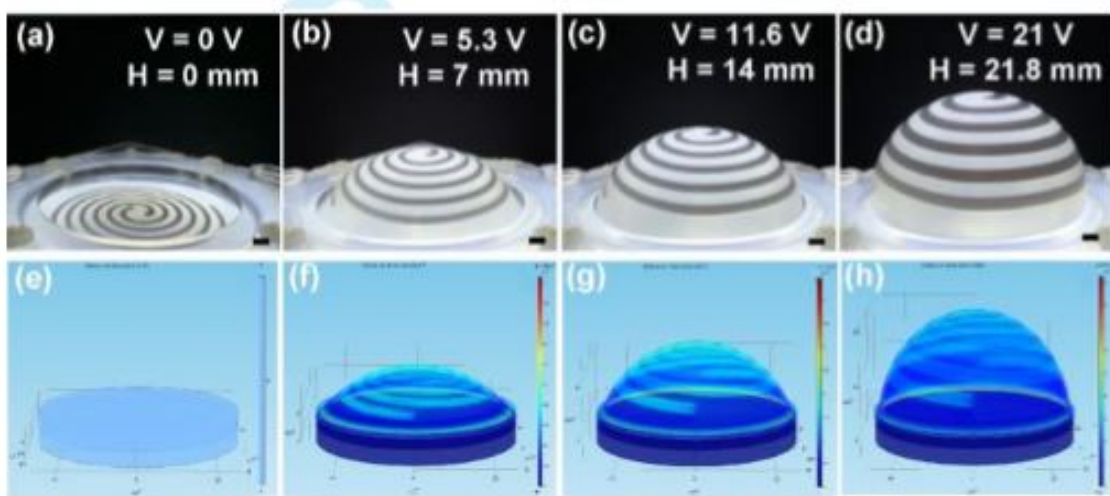
Figure 6.2   Time-lapse images (a-d) and FEA simulation results (e-h) for the Ecoflex elastomer containing the liquid metal antenna with different inflation heights: 0 (a, e), 7 mm (b, f), 14 mm (c, g), and 21.8 mm (d, h). Scale bars in (a-d) represent 3 mm

Figure 6.2 shows the mechanical simulation for four instances of the antenna under different actuation voltages applied to the microblowers. The simulation is performed using finite element analysis (FEA) method based software (COMSOL). The Young's modulus and Poissons ratio of Ecoflex are 29.5 kPa and 0.43, respectively. The pressure values for the simulation are obtained by using a pressure sensor (SPD015AA; Smartec, The Netherlands). As the Ecoflex membrane is inflated, mechanical restoring force of the elastomer acts to balance with the increased internal air pressure, thus obtaining an equilibrium shape at a certain height of the dome. For $H = 0$, 7 mm, 14 mm, and 21 mm under the applied pressure of 0, 2.2 kPa, 5.2 kPa, and 11.8 kPa, the resulting maximum surface stress in the

deformed Ecoflex membrane is found to be 0, 184 kN/m^2, 491 kN/m^2, and 915 kN/m^2, respectively.

As the antenna is made and its deformation is well controlled by the MEMS microblowers, we can start conducting the electromagnetic (EM) measurement. This EM measurement is carried out in an anechoic chamber. The reconfigurable antenna is treated as the receiving antenna, and it is placed on a positioner via a self designed support, which was used for fix the antenna. This positioner is connected to the DAM measurement system (Diamond Engineering, Diamond Springs, CA) . From the PC terminal we can manipulate the DAM system, and further control the positioner to drive the antenna to rotate in both θ, and φ directions.

To receive signal properly, the antenna is fed by a 3 mm SMA coaxial connector at the two heads of the spiral arms in the center region. The central pin and the ground pin of the connector are directly in contact with the liquid metal by inserting the two pins into the channels. A drop of Ecoflex precursor solution is added and then polymerized to seal the holes formed during the insertion Figure 6.3. Then a coaxial cable was used to connected the antenna to one port of the programmable vector network analyzer (VNA, Agilent E8364).

On the other hand, a horn antenna, which is working at X-band, is connected to another port of VNA, and it is treated as the transmitting antenna. These two antennas were placed with a distance of 1.2 m, which ensured that the receiving antenna was in the far-field region (according to the far-field condition $2D^2/\lambda$, where $D = 9.8$ cm is the diagonal of the horn antenna, and $\lambda = 3$ cm is estimated from the center operating frequency).

The received RF signal will be sent back to the VNA and the power (for every position of the receiving antenna) is measured there. All the measured data are sent to the PC terminal, where DAM software will provide instantaneously visualization and post-processing functions. The schematic for the measuring system is shown in Figure 6.4.
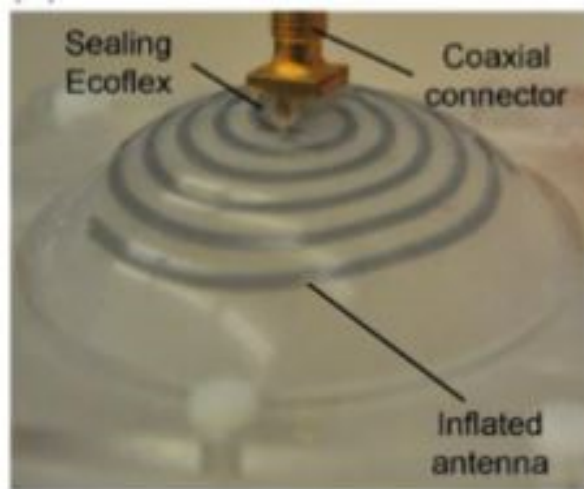
Figure 6.3   Photo of the liquid metal antenna with a feeding structure.
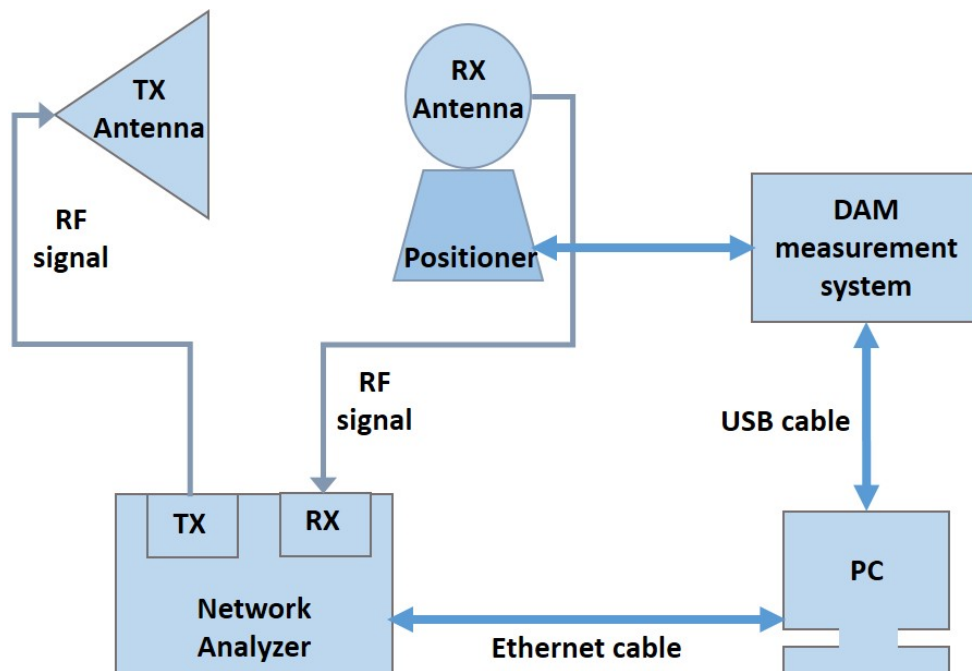
Figure 6.4   The setup for the antenna measurement system, where TX in the figure represents transmitting and RX represents receiving antennas

The reflection coefficients as a function of frequency for different dome heights are measured and plotted in Figure 6.5. The result shows that as the antenna is inflated, the passing band for the antenna remains in a wide frequency range from 6.9 GHz to 13.2 GHz with S_{11} lower than -10 dB.
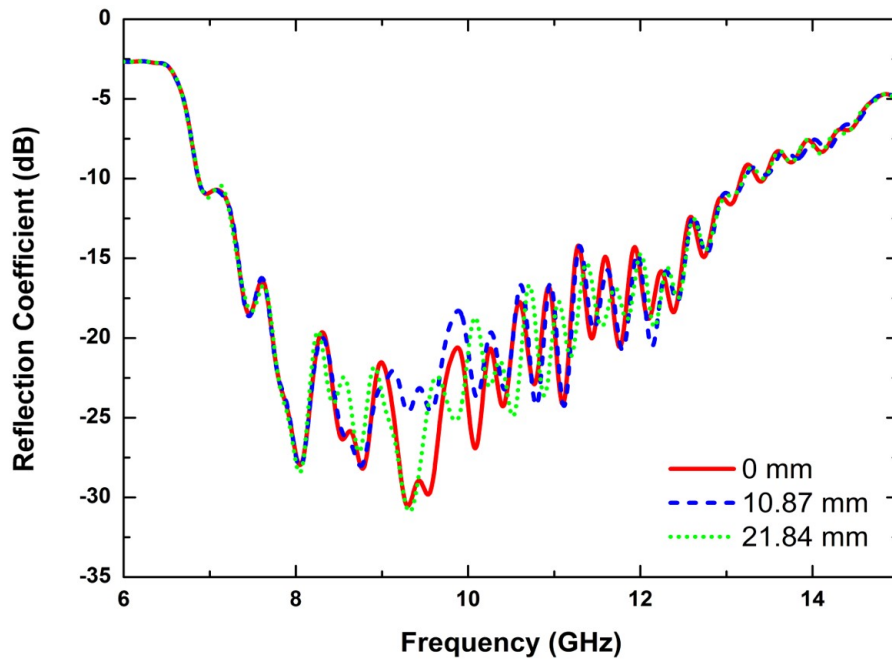
Figure 6.5   Measured reflection coefficient for different inflation heights of the antenna.

The radiation pattern of the designed antenna is measured with a horn antenna in the far field region as shown in Figure 6.6. The designed antenna sits on a turntable rotating around the vertical z axis and the dashed line extending from the horn antenna is in $x - y$ plane. The rotation angle φ is defined as the angle between the horn antenna (dashed line) and x axis. When $\varphi = 90°$, the inflated dome of the antenna point towards the horn antenna. At each sampling angle, 21 measurements are performed to minimize the influence of possible mechanical errors.
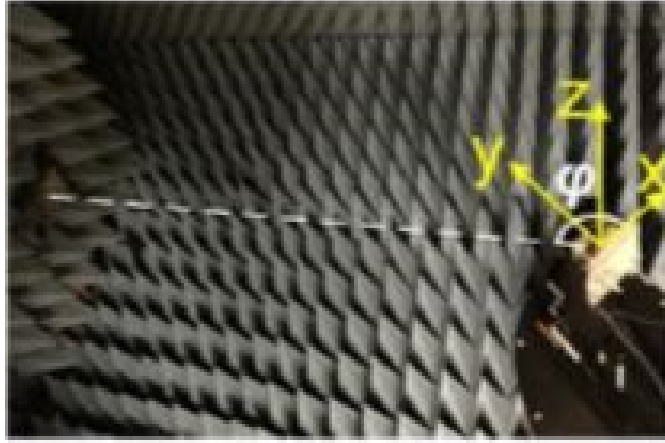
Figure 6.6   Measurement setup for measuring the radiation pattern of the liquid metal antenna with horizontal polarization.

Figure 6.7 shows the radiation patterns of the antenna with horizontal polarization at 8.5 GHz for three different inflation heights: 0, 10.9 mm, and 21.8 mm. The result indicates that the signal strength exhibits the strongest along the y axis (here, y direction at 90° and $-y$ direction at 270°). The flat liquid metal antenna transmits almost same signal strength for both y and $-y$ directions, because of the geometrical symmetry at $x - z$ plane along y axis. As the inflation height increases, the liquid metal antenna tends to increase the radiation along y direction (90°), while decreasing the radiation along $-y$ direction (270°). Further increasing the inflation height will further enhance the radiation along y direction. Therefore, the directivity at the main lobe direction (y direction) can be optimized by inflating the antenna to higher heights.

The radiation patterns of the antenna at different frequencies are also measured in the frequency range from 7.6 GHz to 9.8 GHz with the reflection power lower than -20 dB. Figures 6.8-6.11 show the normalized radiation patterns of the designed antenna with three inflation heights (0, 10.9 mm and 21.8 mm) at two sampling frequencies (8.5 GHz and 9.5 GHz). By rotating the receiving horn antenna by 90°, the radiation patterns of vertical polarization are also measured.
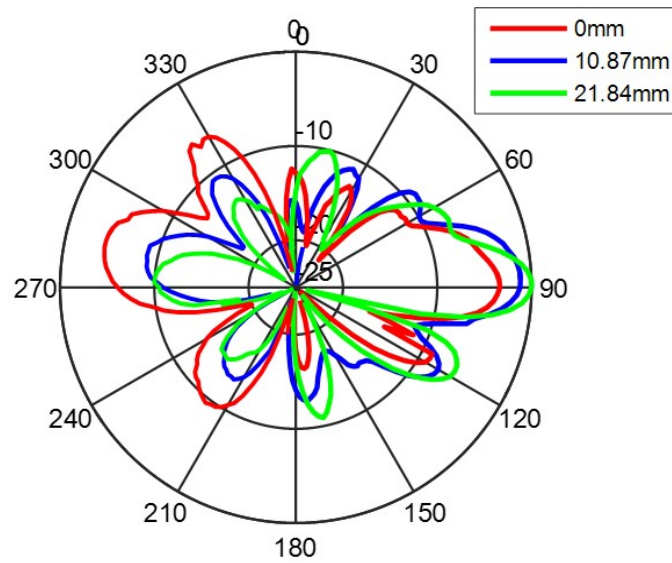
Figure 6.7   Measured radiation pattern at 8.5 GHz of horizontal polarization for three inflation heights.
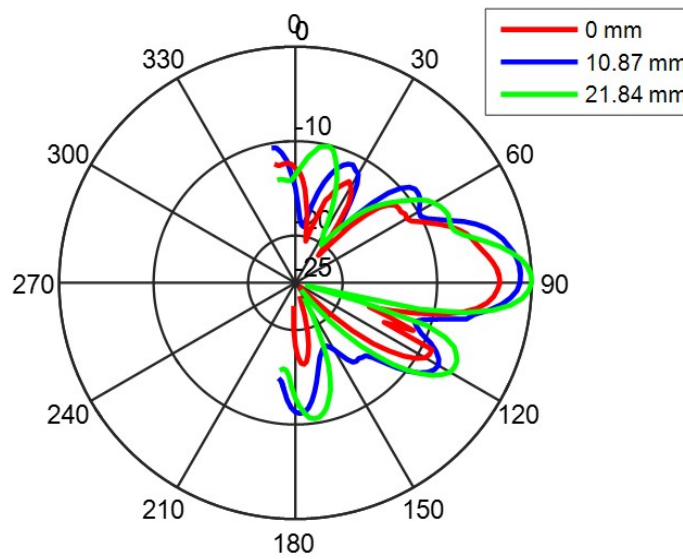
Figure 6.8   Measured radiation pattern at 8.5 GHz of horizontal polarization for three inflation heights from 0° to 180°.
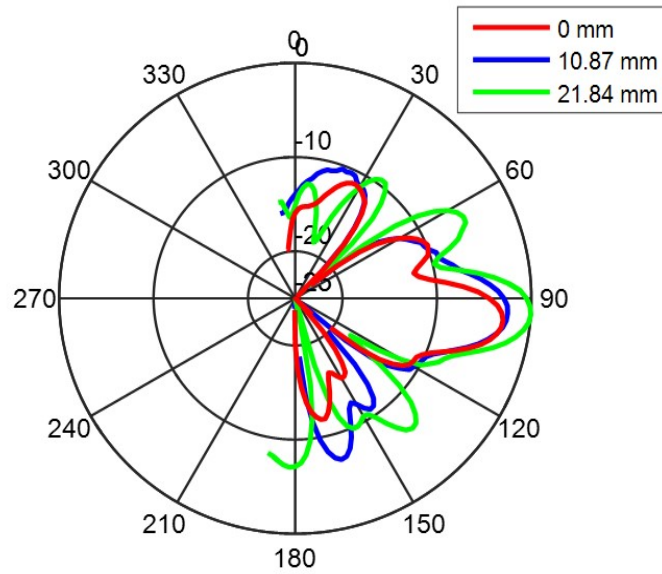
Figure 6.9   Measured radiation pattern at 8.5 GHz of vertical polarization for three infla-
tion heights from 0° to 180°.
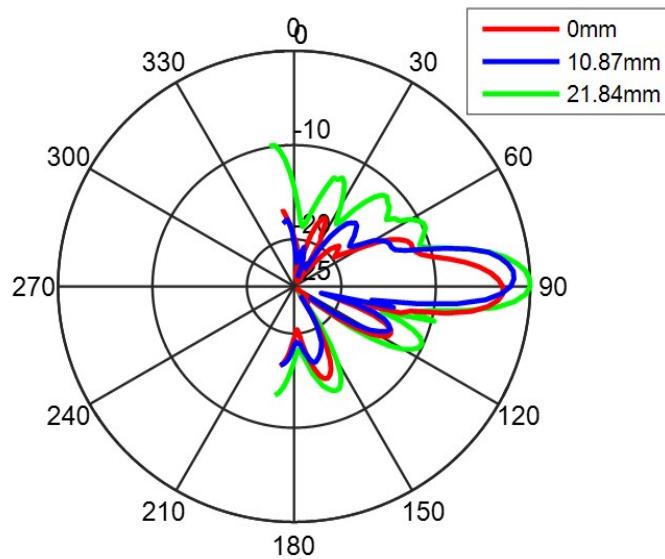
Figure 6.10   Measured radiation pattern at 9.5 GHz of horizontal polarization for three
inflation heights from 0° to 180°.
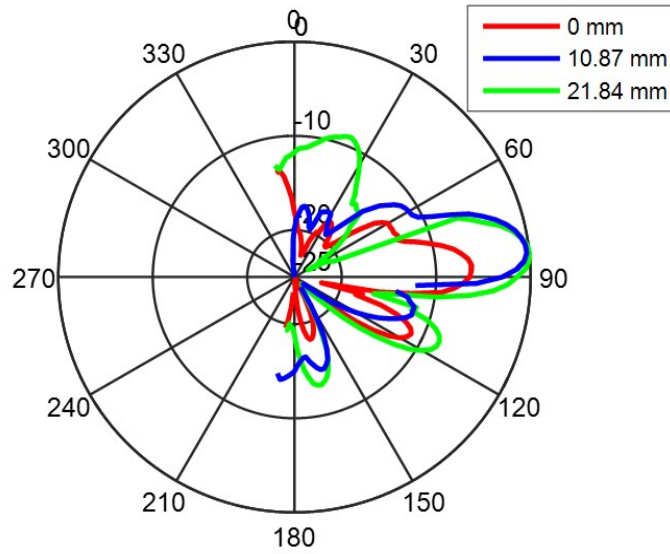
Figure 6.11   Measured radiation pattern at 9.5 GHz of vertical polarization for three infla-
tion heights from 0° to 180°.

6.3   Analysis and Discussions

As mentioned above, the directivity of the antenna can be improved only in the inflation direction of the dome. Consequently, the radiation patterns of the antenna are measured only from 0° to 180° along the main lobe direction or the inflation direction (90° in the radiation pattern plots). The measured radiation patterns show good directivity for all the measured heights at 8.5 GHz and 9.5 GHz. With the measured radiation pattern, we can evaluate the directivity of this antenna beginning from its definition [114]

$$D(\theta, \varphi) = \frac{U(\theta, \varphi)}{U_{ave}} \tag{6.1}$$

In Equation (6.1) $U(\theta, \varphi)$ is the radiation intensity. It can be written as $U(\theta, \varphi) = U_m |F(\theta, \varphi)|^2$, where U_m is the maximum radiation intensity in direction $(\theta_{max}, \varphi_{max})$, and $F(\theta, \varphi) = |\mathbf{E}(\theta, \varphi)|/\max|\mathbf{E}|$ is the radiation pattern. U_{ave} is defined as

$$U_{ave} = \frac{\iint U(\theta, \varphi) d\Omega}{4\pi} \tag{6.2}$$

and $d\Omega = \sin\theta d\theta d\varphi$. Further the directivity can be written as

$$D(\theta, \varphi) = \frac{4\pi U(\theta, \varphi)}{\iint U(\theta, \varphi) d\Omega} \tag{6.3}$$

and the radiation pattern is

$$F(\theta, \varphi) = \frac{\sqrt{|E_\theta(\theta, \varphi)|^2 + |E_\varphi(\theta, \varphi)|^2}}{E_0} \tag{6.4}$$

Thus, the maximum directivity is

$$D_0 = \frac{4\pi U_m}{\iint U(\theta, \varphi) d\Omega} = \frac{4\pi}{\iint |F(\theta, \varphi)|^2 d\Omega} \tag{6.5}$$

The field radiation pattern shown in Equation (6.4) is the same as measured S_{21}. By assuming $F(\theta, \varphi)$ is axisymmetric we have

$$D_0 = \frac{2}{\int_0^\pi |F(\theta)|^2 \sin\theta d\theta} \tag{6.6}$$

The directivity of the antenna at different frequencies and heights are shown in Table 6.1 Correspondingly, the efficiency of the antenna can be evaluated by using

$$\varepsilon_r = \frac{G_r}{D_0} \tag{6.7}$$

where G_r is the gain of the designed antenna, this quantity can be derived by using the Friis transmission formula [114]

$$P_r = P_t \left(1 - |S_{11}|^2\right) \left(1 - |S_{22}|^2\right) \frac{G_t G_r \lambda^2}{(4\pi R)^2} \tag{6.8}$$

where P_r and P_t are receiving and transmitting power, $G_t = 25$ dB is the gain of the horn antenna, $R = 1$ m is the distance between two antennas, power ratio $P_r/P_t = |S_{21\theta}|^2 + |S_{21\varphi}|^2$, and

$$\varepsilon_r = \frac{(4\pi R)^2 P_r}{G_t P_t D_0 \lambda^2 \left(1 - |S_{11}|^2\right) \left(1 - |S_{22}|^2\right)} \tag{6.9}$$

Table 6.1   directivity and efficiency

	Frequency	Dome Height		
		0 mm	10.9 mm	21.8 mm
Directivity	8.5 GHz	5.39 dB	7.24 dB	7.74 dB
	9.5 GHz	7.75 dB	8.92 dB	9.90 dB
Efficiency	8.5 GHz	54.2%	46.4%	72%
	9.5 GHz	40%	45.1%	60.5%

D_0 can be evaluated from Equation 6.6, and the efficiency with different antenna heights are demonstrated in Table 6.1. The efficiency of the antenna varies between 40% and 72% for different inflation heights and frequencies.

More importantly, with increasing the inflation height, the antenna exhibits stronger directivity along its main lobe direction, thus optimizing its directivity along the inflation direction. Specifically, at 8.5 GHz, by inflating the antenna from 0 to 10.9 mm and further to 21.8 mm, the signal strength is improved by 2 dB and further to 3 dB in the horizontal polarization direction, and by 1 dB and further to 3 dB in the vertical polarization direction. Similarly, at 9.5 GHz, the signal strength in the inflation direction is also enhanced by 3 dB and 6 dB, for the horizontal and vertical polarization, respectively. It should be pointed out that as the radiation pattern shows a good similarity between the vertical and horizontal polarizations, the antenna provides relatively good circular polarization. This can be confirmed from the value of axial ratio, which is defined as the ratio between the major and minor axis of the elliptical polarization (for circular polarization axial ratio equal to one). By using the radiation patterns of two orthogonal polarizations, we can calculate the axial ratios at different frequencies and inflation heights, which are shown in Table 6.2.

Table 6.2   Axial ratio for different inflation heights and frequencies

	0 mm	10.9 mm	21.8 mm
8.5 GHz	1.25	1.54	1.32
9.5 GHz	1.58	1.10	1.08

Furthermore, benefiting from the deformability of the liquid metal and elastomer, the present antenna is able to preserve its electromagnetic properties after being inflated for 500 times to the maximum height of 21.8 mm. Theoretically, the directivity of the device can be further enhanced by adding a back reflector or cavity. However, it is difficult to maintain the gap distance unchanged between the antenna and the reflector during the mechanical deformation of the antenna. We will optimize the device and introduce a cavity to the design in the future. Nevertheless, the demonstrated reconfigurability of the present device allows for continuous tuning the radiation pattern and directivity of the antenna. Lastly, to obtain the full benefit of structural tuning, the device needs to operate at temperatures that keep the infused liquid metal in a liquid state. EGaIn used in this study has a melting point of $\sim 15.5°$ C, making it liquid at room temperature. It should be pointed out that when lower operation temperatures are needed, the device requires using other liquid metals or alloys with lower melting points.

6.4   Conclusions

A liquid metal based antenna with a wide frequency band has been developed and its capability to optimize directivity has been demonstrated. The antenna is formed by encasing EGaIn into Ecoflex elastomer and can withstand a large deformation with a good reliability and repeatability. This allows inflating the antenna containing elastomer to form a dome-like structure with different heights, by pneumatically pumping high-pressure air into an air cavity using MEMS microblowers. By increasing the inflation height, the signal strength of the antenna can be improved to different extents. The antenna retains its wideband character without being affected by the pneumatic inflation. With an improved directivity in a broad operating frequency range, the antenna can radiate more energy towards the receiver. It is believed that the antenna can find its applications where targeted wireless power transfer, high directivity, circular polarization, and wide operating frequency band are needed.

CHAPTER 7.   CONCLUSION

In this thesis we mainly investigate two topics. The first one is guided and leaky modes for the dielectric rod and the second one is tunable metamaterials and applications.

In the first part of this thesis, we start our investigation from the field distribution outside the dielectric rod and define the modes to be solved. Through the analysis of different special functions and Riemann sheets, the relationships of these mode solutions are concluded. Further, the complete forms of characteristic equations to solve proper and two types of improper modes are presented explicitly.

In the process of solving these non-linear equations with iterative methods, we provide relatively accurate initial guesses to accelerate the convergence in finding the mode solutions. By asymptotically expanding the special functions and employing the Lambert W function, a set of initial guess expressions are derived. Around cutoff frequency, Lambert W functions at different branches are employed to find the initial guesses for the proper modes, outgoing improper modes, and incoming improper modes stopping at the cutoff frequency. At the low frequency limit, we predict the whole set of outgoing improper modes and incoming improper modes stopping at DC. Also, the initial guesses for the whole set of proper and incoming improper modes from the high frequency limit are also derived. Further, we have made the initial guesses applicable for both TM and TE cases by carefully testing different values of κ. Finally, the complex transverse propagation constants of proper and two types of improper modes are demonstrated numerically.

The procedure in solving modes for the DPS rod is further applied to solve the DNG rod by using the same mode definitions.The characteristic equation for the DNG case is first derived and then the initial guesses for different modes around the cutoff frequency, high frequency limit and low frequency limit are expressed by expanding the characteristic

equations. Finally, these initial guesses are used to solve the characteristic equations with an iterative method and the numerical results are illustrated.

In the second part of the thesis, we introduce the conventional metamaterials and pointe out its drawback of fixed and limited bandwidth. Correspondingly we present a new type of tunable meta-atom in the X-band frequency range toward reconfigurable metamaterials.

This SRR-based meta-atom is made of all flexible materials compliant to the surface of an interaction object. It uses a liquid metal-based SRR as its core constituent embedded in a highly flexible elastomer. We demonstrate that simple mechanical stretching of the meta-atom can lead to the great flexibility in re-configuring its resonance frequency continuously over more than 70% of the X-band frequency range.

Then, we extend the idea of meta-atom to meta-skin, which is developed by embedding an array of liquid metal SRRs into a highly stretchable elastomer. We demonstrate the strong ability of the meta-skin in tuning the resonance frequency as frequency selective surface and to suppress the scattering from the curved surface of a dielectric material along different directions as a flexible "cloaking" surface.

In the last part of the thesis, utilizing the flexible and stretchable properties of liquid metal and elastomer, we develope a novel directivity-reconfigurable two-arm spiral antenna which can be operated from 6.9 GHz to 13.8 GHz. A two-arm Archimedean spiral antenna is adopted to implement the concept of optimizing directivity by inflating the elastomer to form a dome-shaped antenna. The ability to change the shape of the antenna via the Micro-electro-mechanical systems allows optimizing its radiation pattern by making it more directive in the inflation direction, while its frequency band remains wide.

BIBLIOGRAPHY

[1] W. M. Elsasser, "Attenuation in a dielectric circular rod," *J. Appl. Phys.*, vol. 20, pp. 1193-1196, Dec. 1949.

[2] D. Jablonski, "Attenuation characteristics of circular dielectric waveguide at millimeter wavelengths," *IEEE Trans. Microw. Theory Techn.*, vol. 26, no. 9, pp. 667-671, Sep. 1978.

[3] D. Jablonski, "Power-handling capabilities of circular dielectric waveguide at millimeter wave wavelengths," *IEEE Trans. Microw. Theory Techn.*, vol. 33, no. 2, pp. 85-89, Feb. 1985.

[4] K. C. Kao, "Dielectric-fiber surface waveguide for optical frequencies," *Proc. IEE*, vol. 133, no. 7, pp. 1151-1158, Jul. 1966.

[5] E. Snitzer, "Cylindrical dielectric waveguide modes," *J. Opt. Soc. Am.*, vol. 51, no. 5, pp. 491-498, May 1961.

[6] A. Safaai-Jazi and G. L. Yip, "Classification of hybrid modes in cylindrical dielectric optical waveguides," *Radio Sci.*, vol. 12, no. 4, pp. 604-609, Aug. 1977.

[7] R. Chatterjee, *Dielectric and Dielectric-Loaded Antennas*, John Wiley & Sons, Inc., 1985, ch. 2.

[8] F. J. Zucker and H. Jasik, Ed., "Surface and leaky-wave antennas," in Antenna Engineering Handbook. New York: McGraw-Hill, 1961, ch. 16.

[9] A. A. Oliner, "Types and basic properties of leaky modes in microwave and millimeterwave integrated circuits," *IEICE Trans. Electron.*, vol. 83, no. 5, pp. 675-686, May 2000.

[10] S. Kobayashi, R. Mittra, and R. Lampe, "Dielectric tapered rod antennas for millimeter-wave applications," *IEEE Trans. Antennas Propag.*, vol. 30, no. 1, pp. 54-58, 1982.

[11] J. Arnbak, "Leaky waves on a dielectric rod," *Electron. Lett.*, vo1. 5, no. 3, pp. 41-42, Feb. 1969.

[12] R. Sammut and A. W. Snyder, "Leaky modes on circular optical waveguides," *Appl. Opt.*, vol. 15, no. 2, pp. 477-482, Feb. 1976.

[13] K. Y. Kim, *Guided and Leaky Modes of Circular Open Electromagnetic Waveguide*, PhD thesis, Kyungpook National University, Daegu, Korea, Dec. 2004.

[14] K. Y. Kim, H.-S. Tae, and J.-H. Lee, "Analysis of leaky modes in circular dielectric rod waveguides," *Electron. Lett.*, vol 39, no. 1, pp. 61-62, Jan. 2003.

[15] P. Lampariello, F. Frezza, H. Shigesawa, M. Tsuji, and A. A. Oliner, "A versatile leakywave antenna based on stub-loaded rectangular waveguide: Part I-Theory," *IEEE Trans. Microw. Theory Techn.*, vol. 46, no. 7, pp. 1032-1041, Jul. 1998.

[16] C. D. Nallo, F. Frezza, A. Galli, P. Lampariello, and A. A. Oliner, "Properties of NRDguide and H-guide higher-order modes: Physical and nonphysical ranges," *IEEE Trans. Microw. Theory Techn.*, vol. 42, no. 12, pp. 2429-2434, Dec. 1994.

[17] X.-Y. Zeng, S.-J. Xu, K. Wu, and K.-M. Luk, "Properties of guided modes on open structures near the cutoff region using a new version of complex effective dielectric constant," *IEEE Trans. Microw. Theory Techn.*, vol. 50, no. 5, pp. 1417-1424, May 2002.

[18] P. Lampariello, F. Frezza, and A. A. Oliner, "The transition region between bound-wave and leaky-wave ranges for a partially dielectric-loaded open guiding structure," *IEEE Trans. Microw. Theory Techn.*, vol. 38, no. 12, pp. 1831-1836, Dec. 1990.

[19] J. Zhu and Y. Lu, "Leaky modes of slab waveguides-asymptotic solutions," *J. Lightwave Techno.*, vol. 24, no. 3, pp. 1619-1623, 2006.

[20] H. Rogier and D. Vande Ginst, "A fast procedure to accurately determine leaky modes in multilayered planar dielectric substrates," *IEEE Trans. Microw. Theory Techn.*, vol. 56, no. 6, pp. 1413-1422, Jun. 2008.

[21] H. Rogier and D. De Zutter, "Berenger and leaky modes in optical fibers terminated with a perfectly matched layer," *J. Lightwave Techo.*, vol. 20, no. 7, pp. 1141-1148, Jul. 2002.

[22] D. Vande Ginste, H. Rogier, and D. De Zutter, "Efficient computation of TM- and TE-polarized leaky modes in multilayered circular waveguides," *J. Lightwave Techo.*, vol. 28, no. 11, pp. 1661-1669, Jun. 2010.

[23] J. Zhu, Z. Shen, and Z. Chen, "Dispersion relations of the modes for open nonhomogeneous waveguides terminated by perfectly matched layers," *J. Opt. Soc. Am. B*, vol. 29, no. 9, pp. 2524-2530, Sep. 2012.

[24] *NIST Handbook of Mathematical Function*, 1st ed., Cambridge University Press., New York., NY, 2010, pp. 217-261.

[25] R. Corless, G. Gonnet, D. Hare, D. Jeffrey, and D. Knuth, "On the Lambert W function," *Adv. Comput. Math.*, vol. 5, pp. 329-359, Dec. 1996.

[26] V. D. Zvorykin, A. O. Levchenko, A. V. Shutov, E. V. Solomina, N. N. Ustinovskii, and I. V. Smetanin, "Long-distance directed transfer of microwaves in tubular sliding-mode plasma waveguides produced by KrF laser in atmospheric air," *Phys. Plasmas* vol. 19, pp. 033509, Mar. 2012.

[27] J.-M. Jin, "Fields and waves in cylindrical coordinates," in *Theory and Computation of Electromagnetic Fields*, New York: John Wiley & Sons, Inc., 2010, ch. 6, pp. 200-230.

[28] C. A. Balanis, "Circular cross-section waveguide and cavities," in *Advanced Engineering Electromagnetics*, 2nd ed., New York: John Wiley & Sons, Inc., 2012, ch.9 , pp. 470-575.

[29] L. Tsang, "Electromagnetic fields of hertzian dipoles in layered media of moderate thickness including the effects of all modes," *IEEE Antennas Wireless Propag. Lett.*, vol. 6, pp. 316-319, Jul. 2007.

[30] W. Shu and J. M. Song, "Wave propagation in grounded dielectric slabs with double negative metamaterials," *Progress In Electromagnetics Research Symposium*, vol. 2, no. 3, pp. 246-250, Mar. 2006.

[31] K. Y. Kim, "Comparative analysis of guided modal properties of double-positive and double-negative metamaterial slab waveguides," *Radioengineering*, vol. 18, no. 2, pp. 117-123, Jun. 2009.

[32] Z. J. Wang and J. F. Dong, "Analysis of guided modes in asymmetric left-handed slab waveguides," *Progress In Electromagnetics Research*, vol. 62, pp. 203-215, Jan. 2006.

[33] C. Li, Q. Sui, and F. Li, "Complex guided wave solutions of grounded dielectric slab made of metamaterials," *Progress In Electromagnetics Research*, vol. 51, pp. 187-195, Jan. 2005.

[34] S. F. Mahmoud and A. J. Viitanen, "Surface wave character on a slab of metamaterial with negative permittivity and permeability," *Progress In Electromagnetics Research*, vol. 51, pp. 127-137, Jan. 2005.

[35] D.-H. Kim, J.-H. Ahn, W. M. Choi, H.-S. Kim, T.-H. Kim, J. Song, Y. Y. Huang, Z. Liu, C. Lu, and J. A. Rogers, "Stretchable and foldable silicon integrated circuits," *Science*, vol. 320, no. 5875, pp. 507-511, Apr. 2008.

[36] D.-H. Kim, Z. Liu, Y.-S. Kim, J. Wu, J. Song, H.-S. Kim, Y. Huang, K.-c. Hwang, Y. Zhang, and J. A. Rogers, "Optimized structural designs for stretchable silicon integrated circuits," *Small*, vol. 5, pp. 2841-2847, Dec. 2009.

[37] J.-H. Ahn, H.-S. Kim, K. J. Lee, S. Jeon, S. J. Kang, Y. Sun, R. G. Nuzzo, and J. A. Rogers, "Heterogeneous three-dimensional electronics by use of printed semiconductor nanomaterials", *Science*, 2006, vol. 314, no. 5806, pp. 1754-1757. Dec. 2006.

[38] Y. Sun and J. A. Rogers, "Inorganic semiconductors for flexible electronics," *Adv. Mater.*, vol. 19, no. 15, pp. 1897-1016, Aug. 2007.

[39] J. Yoon, S. Y. Hong, Y. Lim, S.-J. Lee, G. Zi, and J. S. Ha, "Design and fabrication of novel stretchable device arrays on a deformable polymer substrate with embedded liquid-metal interconnections," *Adv. Mater.*, vol. 26, no. 28, pp. 65806586, Aug. 2014.

[40] M. Kubo, X. Li, C. Kim, M. Hashimoto, B. J. Wiley, D. Ham, and G. M. Whitesides, "Stretchable microfluidic radiofrequency antennas," *Adv. Mater.*, vol. 22, pp. 2247-2749, Jul. 2010.

[41] J.-H. So, J. Thelen, A. Qusba, G. J. Hayes, G. Lazzi, and M. D. Dickey, "Reversibly deformable and mechanically tunable fluidic antennas," *Adv. Funct. Mater.*, vol. 19, no. 22, pp. 3632-3637, Nov. 2009.

[42] M. R. Khan, G. J. Hayes, J.-H. So, G. Lazzi, and M. D. Dickey, "A frequency shifting liquid metal antenna with pressure responsiveness," *Appl. Phys. Lett.*, vol. 99, 013501, Jul. 2011.

[43] Y. Yang, G. Ruan, C. Xiang, G. Wang, and J. M. Tour, "Flexible three-dimensional nanoporous metal-based energy devices," *J. Am. Chem. Soc.*, vol. 136, pp. 6187-6190, Apr. 2014.

[44] A. C. Arias, S. E. Ready, R. Lujan, W. S. Wong, K. E. Paul, A. Salleo, M. L. Chabinyc, R. Apte, R. A. Street, Y. Wu, P. Liu, and B. Ong, "All jet-printed polymer thin-film transistor active-matrix backplanes," *Appl. Phys. Lett.*, vol. 85, 3304, Aug. 2004.

[45] K. Hong, S. H. Kim, K. H. Lee, and C. D. Frisbie, "Printed, sub-2V ZnO electrolyte gated transistors and inverters on plastic," *Adv. Mater.*, vol. 25, no. 25, pp. 3413-3418, Jul. 2013.

[46] A. Pierre, M. Sadeghi, M. M. Payne, A. Facchetti, J. E. Anthony, and A. C. Arias, "All-printed flexible organic transistors enabled by surface tension-guided blade coating," *Adv. Mater.*, vol. 26, no. 32, pp. 5722-5727, Aug. 2014.

[47] A. d. l. F. Vornbrock, D. Sung, H. Kang, R. Kitsomboonloha, and V. Subramanian, "Fully gravure and ink-jet printed high speed pBTTT organic thin film transistors," *Org. Electron.*, vol. 11, no. 12, pp. 2037-2044, 2037. Dec. 2010.

[48] W. Wu, X. Wen, and Z. L. Wang, "Taxel-addressable matrix of vertical-nanowire piezotronic transistors for active and adaptive tactile imaging," *Science*, vol. 340, no. 6135, pp. 952-957, May 2013.

[49] H.-T. Chen, J. F. O'Hara, A. K. Azad, A. J. Taylor, R. D. Averitt, D. B. Shrekenhamer, and W. J. Padilla, "Experimental demonstration of frequency-agile terahertz metamaterials," *Nature Photon.*, vol. 2, pp. 295-298, Apr. 2008.

[50] H.-T. Chen, W. J. Padilla, J. M. O. Zide, A. C. Gossard, A. J. Taylor, and R. D. Averitt, "Active terahertz metamaterial devices," *Nature*, vol. 444, pp. 597-600, Oct. 2006.

[51] A. Jain, P. Tassin, T. Koschny, and C. M. Soukoulis, "Large quality factor in sheet metamaterials made from dark dielectric meta-atoms," *Phys. Rev. Lett.*, vol. 113, 117403, Mar. 2014.

[52] D. R. Smith, D. C. Vier, T. Koschny, and C. M. Soukoulis, "Electromagnetic parameter retrieval from inhomogeneous metamaterials," *Phys. Rev. E*, vol. 71, 036617, Mar. 2005.

[53] D. Schurig, J. J. Mock, B. J. Justice, S. A. Cummer, J. B. Pendry, A. F. Starr, and D. R. Smith, "Metamaterial electromagnetic cloak at microwave frequencies," *Science*, vol. 314, no. 5801, pp. 977-908, Nov. 2006.

[54] D. Shin, Y. Urzhumov, Y. Jung, G. Kang, S. Baek, M. Choi, H. Park, K. Kim, and D. R. Smith, "Broadband electromagnetic cloaking with smart metamaterials," *Nat. Commun.*, vol. 3, 1213, Nov. 2012.

[55] W. Cai, U. K. Chettiar, A. V. Kildishev, and V. M. Shalaev, "Optical cloaking with metamaterials," *Nature Photon.*, vol. 1, pp. 224-227, Apr. 2007.

[56] J. Hao, J. Wang, X. Liu, W. J. Padilla, L. Zhou, and M. Qiu, "High performance optical absorber based on a plasmonic metamaterial," *Appl. Phys. Lett.*, vol. 96, 251104, Jun. 2010.

[57] N. I. Landy, S. Sajuyigbe, J. J. Mock, D. R. Smith, and W. J. Padilla, "Perfect metamaterial absorber," *Phys. Rev. Lett.*, vol. 100, 207402, May 2008.

[58] J. B. Pendry, D. Schurig, and D. R. Smith, "Controlling electromagnetic fields," *Science*, vol. 312, no. 5781, pp. 1780-1782, Jun. 2006.

[59] I. M. Pryce, Y. A. Kelaita, K. Aydin, and H. A. Atwater, "Compliant metamaterials for resonantly enhanced infrared absorption spectroscopy and refractive index sensing," *Acs Nano*, vol. 5, pp. 8167-8174, Sep. 2011.

[60] X. Zhang and Z. Liu, "Superlenses to overcome the diffraction limit," *Nature Mater.*, vol. 7, pp. 435-441, Jun. 2008.

[61] Q. Zhou, Y. Shi, A. Wang, L. Li, D. Zhao, J. Liu, H. Sun, and C. Zhang, "Ultrafast optical modulation of terahertz metamaterials," *J. Opt.*, vol. 13, no. 12, 125102, Nov. 2011.

[62] R. A. Shelby, D. R. Smith, and S. Schultz, "Experimental verification of a negative index of refraction," *Science*, vol. 292, no. 5514, pp. 77-79, Apr. 2001.

[63] D. R. Smith, W. J. Padilla, D. C. Vier, S. C. Nemat-Nasser, and S. Schultz, "Composite medium with simultaneously negative permeability and permittivity," *Phys. Rev. Lett.*, vol. 84, no. 18, pp. 4184-4187, May 2000.

[64] A. A. Zharov, I. V. Shadrivov, and Y. S. Kivshar, "Nonlinear properties of left-handed metamaterials," *Phys. Rev. Lett.*, vol. 91, no. 3, 037401, Jul. 2003.

[65] N. Katsarakis, T. Koschny, M. Kafesaki, E. N. Economou, and C. M. Soukoulis, "Electric coupling to the magnetic resonance of split ring resonators," *Appl. Phys. Lett.*, vol. 84, no. 15, pp. 2943-2945, Feb. 2004.

[66] K. Aydin and E. Ozbay, "Capacitor-loaded split ring resonators as tunable metamaterial components," *J. Appl. Phys.*, vol. 101, no. 2, 024911, Jan. 2007.

[67] I. Gil, J. Bonache, J. Garcia-Garcia, and F. Martin, "Tunable metamaterial transmission lines based on varactor-loaded split-ring resonators," *IEEE Trans. Microw. Theory Techn.*, vol. 54, no. 6, pp. 2665-2674, Jun. 2006.

[68] D. Wang, L. Ran, H. Chen, M. Mu, J. A. Kong, and B.-I. Wu, "Active left-handed material collaborated with microwave varactors," *Appl. Phys. Lett.*, vol. 91, no. 16, 164101, Oct. 2007.

[69] J. Han, A. Lakhtakia, and C.-W. Qiu, "Terahertz metamaterials with semiconductor split-ring resonators for magnetostatic tunability," *Opt. Express*, vol. 16, no. 19, pp. 14390-14396, Aug. 2008.

[70] G. He, R.-x. Wu, Y. Poo, and P. Chen, "Magnetically tunable double-negative material composed of ferrite-dielectric and metallic mesh," *J. Appl. Phys.*, vol. 107, no. 9, 093522, May 2010.

[71] Y. Poo, R.-x. Wu, G.-h. He, P. Chen, J. Xu, and R.-f. Chen, "Experimental verification of a tunable left-handed material by bias magnetic fields," *Appl. Phys. Lett.*, vol. 96, 161902, Apr. 2010.

[72] R. Pratibha, K. Park, I. I. Smalyukh, and W. Park, "Tunable optical metamaterial based on liquid crystal-gold nanosphere composite," *Opt. Express*, vol. 17, no. 22, pp. 19459-19469, Oct. 2009.

[73] D. H. Werner, D.-H. Kwon, and I.-C. Khoo, "Liquid crystal clad near-infrared metamaterials with tunable negative-zero-positive refractive indices," *Opt. Express*, vol. 15, no. 6, pp. 3342-3347, Mar. 2007.

[74] Q. Zhao, L. Kang, B. Du, B. Li, J. Zhou, H. Tang, X. Liang, and B. Zhang, "Electrically tunable negative permeability metamaterials based on nematic liquid crystals," *Appl. Phys. Lett.*, vol. 90, no. 1, 011112, Jan. 2007.

[75] T. S. Kasirga, Y. N. Ertas, M. Bayindir, "Microfluidics for reconfigurable electromagnetic metamaterials," *Appl. Phys. Lett.*, vol. 95, no. 21, 214102, 2009.

[76] F. Zhang, Q. Zhao, L. Kang, D. P. Gaillot, X. Zhao, J. Zhou, and D. Lippens, "Magnetic control of negative permeability metamaterials based on liquid crystals," *Appl. Phys. Lett.*, vol. 92, no.19, 193104, Nov. 2008.

[77] Y. H. Fu, A. Q. Liu, W. M. Zhu, X. M. Zhang, D. P. Tsai, J. B. Zhang, T. Mei, J. F. Tao, H. C. Guo, X. H. Zhang, J. H. Teng, N. I. Zheludev, G. Q. Lo, and D. L. Kwong, "A micromachined reconfigurable metamaterial via reconfiguration of asymmetric split-ring resonators," *Adv. Funct. Mater.*, vol. 21, no. 18, pp. 3589-3594, Aug. 2011.

[78] M. Lapine, D. Powell, M. Gorkunov, I. Shadrivov, R. Marques, and Y. Kivshar, "Structural tunability in metamaterials," *Appl. Phys. Lett.*, vol. 95, no. 8, 084105, Aug. 2009.

[79] M. Lapine, I. V. Shadrivov, D. A. Powell, and Y. S. Kivshar, "Magnetoelastic metamaterials," *Nature Mater.*, vol. 11, pp. 30-33, Nov. 2012.

[80] W. M. Zhu, A. Q. Liu, X. M. Zhang, D. P. Tsai, T. Bourouina, J. H. Teng, X. H. Zhang, H. C. Guo, H. Tanoto, T. Mei, G. Q. Lo, and D. L. Kwong, "Switchable magnetic metamaterials using micromachining processes," *Adv. Mater.*, vol. 23, no. 15, pp. 1792-1796, Feb. 2011.

[81] D. Bouyge, A. Crunteanu, M. Duran-Sindreu, A. Pothier, P. Blondy, J. Bonache, J. C. Orlianges, and F. Martin, "Reconfigurable split rings based on MEMS switches and their application to tunable filters," *J. Opt.*, vol. 14, no. 11, 114001, Jul. 2012.

[82] H. Tao, A. C. Strikwerda, K. Fan, W. J. Padilla, X. Zhang, and R. D. Averitt, "MEMS based structurally tunable metamaterials at terahertz frequencies," *J. Infrared Millim. Terahertz Waves*, vol. 32, no. 5, pp. 580-595, May 2011.

[83] K. Hong, S. H. Kim, K. H. Lee, and C. D. Frisbie, "Printed, sub-2V ZnO Electrolyte Gated Transistors and Inverters on Plastic," *Adv. Mater.*, vol. 25, no. 25, pp. 3413-3418, Jul. 2013.

[84] J. H. So, J. Thelen, A. Qusba, G. J. Hayes, G. Lazzi, and M. D. Dickey, "Reversibly deformable and mechanically tunable fluidic antennas," *Adv. Funct. Mater.*, vol. 19, no. 22, pp. 3632-3637, Nov. 2009.

[85] W. Z. Wu, X. N. Wen, and Z. L. Wang, "Taxel-addressable matrix of vertical-nanowire piezotronic transistors for active and adaptive tactile imaging," *Science*, vol. 340, no. 6135, pp. 952-957, May 2013.

113

[86] J. Yoon, S. Y. Hong, Y. Lim, S. J. Lee, G. Zi, and J. S. Ha, "Design and fabrication of novel stretchable device arrays on a deformable polymer substrate with embedded liquid-metal interconnections," *Adv. Mater.*, vol. 26, no. 38, pp. 6580-6586, Oct. 2014.

[87] G. J. Hayes, J. H. So, A. Qusba, M. D. Dickey, and G. Lazzi, "Flexible liquid metal alloy (EGaIn) microstrip patch antenna," *IEEE Trans. Antennas Propag.*, vol. 60, no. 5, pp. 2151-2156, May 2012.

[88] M. Kubo, X. F. Li, C. Kim, M. Hashimoto, B. J. Wiley, D. Ham, et al., "Stretchable microfluidic radiofrequency antennas," *Adv. Mater.*, vol. 22, no. 25, pp. 2749-2752, Jul. 2010.

[89] M. Wang, C. Trlica, M. R. Khan, M. D. Dickey, and J. J. Adams, "A reconfigurable liquid metal antenna driven by electrochemically controlled capillarity," *J. Appl. Phys.*, vol. 117, 194901, May 2015.

[90] S. Cheng, A. Rydberg, K. Hjort, and Z. G. Wu, "Liquid metal stretchable unbalanced loop antenna," *Appl. Phys. Lett.*, vol. 94, 144103, Apr. 2009.

[91] M. Jobs, K. Hjort, A. Rydberg, and Z. G. Wu, "A Tunable spherical cap microfluidic electrically small antenna," *Small*, vol. 9, no. 19, pp. 3230-3234, Oct. 2013.

[92] S. M. Yang and J. M. Song, "Guided and leaky modes of circular dielectric waveguide solved with multiple special functions," *IEEE Antennas and propagation Int. Symp.*, Paper 108.6, pp. 125-126, Sep. 2014.

[93] A. Sommerfeld, *Electrodynamics*, translated by Ramberg, E. G., Academic Press, New York, 1952.

[94] S. M. Yang and J. M. Song, "Efficient initial guesses for solving guided and leaky modes in dielectric rod," *Annual Review of Progress in Applied Computational Electromagnetics*, pp. 148-149, Mar. 2015.

[95] Tjalling J. Ypma, "Historical development of the Newton-Raphson method", *SIAM Review*, vol. 37 no. 4, pp. 531551, Feb. 1995.

[96] A. Ishimaru, *Electromagnetic wave propagation, radiation, and scattering,* Prentice Hall, Inc., 1991.

[97] W. C. Chew, *Waves and fields in inhomogeneous media*, IEEE Press, New York, 1995.

[98] P. John, "Metamaterials: Neither solid nor liquid," *Nature Materials*, vol. 10, no. 8, pp. 565-566, Jul. 2011.

[99] S. B. Guenneau, A. Movchan, G. Ptursson, and S. A. Ramakrishna, "Acoustic metamaterials for sound focusing and confinement," *New Journal of Physics*, vol. 9, 399, Nov. 2007.

[100] V. G, Vesekago, "The electrodynamics of substances with simultaneously negative values of ϵ and μ," *Sov. Phys. Usp*, vol. 10, no. 4, pp. 509-514, Jan. 1968.

[101] J. B. Pendry, A. J. Holden, W. J. Strewart, and I. Youngs, "Extremely low frequency plasmons in metallic mesostructures," *Phys. Rev. Lett.*, vol. 76, no. 25, pp. 4773-4776, Jun. 1996.

[102] J. B. Pendry, A. J. Holden, D. R. Robbins, and W. J. Strewart, "Low frequency plasmons in thin-wire structures," *J. Phys. : Condens. Matter,*, vol. 10, no. 22, pp. 4785-4809, Mar. 1998.

[103] J. B. Pendry, A. J. Holden, D. J. Robbins, and W. J. Stewart, "Magnetism from conductors and enhanced nonlinear phenomena," *IEEE Trans. Microw. Theory Techn.*, vol. 47, no. 11, pp. 2075-2084, Nov. 1996.

[104] J. B. Pendry, "Negative refraction makes a perfect lens," *Phys. Rev. Lett.*, vol. 85, no. 18, pp. 3966-3969, Oct. Nov. 2000.

[105] R. A. Shelby, D. R. Smith, S. C. Nemat-Nasser, and S. Schultz, "Microwave transmission through a two-dimensional, isotropic, left-handed metamaterial," *Appl. Phys. Lett.*, vol. 78, no. 4, pp. 489-491, Nov. 2001.

[106] K. Li, S. J. Mclean, R. B. Gregor, C. G. Parazzoli, and M. Tanielian, 2003 "Free-space focused-beam characterization of left-handed materials," *Appl. Phys. Lett.*, vol. 82, no. 15, pp. 2535-2537, Apr. 2003.

[107] D. R. Smith and J. B. Pendry, "Homogenization of metamaterials by field averaging," *J. Opt. Soc. Amer. B, Opt. Phys.*, vol. 23. no. 3, 391-403, Mar. 2006.

[108] V. Shalaev, "Optical negative-index metamaterials," *Nat. Photon.*, vol. 1, pp. 41-48, Jan. 2007.

[109] C. M. Soukoulis, S. Linden, and M. Wegener, "Negative refractive index at optical wavelengths," *Science*, vol. 315, no. 5808, pp. 47-49, Jan. 2007.

[110] G. Dolling, M. Wegener, C. M. Soukoulis, and S. Linden, "Negative-index metamaterial at 780 nm wavelength," *Opt. Lett.*, vol. 32, no. 1, pp. 53-55, Dec. 2007.

[111] P. Liu, S. Yang, A. Jain, Q. Wang, H. Jiang, J. Song, T. Koschny, C. M. Soukoulis, and L. Dong, "Tunable meta-atom using liquid metal embedded in stretchable polymer," *J. Appl. Phys.*, vol. 118, 014504, Jul. 2015.

[112] Peng Liu, Micro-electro-opto-fluidic systems for biomedical drug screening and electromagnetic filtering and cloaking applications, Ph.D. thesis, Iowa State University, Ames, Iowa, 2016.

[113] S. Yang, P. Liu, M. Yang, Q. Wang, J. Song, and L. Dong, "From Flexible Meta-Atom to Metamaterial: A wearable Mircowave Meta-Skin with Tunable Frequency Selective and Cloaking Effects," *Sci. Rep*, vol. 6, 21921, Feb. 2016.

[114] C. Balanis, "Antenna Theory, Analysis, and Design," 3rd ed. New York: Wiley, 2005.